TEL AVIV UNIVERSITY

The Iby and Aladar Fleischman Faculty of Engineering
The Zandman-Slaner School of Graduate Studies
The School of Electrical Engineering

SPATIOTEMPORAL ANALYSIS OF OPTICAL NANOSENSORS BASED ON NEAR-INFRARED FLUORESCENT SINGLE-WALLED CARBON NANOTUBES USING MICROFLUIDICS PLATFORMS

A thesis submitted toward the degree of
Master of Science in Electrical Engineering

By

Edward Sharaga

December 2023

TEL AVIV UNIVERSITY

The Iby and Aladar Fleischman Faculty of Engineering
The Zandman-Slaner School of Graduate Studies
The School of Electrical Engineering

SPATIOTEMPORAL ANALYSIS OF OPTICAL NANOSENSORS BASED ON NEAR-INFRARED FLUORESCENT SINGLE-WALLED CARBON NANOTUBES USING MICROFLUIDICS PLATFORMS

A thesis submitted toward the degree of
Master of Science in Electrical Engineering

By

Edward Sharaga

This research was carried out in The Department of Biomedical Engineering under the supervision of Prof. Gili Bisker

December 2023

Acknowledgments

First and foremost, I would like to express my earnest gratitude to my supervisor, Prof. Gili Bisker, for the patient mentoring, invaluable guidance, advice and support, for teaching me, challenging me, and being a role model for leadership, hard-work, and interpersonal communication.

I would also like to thank Dr. Adi Hendler-Neumark, Dr. Verena Wulf, and Dr. Dotan Kamber for their patience and support, for always offering a helping hand, and for being great partners in this journey. For everyone in the Bisker Lab group, I am truly grateful for being a part of this team.

I would like to thank the Israel Science Foundation and the Ministry of Science, Technology, and Space, Israel, for supporting this project. I would also like to thank the Marian Gertner Institute for Medical Nanosystems at Tel Aviv University.

Lastly, I would like to thank my family for being there with me on this journey.

Abstract

Functionalized Single-walled carbon nanotubes (SWCNTs) can be tailored to recognize specific analytes. Owing to the SWCNTs fluorescence in the near-infrared (NIR) range, which overlaps with the biological transparency spectral window, target interaction with the functionalized SWCNT can result in a modulation of the emitted fluorescence manifested as either an intensity change or a peak emission wavelength shift, rendering SWCNTs optical nanosensors.

This method opens new avenues for synthetic, non-biological antibody analogs that recognize biological macromolecules and can further be used as tracking probes in model organisms such as the widely studied Caenorhabditis elegans (*C. elegans*) nematodes. Animal response to changes in environmental cues is a complex dynamical process that occurs at diverse molecular and cellular levels. It is desirable to have a well-controlled method in order to gain a quantitative understanding of such processes with a high spatial and temporal resolution. Indeed, this is accomplished by utilizing microfluidic devices for confinement, and environmentally controlled interface.

In this research, the SWCNTs serve as fluorescent probes and tracking agents within the *C. elegans* gut, following internalization along with food intake. We employ a microfluidic confinement device to ensure an anesthetics-free feeding environment, allowing spatiotemporal control over the SWCNTs intake imaging. The SWCNTs NIR fluorescence allows us to avoid the autofluorescence background in the visible range emitted by the worm. We demonstrate enhanced spatiotemporal capabilities of the SWCNT sensors when utilized as practical *in vivo* sensing and tracking devices.

Publications

- Edward Sharaga, Adi Hendler-Neumark, Dotan Kamber, and Gili Bisker, ‘‘**Spatiotemporal tracking of near-infrared fluorescent single-walled carbon nanotubes in *C. elegans* nematodes confined in a microfluidics platform**’’, *Advanced Materials Technologies*, 2023.

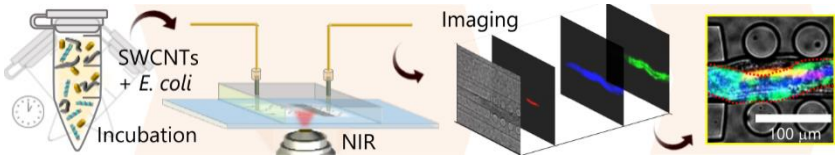

Abstract: Caenorhabditis elegans (*C. elegans*) nematodes are a powerful model organism for diverse biological and biomedical studies, benefiting from their genetic similarities to humans, small size, and transparency. However, live fluorescence imaging of *C. elegans* can be challenging due to the strong autofluorescence in the visible range, which obscures the signal of common fluorescent proteins or dyes. Single-walled carbon nanotubes (SWCNTs) fluoresce in the near-infrared (NIR) range, where there is no autofluorescence background. Herein, we develop a platform for *in vivo* NIR imaging of *C. elegans* gastrointestinal tract using biocompatible SWCNTs functionalized by single-stranded DNA or phospholipid-polyethylene glycol (PEG). The SWCNTs serve as fluorescent tracking probes within the worm gut, following internalization along with food intake. We employ a microfluidic confinement device to ensure an anesthetics-free feeding environment, allowing spatiotemporal control over the SWCNTs intake imaging. Furthermore, we demonstrate improvement in spectral colocalization, real-time detection of intracorporeal SWCNTs dynamics, and digestive trajectory tracking. Owing to the unique optical properties of SWCNTs and the confinement of the worms in the microfluidics system, our proposed platform facilitates advanced *in vivo* imaging of *C. elegans* in both the visible and NIR regions, opening numerous avenues for advancing research of *C. elegans* and other microscopic model organisms

TABLE OF CONTENTS

LIST OF FIGURES

1. Introduction

1.1. *C. elegans* as model organism

A widely used *in vivo* model organism, the nematode Caenorhabditis elegans (*C. elegans*) is a transparent, non-parasitic soil-dwelling roundworm that has become a well-established experimental system used for numerous applications (**Figure 1**).[1] Due to its small size (0.25 – 1 mm), ease of maintenance, culturing in large numbers, rapid life cycle, and genetic tractability, it has been used to study various aspects of human biology, including but not limited to developmental biology, neurobiology, cell biology, aging, and in recent years, transgenerational epigenetics.[2–6]

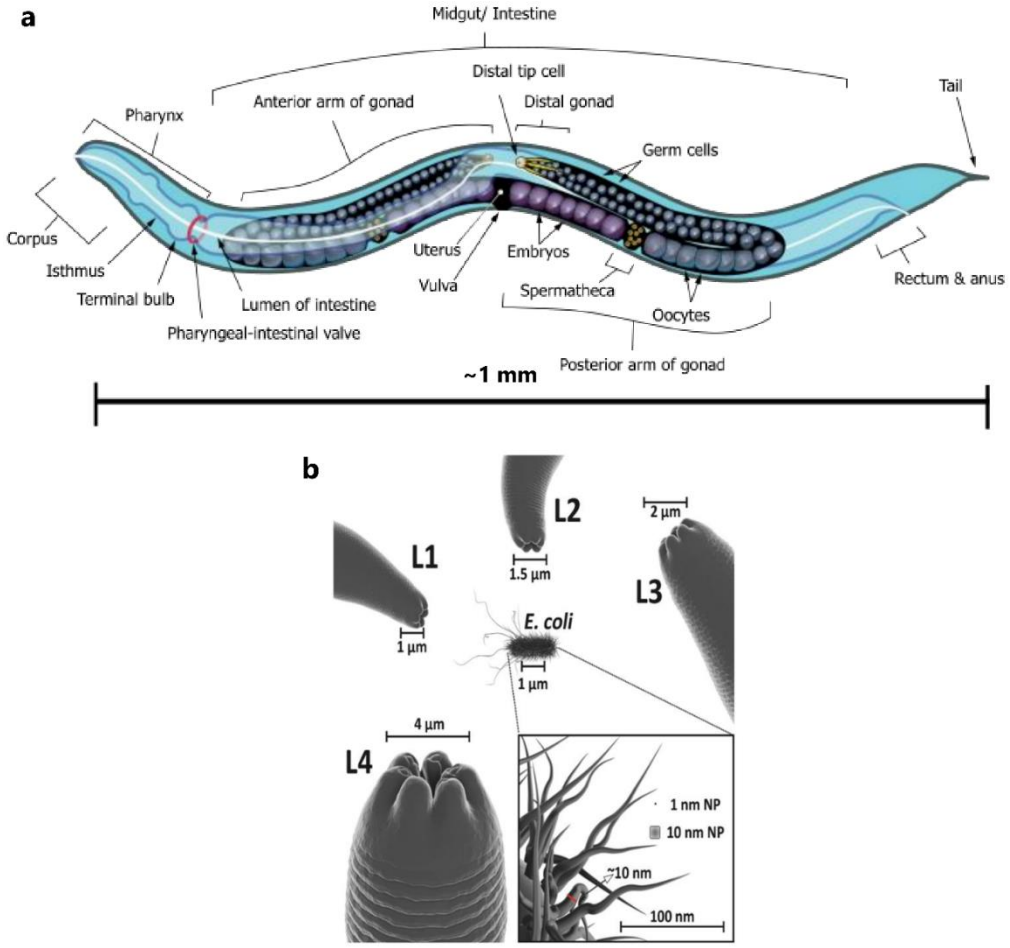

Figure 1. *C. elegans* body structure and scale. a) Reprinted from K. D. Schroeder, CC BY-SA 3.0 https://commons.wikimedia.org/w/index.php?curid=26958836. A lateral side anatomical diagram of an adult-stage *C. elegans* hermaphrodite. b) Reprinted from[7] .3D representation and comparison between the size of *C. elegans* mouth in different larval stages, *E. coli* bacteria, and nanoparticles (NP). L1-L4 indicate the four larvae growth stages from egg, larval 1 stage (L1) through larval 4 stage (L4), and finally, the adult stage.

C. elegans has become a potent experimental system for investigating the *in vivo* molecular and cellular mechanisms underlying human diseases. It has been estimated that roughly 42% of human disease genes have an ortholog in the *C. elegans* genome, including those associated with Alzheimer's disease, juvenile Parkinson's disease, spinal muscular atrophy, hereditary non-polyposis colon cancer, and many other age-related disorders.[8] Using a simple invertebrate like *C. elegans* to model a human disease enables the deconstruction of complex molecular pathways into their individual components, resulting in valuable insights into the pathogenesis of a complex disease phenotype.[9] Notable examples are the discovery of major factors involved in apoptosis, phagocytosis and necrosis,[10–14] the discovery of key genes implicated in cancer,[15,16] the study of genes involved in neurodegenerative disorders,[17,18] and the discovery of genes regulating longevity like insulin/insulin-like growth factor 1 (IGF1) signaling.[19] The *C. elegans* nematode is also becoming a popular platform for a deeper understanding of the underlying mechanism of anti-parasitic agents and various human drugs,[20,21] as well as for the discovery of new bioactive compounds.[22]

Imaging of *C. elegans* internal processes, certain proteins, cellular compartments, or tissues, are normally performed by labeling targets with fluorescent markers. Fluorescent markers are used to indicate defects in function, gene expression, development, or protein interactions *in vivo*.[23,24] For example, the green fluorescent protein (GFP) reporter is commonly used in transgenic *C. elegans* worms,[25,26] and the 40,60-diamidino-2-phenylindole hydrochloride (DAPI) is most commonly used as DNA dye for worm cell compartments visualization,[27] and germ line development.[28]

Furthermore, the autofluorescence of the worm can function as an indicator to determine the health of the organism or its organs, as well as aging and developmental stages.[24,29–33] Strong autofluorescence in *C. elegans* can be detected throughout the visible spectral

range (**Figure 2**) and is caused by a few major sources. For example, in the GFP wavelength (excitation 470-490 nm and emission 500-550 nm), the source is primarily the presence of flavin-containing molecules such as riboflavin and flavin adenine dinucleotide (FAD) in the intracellular lysosome-derived granules, mitochondria or extracellular collagen present in the cuticle, uterus and intestine of the worm,[23,34] whereas in the DAPI wavelength range (excitation 325-375 nm and emission 435-485 nm), the autofluorescence is mainly due to the presence of lipofuscin, a fluorescent pigment that accumulates in aging cells and which is located in the gut granules.[35,36]

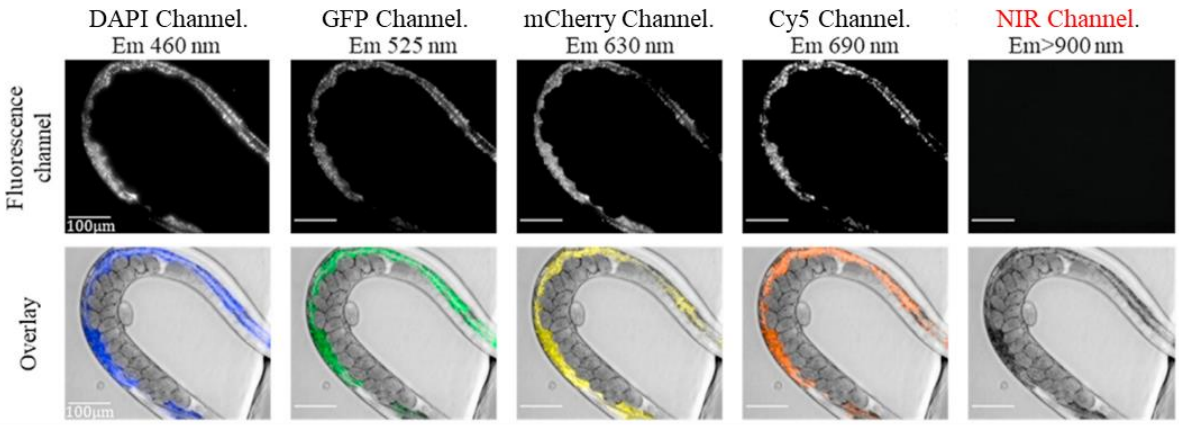

Figure 2. *C. elegans* autofluorescence in the visible and NIR spectral range. Reprinted from[37]. Visible autofluorescence (400–800 nm) of the worms imaged with an EMCCD- camera under LED illumination (4 leftmost columns). The fluorescence channels imaged are named after the common dyes they are applied to, and cover the visible emission wavelength range: DAPI (blue, λ_{ex} = 365 nm; λ_{em} = 435–485 nm), GFP (green, λ_{ex} = 460 nm; λ_{em} = 500–550), mCherry (yellow, λ_{ex} = 525 nm; λ_{em} = 590–670 nm) and Cy5 (orange, λ_{ex} = 635 nm; λ_{em} = 665–715 nm). The right column shows images taken with an InGaAs camera, detecting fluorescence in the NIR spectral region (λ_{em} > 900 nm) under LED illumination with the four wavelengths used for the visible range (λ_{ex} = 365, 460, 525, 635 nm), demonstrating the lack of autofluorescence in the NIR. Top row shows the fluorescence emission images, and bottom row shows their overlay with the brightfield images. Scale bar is 100 µm.

Besides protein labeling, *C. elegans* has gained importance as a model for evaluating particles uptake and feeding behaviors for a wide range of fields such as ecology and evolution,[38,39] aging and metabolism,[40,41] health and disease,[42,43] drug delivery,[44] and nanomaterial toxicity.[7,45–47] Assessing the processes and fate of ingested particles in the worm's intestine is therefore of great interest (**Figure 3**). In nanomaterials research, for

example, the *C. elegans* nematode is utilized to study the uptake, distribution, and toxicity of various nanoparticles, including gold,[48] silver,[49] and carbon nanotubes.[37,50,51]

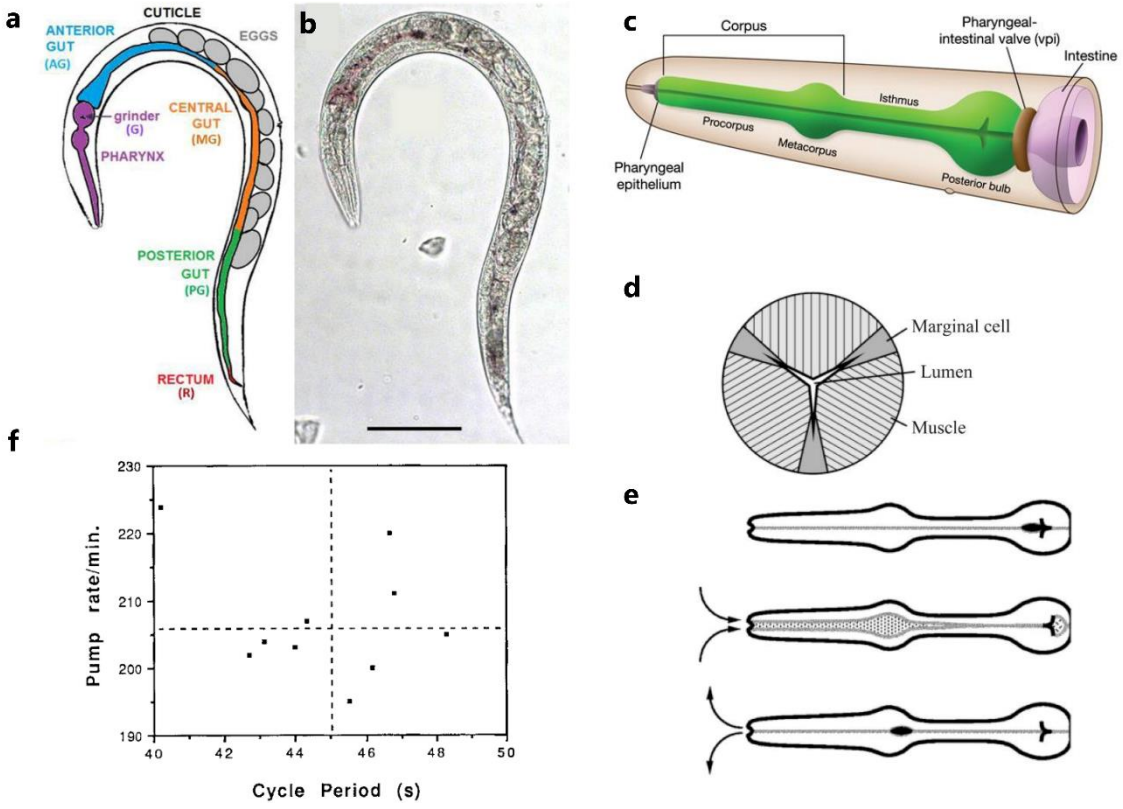

Figure 3. Alimentary mechanism and structure in *C. elegans* nematodes. a) Reprinted from[48] Copyright (2023), with permission from Elsevier. A schematic drawing of the intestinal tract anatomical parts. Segmentation of five parts: pharynx, which contains the grinder; the anterior, mid and posterior parts of the gut, and the rectum. b)[48] Optical microscopy images of 11-nm gold nanoparticles (AuNPs in pink) treated worms. Scale bar is 100 μm. c) Reprinted from[52]. Graphic rendition of the pharynx anatomy. The metacorpus is also called the anterior bulb. The posterior bulb is also called the terminal bulb. At the anterior end, the pharynx is connected to the buccal cavity. At the posterior end, it is connected to the intestine through the pharyngeal-intestinal valve. d) Reproduced with permission from [53]. Simplified schematic of the pharynx cross section. e) Reproduced with permission from[53]. Schematic of pharyngeal food intake by pumping mechanism. A contraction–relaxation cycle involving the corpus, anterior half of the isthmus and terminal bulb. f) Reprinted from[54] according to CC BY 4.0 DEED. *C. elegans* periodic defecation motor. Average defecation periods plotted against average pharyngeal pumping rates (food intake) for 10 worms shows no correlation.

Another common example that uses the feeding mechanism in *C. elegans* models is the study of host-microbiota interactions and bacterial infections related to human pathogens.[55] Typically, these bacteria express a fluorescent protein and are introduced into the worms through food intake. This approach allows for the identification of the defense

response pathway and the interplay between offensive and defensive factors involved.[56–59]. Many research studies have explored intestinal imaging in *C. elegans* by employing conventional visible fluorescent proteins or particles,[60] such as glucose uptake[61] or abnormal pharyngeal structure in response to phm-2 gene mutation.[62] However, the majority of frequently used fluorescent dyes emit fluorescence in the visible wavelength range, which overlaps with the autofluorescence exhibited by the worms so that the fluorescent agents can unambiguously label only proteins or compartments that are spatially separated from the intestines and the uterus of the worm. To address this challenge, a few approaches were introduced, such as administering RNA interference (RNAi) to the worms through feeding and thus reducing the autofluorescence of the intestine, however, it could also cause changes in gene functions.[23,63] Another possible approach to address the fluorescence crosstalk is to separate the spectral bands of the fluorescence proteins emission from the worm's autofluorescence with a triple band filter set, however, it can also block some of the fluorescence emission of the dye.[64] One promising solution for overcoming fluorescence masking involves the use of fluorescent markers with emission spectra that are spectrally distinct from the visible autofluorescence of the worms (**Figure 4**), for example, the near-infrared (NIR) range (700 nm – 2500 nm).[65–68]

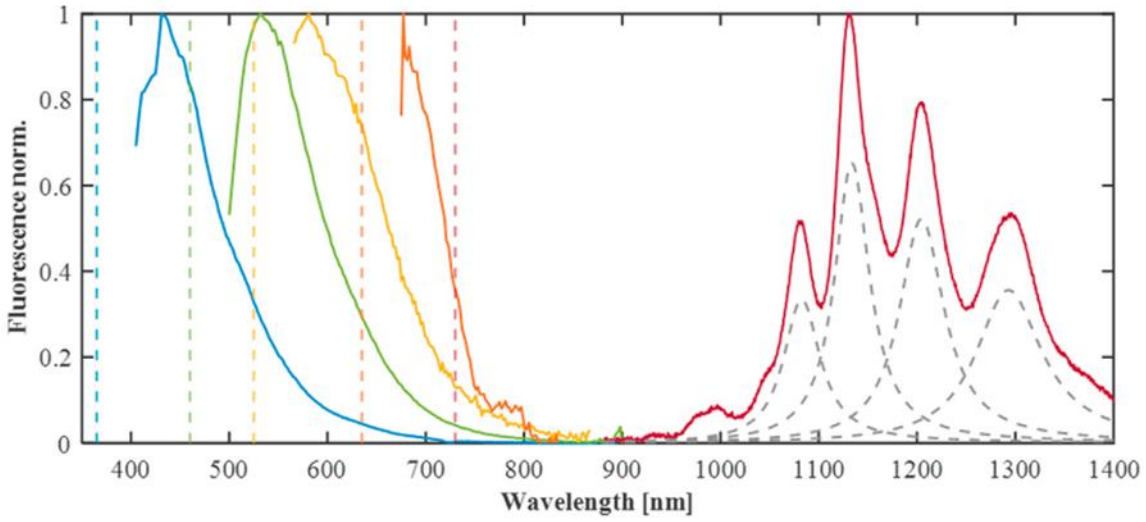

Figure 4. Visible autofluorescence of *C. elegans* and NIR fluorescence of single-walled carbon nanotubes (SWCNTs). Reprinted from[37]. The worms show autofluorescence in the entire visible range up to 900 nm. The SWCNTs fluorescence (solid red curve, >900 nm) inside the worms does not overlap with the *C. elegans* autofluorescence.

1.2. SWCNTs sensors and NIR imaging

NIR imaging techniques, which take advantage of the unique properties of the NIR spectral range, have emerged as a powerful tool for non-invasive *in vivo* imaging.[65,69,70] In particular, single-walled carbon nanotubes (SWCNTs) have been found to exhibit fluorescence in the near-infrared II (NIR-II) region, mainly between 900 and 1400 nm (**Figure 4**).[71] This is due to their unique semiconducting electronic band structure, which allows them to absorb and emit light at specific wavelengths.

SWCNTs may be conceptualized as tubular structures composed of graphene sheets that are cylindrically configured (**Figure 5**a, b, c, and d), exhibiting diameters within the range of 0.7 to 3 nm and lengths spanning from 300 nm to 10 μm. The distinct chiralities of these nanotubes arise from the diverse rolling orientations. Due to the susceptibility of SWCNTs' properties to structural nuances, each specific chirality is associated with discrete attributes, including diameter, as well as distinct physical, chemical, electronic, and optical characteristics.

The angle values can be described using two real space basis vectors of the hexagonal lattice structure of the graphene layer (**Figure 5**a)[72] $\mathbf{a_1}$ and $\mathbf{a_2}$:

$$\mathbf{a_1} = \left(\frac{\sqrt{3}a}{2}, \frac{a}{2}\right) \quad (1)$$

$$\mathbf{a_2} = \left(\frac{\sqrt{3}a}{2}, -\frac{a}{2}\right) \quad (2)$$

Where, $a = |\mathbf{a_1}| = |\mathbf{a_2}| = 2.46$ Å ,is the graphene lattice constant.

The roll-up angle of the SWCNT can be described by a lattice chiral vector that is a linear combination of the two:

$$\mathbf{C}_h = n\mathbf{a_1} + m\mathbf{a_2} \equiv (n, m) \quad (3)$$

Where n and m are the integers defining the chirality of the resulting cylinder. These indices can be used to calculate the diameter D and chiral angle θ of the SWCNT using the following equations:

$$D = \frac{a}{\pi}\sqrt{n^2 + nm + m^2} \quad (4)$$

$$\cos\theta = \frac{2n+m}{2\sqrt{n^2+nm+m^2}} \quad (5)$$

Different chiralities manifest distinctive conductive attributes, encompassing metallic, semimetallic, or semiconducting characteristics. These characteristics are intricately intertwined with the density of electronic states (DOS), as well as the energy bandgap existing between the conduction and valence bands (**Figure 5**e), and can yield a variety of optical transitions.[73] SWCNTs can be functionalized with various chemical groups to tune their resonant fluorescence excitation (E22-transitions) and emission (E11-transitions) wavelengths, and render them more suitable for specific applications as fluorescent probes or sensors given tailored functionalization.[74–78] Moreover, SWCNTs benefit from a relatively large excitation-to-emission wavelength difference (Stokes

shifts), having an excitation wavelength in the visible range and an emission wavelength in the NIR biological transparency window (>900 nm) (**Figure 5**f).[79–86]

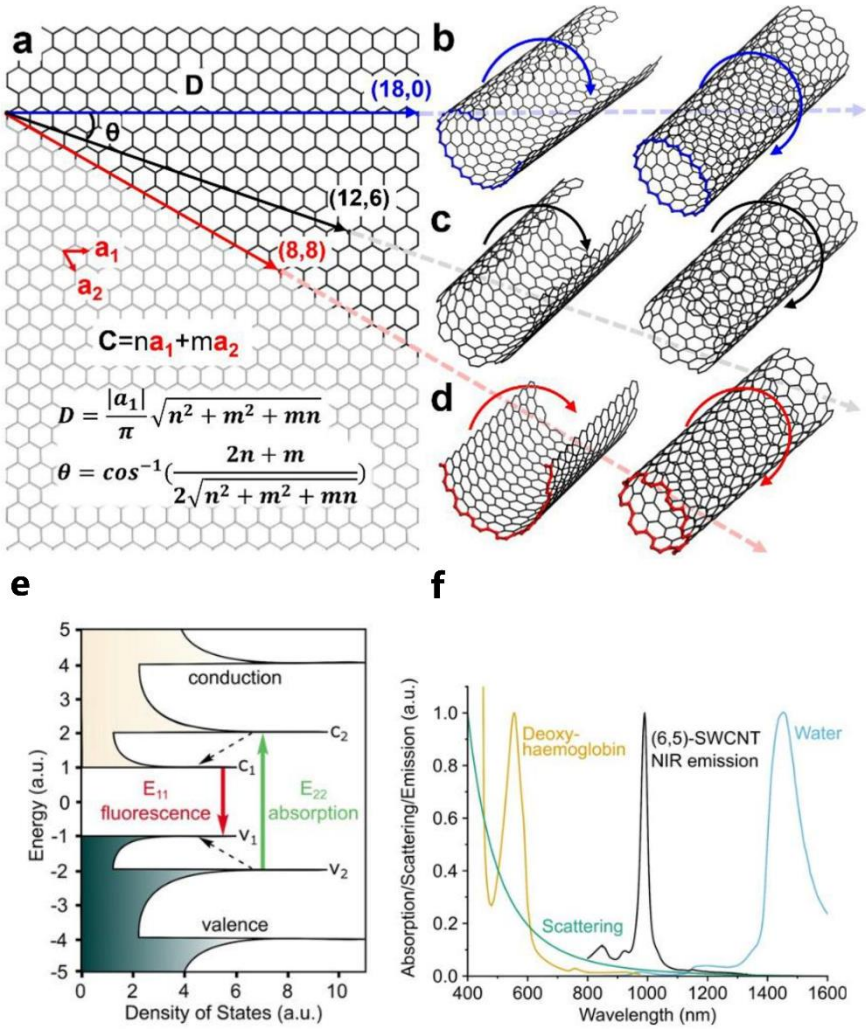

Figure 5. Physical and optical properties of SWCNTs. a) Reprinted with permission from[87] Copyright (2021), American Chemical Society. Chirality of SWCNTs, where $\mathbf{a_1}$ and $\mathbf{a_2}$ are the basis vectors of graphene and **C** is the chiral vector, we can obtain different SWCNTs (b−d) depending on the rolling direction and the length of the vector. The chiral angle $\boldsymbol{\theta}$ and the diameter **D** of the SWCNT as functions of the chiral indexes ($\boldsymbol{n}, \boldsymbol{m}$) are also shown. e) Reprinted from[88]. The density of states (DOS) of SWCNTs. The band gap structure gives rise to fluorescence emission in the near infrared (NIR). f) Reprinted from[88]. Biological transparency window. The E11 transition of SWCNTs overlaps with the tissue transparency window, offering the advantage of reduced light absorption, scattering (*e.g.*, Rayleigh) and background fluorescence. Here, the emission spectrum of SWCNTs of (6,5)- chirality is shown, but the emission wavelengths for other chiralities span the whole NIR range.

Being highly hydrophobic nanostructures, the pristine SWCNTs tend to clump in an aqueous environment. However, their properties can be altered to suit many applications by surface functionalization (**Figure 6**). The choice of functionalization method depends on the desired properties of the SWCNTs and the specific application. For example,

SWCNTs can be suspended in an aqueous solution using noncovalent functionalization by polymers, DNA, RNA, dendrons, proteins, peptides, peptoids, surfactants, or specific recognition elements like antibodies or aptamers.[78,89,98–103,90–97] SWCNTs functionalization can improve the electronic and optical properties of SWCNTs, making them useful in electronics,[104] photonics,[105] energy storage,[106] materials science,[107] and agriculture applications,[108,109] as well as in the biomedical field.[110–117] Several studies demonstrated the feasibility of SWCNTs as fluorescence sensors or markers *in vivo*.[83,84,125–128,85,118–124]

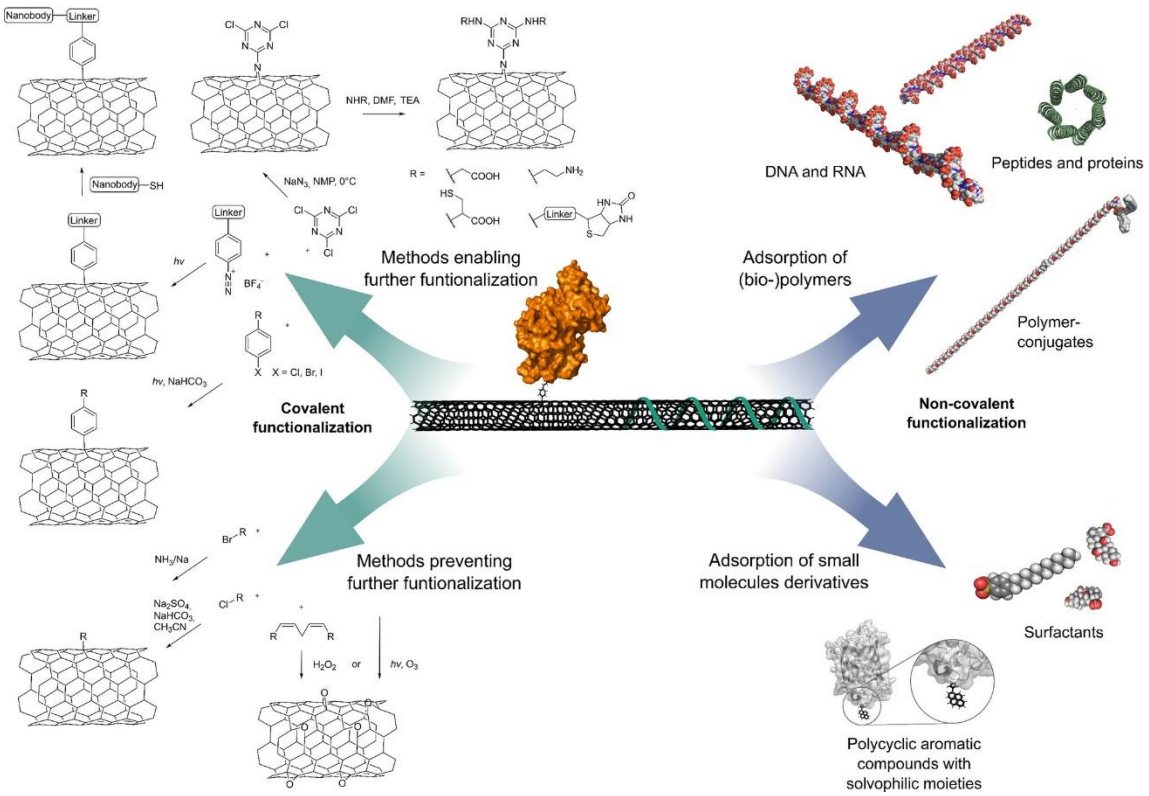

Figure 6. Covalent and non-covalent (bio)functionalization approaches of SWCNTs. Reprinted from[88].

Indeed, imaging *C. elegans* using the fluorescence emission of SWCNTs can be advantageous owing to the spectral distinguishability between the SWCNTs' NIR fluorescence and the autofluorescence of the worm in the visible range, thereby improving

quantitative analysis as well. Hence, the utilization of SWCNTs as fluorescence probes can be extended beyond specific areas or organs. Furthermore, unlike organic fluorescent dyes, SWCNTs do not exhibit photobleaching or blinking, making them ideal for imaging extended dynamic processes.[129–132]

1.3. Microfluidic devices for spatiotemporal control

Long-term *in vivo* imaging of SWCNTs within *C. elegans* requires a well-controlled spatiotemporal environment for restricting the worms in an optically accessible setting and avoiding movement-related artifacts while allowing for continuous feeding and washing procedures. In previous studies, such imaging on free-roaming *C. elegans* worms presented some difficulties due to the hectic locomotion of the worms, and required some means of immobilization or real-time complex imaging setups.[133–135] Worms immobilization techniques, such as introducing anesthetics or using polystyrene nanoparticles on agarose pads,[136,137] were either ill-controlled or contained compounds that were often not compatible with the physiological processes being studied and usually precluded long-term imaging.[138,139]

One popular method for *C. elegans* immobilization is using microfluidic devices, owing to the precision of control, minimal stress to animals, compatibility with imaging settings, high throughput, reusability, and versatility. Numerous microfluidics-based solutions were previously proposed for confining worms in a controlled space, where each platform served different purposes and varied in fabrication complexity and experimental operation.[140,141,150–153,142–149] For example, worms could be immobilized for high-resolution applications, including imaging at subcellular resolution, flow-controlled microfluidic devices could be used for automated sorting of worms with high throughput, and some devices offer the capability of longitudinal imaging of individuals for studying

development, aging and stress response. Moreover, experiments such as electrotaxis,[154] pharyngeal activity,[155] mechanical stimuli,[156] and acoustic manipulation became available on-chip (**Figure 7**).[157]

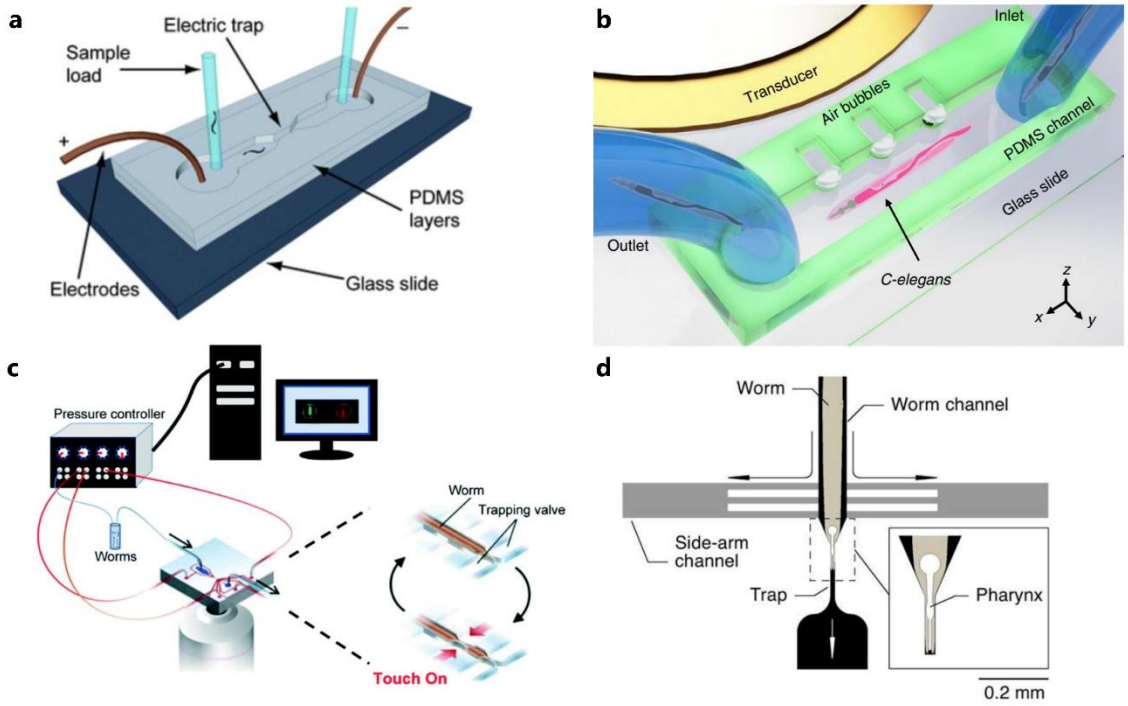

Figure 7. Microfluidic devices designed for specific research applications on *C. elegans* nematods. a) Used with permission of Royal Society of Chemistry**,** from[154] , Copyright (2012) permission conveyed through Copyright Clearance Center, Inc. Microfluidic devices for worm electrotactic sorting. Single electric trap device. b) Reprinted from[157]. Design and operation of the acousto-fluidic rotational manipulation (ARM) device. The acoustic waves actuate air microbubbles trapped within sidewall microcavities. *C. elegans* is trapped by multiple oscillating microbubbles. c) Reproduced from[156] with permission from the Royal Society of Chemistry. A microfluidic platform designed to deliver a mechanical stimulus and allow imaging of calcium responses in *C. elegans* mechanoreceptor neurons. d) Used with permission of Royal Society of Chemistry**,** from[155] Copyright (2012) permission conveyed through Copyright Clearance Center, Inc. Design of the microfluidic device for recording electropharyngeograms (EPGs). Top view of a single recording module.

In one well-exploited example, the "Worm Spa" microfluidic device, was used in several applications such as surveillance of *C. elegans* response to environmental cues, serotonin promotion of feeding dynamics, and longitudinal imaging.[158–161]

Despite the significant potential of using NIR imaging with functionalized SWCNTs in *C. elegans* confined within a microfluidic device, thorough investigations of such a platform that can utilize long-term NIR imaging for *in vivo* applications are lacking. For

example, the suggested platform would enable deeper insights into the worm's digestive tract physiology and could have significant implications for understanding gastrointestinal disorders and drug development.

1.4. Research goal

In this work,[162] we aim to develop and implement a platform for *in vivo* imaging of SWCNTs as NIR fluorescent probes within the model organism *C. elegans* nematodes. Our approach leverages a microfluidic device tailor-made to provide optimal spatial and temporal control, thereby facilitating whole organism imaging. We plan to use the nutritional source for *C. elegans* worms, namely, the *E. coli* bacteria, as a conduit to introduce SWCNTs into the worms through the food intake process. During the imaging, we aim to showcase multi-spectral fluorescence imaging and colocalization, highlighting spectral distinction between the worm's intrinsic autofluorescence in the visible wavelengths range the SWCNTs probes NIR fluorescence. We intend to examine different types of functionalized SWCNTs, such as single-stranded DNA (ssDNA) and PEGylated phospholipids, both of which will be introduced to the *C. elegans* as ingestible NIR fluorescent probes. Finally, we set up to compare different feeding profiles, with an end goal of establishing the functionalized SWCNTs potential as NIR fluorescent real-time tracking agents inside the digestive tract of *C. elegans.* Our work seeks not only to advance *in vivo* imaging techniques in the near-infrared but also to broaden the potential applications of SWCNTs in biological research.

2. Methods and experimental setup

2.1. SWCNTs functionalization

For DNA functionalization, 1 mg of SWCNTs (HiPCO, NanoIntegris) was suspended with 2 mg single-stranded $(GT)_{15}$ DNA oligonucleotides (Integrated DNA Technologies) in 0.1 M NaCl via bath sonication (Elma P-30H, 80 Hz for 10 min), followed by two cycles of direct tip sonication (QSonica Q125, 3 mm tip, 4 W) for 20 min in an ice bath. Aggregates and impurities were then separated from the individually suspended SWCNTs by centrifuging the sample twice for 90 min at 16100 rcf. After each centrifugation step, 80% of the supernatant was collected, and the pellet was discarded.

For Phospholipid PEG functionalization, SWCNTs were first suspended with sodium cholate (SC, Sigma Aldrich), which was later removed by dialysis in the presence of phospholipid-poly(ethylene-glycol)(1,2-dipalmitoyl-sn-glycero-3-phosphoethanolamine-PEG (5 kDa), Avanti Polar Lipids) using methods similar to those previously published.[137] In brief, SWCNTs (HiPCO, NanoIntegris) were first suspended with 2 % wt SC via bath sonication (80 Hz for 10 min), followed by two cycles of direct tip sonication (6 mm tip, 12 W) for 30 min in an ice bath. To remove SWCNT aggregates and impurities, the suspension was ultracentrifuged (OPTIMA XPN-80, Beckman-Coulter, 41,300 rpm for 4 h, 4°C), the top 80% of the supernatant was collected, and the pellet was discarded. Subsequently, a surfactant exchange was performed. To this means, a mixture of SC-SWCNTs (40 mg L^{-1}) and 2 mg mL^{-1} DPPE-PEG (5 kDa) was dialyzed against water using a dialysis membrane (Spectra-Por Float-A-Lyzer G2, Spectrum labs, MWCO: 0.5-1 kDa, 5mL). Dialysis was performed for 7 days with multiple water exchanges to remove SC and allow the adsorption of the DPPE-PEG onto the SWCNTs.

2.2. SWCNTs Characterization

Successful suspensions were validated by recording their ultraviolet-visible-near-infrared (UV–Vis–NIR) absorption spectra, using a UV–Vis–NIR spectrophotometer (Shimadzu UV- 3600 PLUS), in a 1 cm path length quartz cuvette (Starna cells Inc.) where sharp distinguishable peaks indicated a successful suspension (**Figure 8**). The concentrations of $(GT)_{15}$-SWCNT and DPPE-PEG-SWCNTs were determined spectroscopically and using the Beer-Lambert law:

$$A = \varepsilon \cdot c \cdot l \tag{6}$$

Where, A is the light absorbance, ε is the extinction coefficient or the molar absorptivity of the sample ($\varepsilon_{632\,nm} = 0.036$ L mg^{-1} cm^{-1}), l is the light path length ($l = 1$ cm) and c is the sample concentration. A redshift relative to the initial SC-SWCNT suspension of the DPPE-PEG-SWCNTs was also observed (**Figure 8**b), indicating the surfactant exchange.[163]

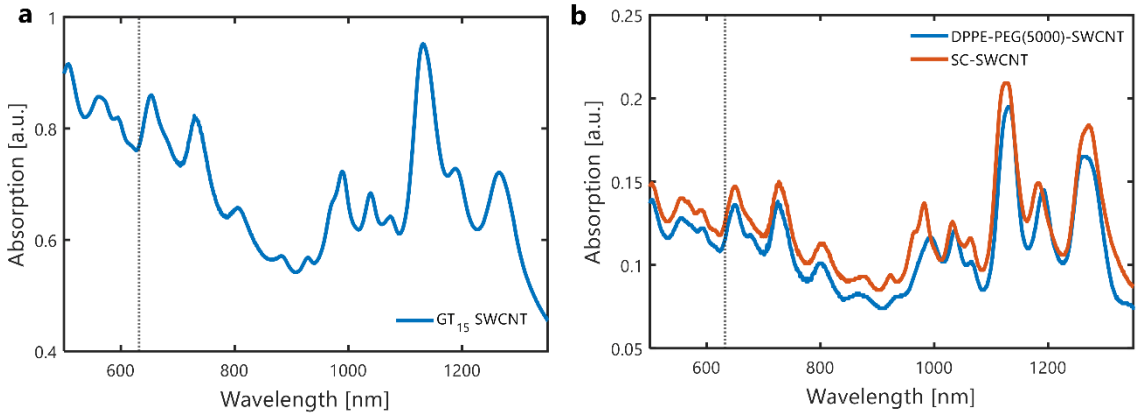

Figure 8. Absorption spectrum of SWCNTs. a) Characteristic absorption spectrum of GT_{15}-SWCNTs. b) Characteristic absorption spectrum of Sodium Cholate SWCNTS (SC-SWCNTs) (red line) and DPPE-PEG(5000)-SWCNTs (blue line). The DPPE-PEG(5000)-SWCNTs are red-shifted compared to the SC-

SWCNTs. The dashed line marks the 632 nm wavelength, where the concentration of particles is calculated from the Beer-Lambert law using the extinction coefficient and the absorption value at this wavelength.

For SWCNTs fluorescence characterization, the excitation-emission map was recorded, (**Figure 9**a and **Figure 9**b). Samples of suspended $(GT)_{15}$-SWCNT and DPPE-PEG-SWCNTs were diluted to 0.5 mg L^{-1} in NaCl 0.1M and were added to the wells of a 96-well plate. The samples were illuminated with a supercontinuum white-light laser (NKT-photonics, Super-K Extreme) coupled to a tunable bandwidth filter (NKT- photonics, Varia, $\Delta\lambda = 20\ nm$) scanned between 500 nm to 840 nm with an excitation time of 2 s per wavelength, a 1 nm wavelength step size, and 20 mW (at 730 nm) intensity. Emission spectra (**Figure 9**c and **Figure 9**d) were recorded on an inverted fluorescence microscope (Olympus IX73) coupled to a spectrograph and a liquid-nitrogen cooled InGaAs detector (HRS-300SS, and PyLoN-IR 1024-1.7, Princeton Instruments, Teledyne Technologies) or adapted from the excitation-emission map.

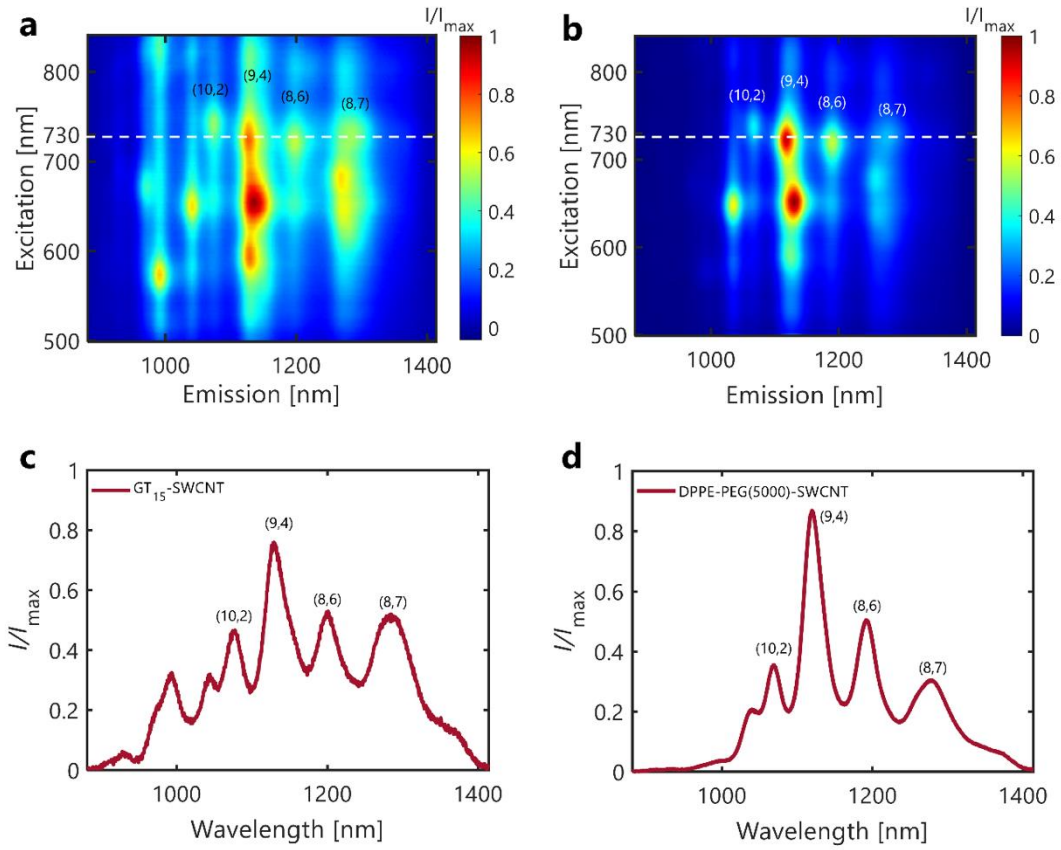

Figure 9. SWCNTs fluorescence measurements. (a-b) Excitation-emission map normalized to the maximum emission intensity, with the predominant chiralities at the excitation wavelength of 730 nm (white dashed line) of a) GT_{15}-SWCNTs and b) DPPE-PEG(5000)-SWCNTs. (c-d) Fluorescence intensity spectrum for an excitation wavelength of 730 nm with the predominant chiralities, adapted from the excitation-emission map, of c) GT_{15}-SWCNTs and d) DPPE-PEG(5000)-SWCNTs.

2.3. *C. elegans* growth and maintenance

The N2 Bristol strain Caenorhabditis Elegans (*C. elegans*) was used as a wild-type animal model in this study (kindly received from Prof. Limor Broday, Tel-Aviv University, Israel). The worms were grown and maintained on standard nematode growth medium (NGM) plates seeded with Escherichia coli (*E. Coli*) strain OP50 as a food source at 22 ± 1 °C. For maintaining the stock culture, the worms were transferred to fresh NGM plates every 5-7 days, similarly as described in previous works.[164,165]

Age-synchronized worms were obtained using the alkaline hypochlorite method (**Figure 10**).[51,166] In brief, cultured worms were collected from 2-3 NGM plates by repeating twice a wash-and-collect cycle followed by the addition of diluted bleach (1%), thus, terminating adult worms and leaving behind a population of eggs, which were then

transferred to fresh NGM plates for hatching and culturing period of 72-96 hours at 22 ± 1 °C, resulting in synchronized adult hermaphrodites.

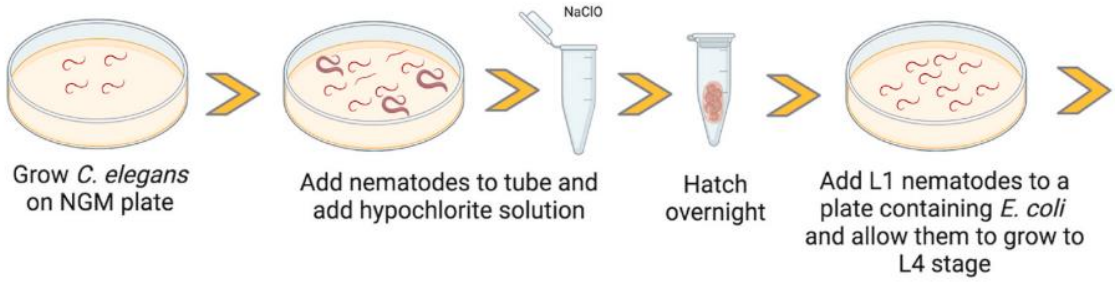

Figure 10. Diagram of synchronization process for *C. elegans* of all stages of life. Reprinted from[22] according to CC BY 4.0 DEED. Worms are grown on petri dishes containing nematode growth media (NGM). These nematodes are then collected and mixed with a hypochlorite solution to lyse the nematode bodies and release the eggs inside the adult nematodes. These eggs hatch in about 8 h and are arrested in the L1 stage until exposed to *E. coli* OP50 (their food source), which allows for experiments to be conducted with nematodes of the same stage of life. These L1 nematodes grow later to L4 and adults.

2.4. Microfluidic device fabrication and assembly

Microfluidic devices (MFD) for longitudinal studies of *C. elegans* worms were fabricated based on a slightly modified design of the 'WormSpa' MFD developed by Kopito and Levine.[159,167] Standard soft-lithography techniques[168] were used to create a master mold for the polydimethylsiloxane (PDMS; Sylgard 184, Dow Corning Corp) structures consisting of 9 individual microfluidic cells, each containing 32 channels (**Figure 11**a and **Figure 11**b). Fabricated at the Tel Aviv University Center for Nanoscience and Nanotechnology facilities, a 4″ silicon wafer was spin-coated with SU-8 photoresist to obtain a uniform height of ~50 µm. This layer was exposed to UV light through a patterned 5" photomask to achieve the microfluidic cell-specific design features. This layer was then etched and cleaned to remove the unexposed SU-8 photoresist. [169] The Silicon master mold was adhered to a 120 mm × 20 mm borosilicate culture plate (SCHOTT) to be used for PDMS casting.

The SU-8 master mold was then used to fabricate the PDMS microfluidic devices. The PDMS was mixed at a ratio of 10:1 (base to curing agent), degassed in a vacuum chamber

for 4 hours to remove bubbles, and slowly poured onto the master to a height of ~7 mm. The PDMS layer was cured at 70 °C for 2 h and peeled off from the SU-8 mold after cooling. Individual cells were cut out and fluid interconnecting holes were punched in manually with a 1.2 mm rapid core microfluidic punch (PT-T983-12, Darwin microfluidics). The PDMS cells were cleaned with tape and irreversibly bonded to a 24 mm × 50 mm #1.0 microscope cover glass (BN1052431STC, Bar-Naor Ltd.) via low-pressure oxygen plasma treatment at 100 W and 0.5 mBar for 60 s (Atto, Diener electronic) (**Figure 11**c).

The fluid interconnectivity (**Figure 11**d) to the devices was accomplished by assembly of a 90° stainless steel 18-gauge PDMS coupler (PN-BEN-18G, Darwin microfluidics) that was inserted into the fluid interconnect holes, and each was connected to a 1.02 × 1.78 mm tubing (SA-AAD04127, Tygon ND 100-80, Darwin microfluidics). Lastly, the inlet and outlet ports of the tubing were connected to an 18-gauge Blunt-end Luer Lock Syringe Needle (AE-18G, Darwin microfluidics).

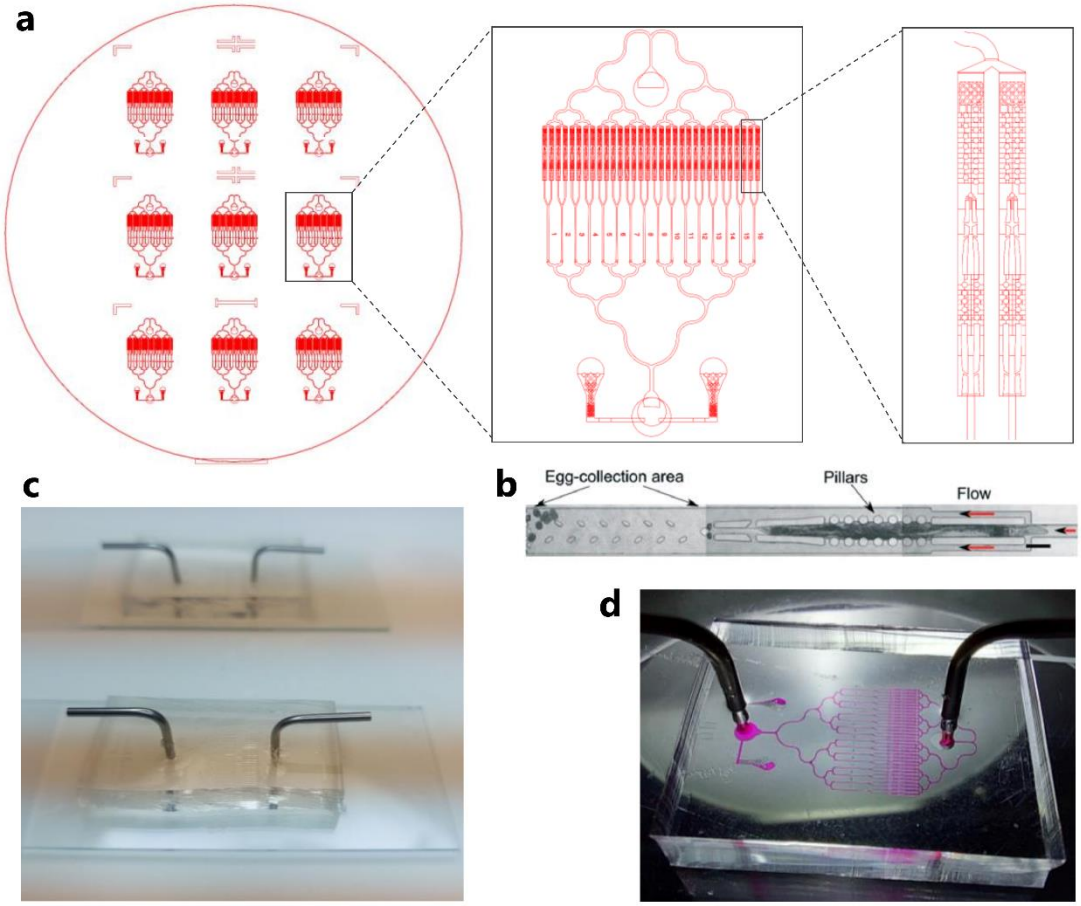

Figure 11. 'Worm Spa' microfluidic device fabrication and assembly. a) Master wafer mold design consisting 9 fluidic cells (left), zoom on fluidic cell design consisting 32 worms confinement channels (middle), zoom on confinment channel design (right). b)[158] Worms confinment channel structure. c) Assembly of PDMS microfluidics on glass covers. d) Demonstration of PDMS microfluidic device functionality.

2.5. Microfluidic device treatment and handling

Prior to loading the microfluidic device with worms, it was surface treated and primed.[170] A freshly assembled MFD was connected to a syringe pump system (NE-4000X, New-Era syringe pump systems Inc.). Then, a solution of 5% w/w Pluronic F-127 (Sigma) in ddH_2O was injected into the MFD at 250 µL min^{-1} for 20 minutes and allowed to be adsorbed onto the PDMS surfaces of the micro-chamber. The MFD was then washed with ddH_2O at 500-700 µL min^{-1} for few minutes. The MFD was primed with M9 buffer (3 g KH_2PO_4, 6 g Na_2HPO_4, 5 g NaCl, 1 ml 1 M $MgSO_4$, ddH_2O to 1 liter, sterilize by autoclaving) at 500 µL min^{-1} for 10 minutes. Using the syringe pump, the M9 buffer was

aspirated and emptied from the micro-chamber and inlet tube, freeing the path for worms loading fluid.

Each Microfluidic device was re-used 1-2 times. A bleach solution (3-5%) was injected into the MFD after completing the experiment, using the same setup as aforementioned, the bleach was infused in both directions of the MFD (inlet and outlet) for 5 minutes respectively at a flow rate of 500 μL min^{-1}. A thorough wash with ddH_2O was then applied, again, in both directions for 5 minutes each at the same flow rate.

2.6. Feeding experimental setup

Feedthrough experiments were performed such that the pre-loaded MFD was scrutinized under the imaging microscope while feeding and incubating the worms with the functionalized SWCNTs occurred in real-time (**Figure 12**). A culture of *E. coli* OP50 grown in LB media was mixed with SWCNTs at a 1:1 ratio. A syringe pump system (New-Era) infused the mixture into the microfluidic device with a flow rate of 250 μL min^{-1} for 60 seconds, followed by a constant flow of 5 μL min^{-1} all throughout the feeding and incubation time. In order to remove eggs from the vicinity of the worms into the egg-collection area, a 15 second pulse of 250 μL min^{-1} was initiated every 30 minutes. Once the SWCNTs were identified within the worm's digestive tract, a wash medium consisting of only M9 buffer was dispensed into the MFD with a flow rate of 400 μL min^{-1} for 2 minutes to wash away any undesired SWCNTs that were outside the worm, followed by a constant flow of 20 μL min^{-1} throughout the imaging sequence.

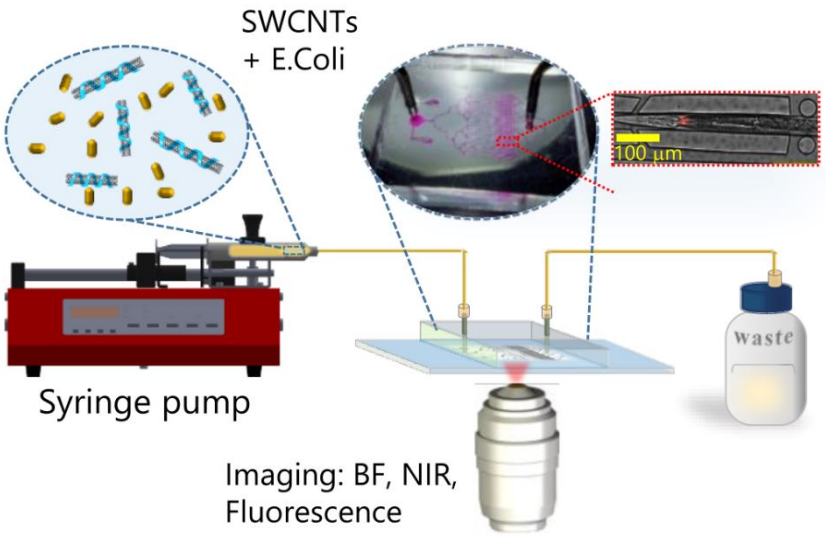

Figure 12. Feedthrough experimental setup.

Another type of experimental setup used in this work utilizes worms that were already incubated with SWCNTs prior to their imaging sequence. Adult hermaphrodite worms (~10-20 subjects) were handpicked from a synchronized culture NGM plate (**Figure 13**) and placed inside a 200 µL loading medium consisting of a 50% *E. coli* and 50% 1mg L^{-1} SWCNT suspension (either $(GT)_{15}$-SWCNT or DPPE-PEG-SWCNT). The loading medium with the worms was then placed in a shaker for incubation between 2-4 hours at 25 °C, resulting in pre-incubated worms ready to be loaded into the microfluidic chamber (**Figure 14**).

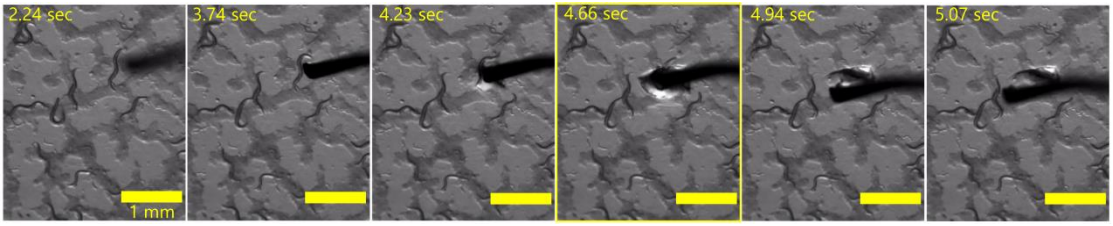

Figure 13. Single *C. elegans* worm handpicking. Image contoured in yellow demostrates instance of the worm collection from the NGM plate with the platinum wire handpicking tool tip. Scale bars are 1 mm.

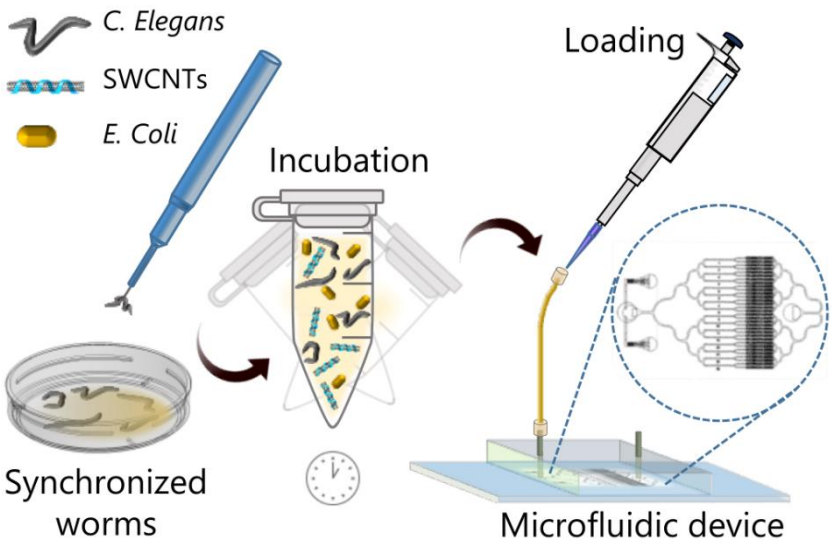

Figure 14. Pre-incubation experimental process.

2.7. Worms loading and mounting

For free-roaming worms fluorescence imaging, worms were mounted on a 3% agarose gel pad on a glass slide, covered with an 18 mm × 18 mm #1.0 microscope cover glass (Marienfeld), and sealed with wax. As for the binocular imaging, worms were used in their original culture NGM plate.

For loading the worms into the microfluidic device, the 200μL of incubated worms in the loading medium were dispensed into the microfluidic device inlet tube with a pipette. The inlet tube was then reconnected to the pump system, and M9 buffer was infused into the microfluidic device at a rate of 450 μL min^{-1} and was supervised through the binocular microscope camera. On the occasion that worms were entangled or clustered, a few iterations of withdrawal and infusion were performed until satisfactory loading was achieved (**Figure 15**). The microfluidic device with the loaded worms was transferred to the fluorescence microscope setup for live imaging.

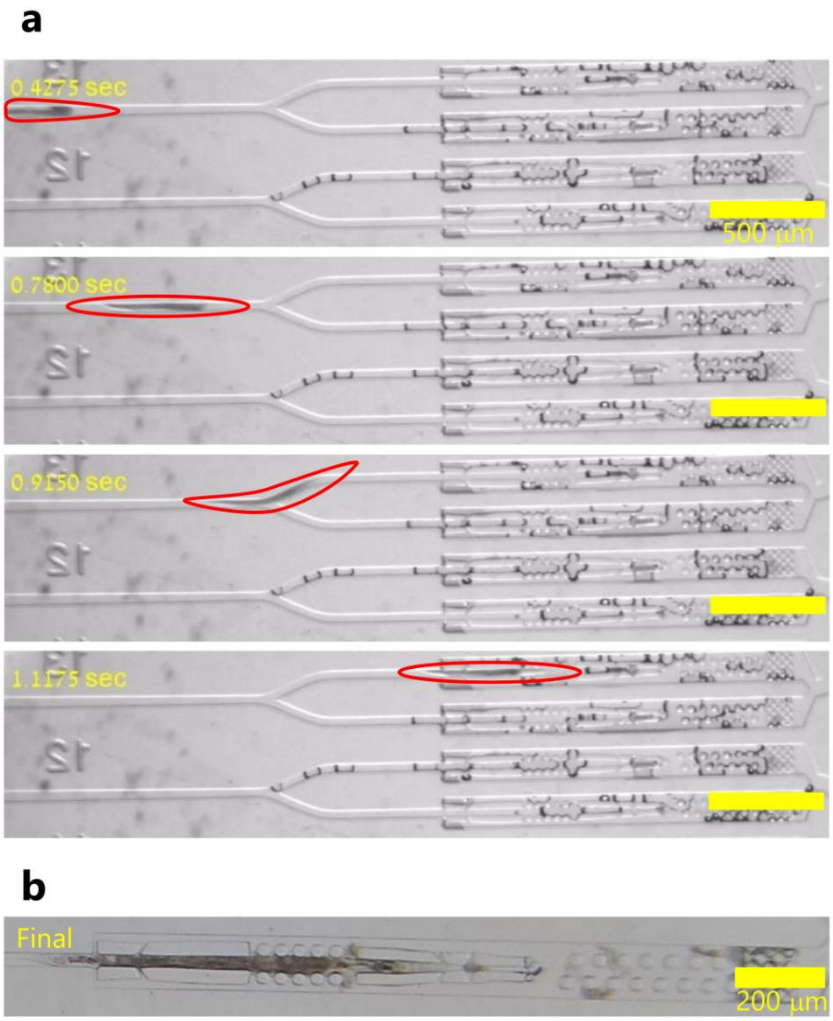

Figure 15. Worms loading. a) A single adult *C. elegans* worm being loaded into a microfluidic channel (marked with a red circle), scale bars are 500 µm. b) A single adult worm loaded and confined in a microfluidic channel. Scale bar is 200 µm.

2.8. Imaging

The Microfluidic device handling and worms loading procedure was aided by a Binocular reverse microscope (Nikon SMZ800N, Objective Nikon plan 1x WD78) with a digital CMOS camera (PL-D752, Pixelink) and Pixelink CAPTURE software.

For the real-time fluorescence imaging (**Figure 16**), images were taken via an inverted fluorescence microscope (Olympus IX83) using five different objectives: UPLFLN4X/0.13, UPLFLN10X/0.3, LUCPLFLN20X/0.45, LUCPLFLN60X/0.7 and UPLFLN100X/1.3. Visible autofluorescence was excited with a LED illumination system

(CoolLED, pE4000), choosing 2 different channels covering the visible excitation wavelengths range for DAPI and GFP (365 nm and 460 nm, respectively). Autofluorescence was imaged using two different filter cubes, covering the visible wavelength range of DAPI (Chroma, 49000), and GFP (Chroma, 49002). Fluorescence in the visible wavelength range was detected with an EMCCD camera (Andor, iXon Ultra 888). The SWCNT- fluorescence was excited by a 730 nm CW laser (MDL-MD-730-1.5 W, Changchun New Industries) with a neutral density filter (ND02B, 63% transmission, Thorlabs) and an excitation power that was measured at the sample plane as 540, 570, 570, 570, 465 mW for the 4×, 10×, 20×, 60×, and 100× objectives, respectively. The laser excitation light was directed to the sample with a dichroic mirror (T900LPXXRXT, Chroma), and the NIR emission of the SWCNTs was detected after an additional 900 nm long-pass emission filter (Chroma, ET900lp) with an InGaAs-camera (Raptor, Ninox 640 VIS-NIR). Videos were taken at frame rates ranging from 2 frames per second down to 0.1 frames per second, depending on the experiment. Exposure times and gains varied between the different wavelengths and objectives used in each experiment for the best SNR and image quality.

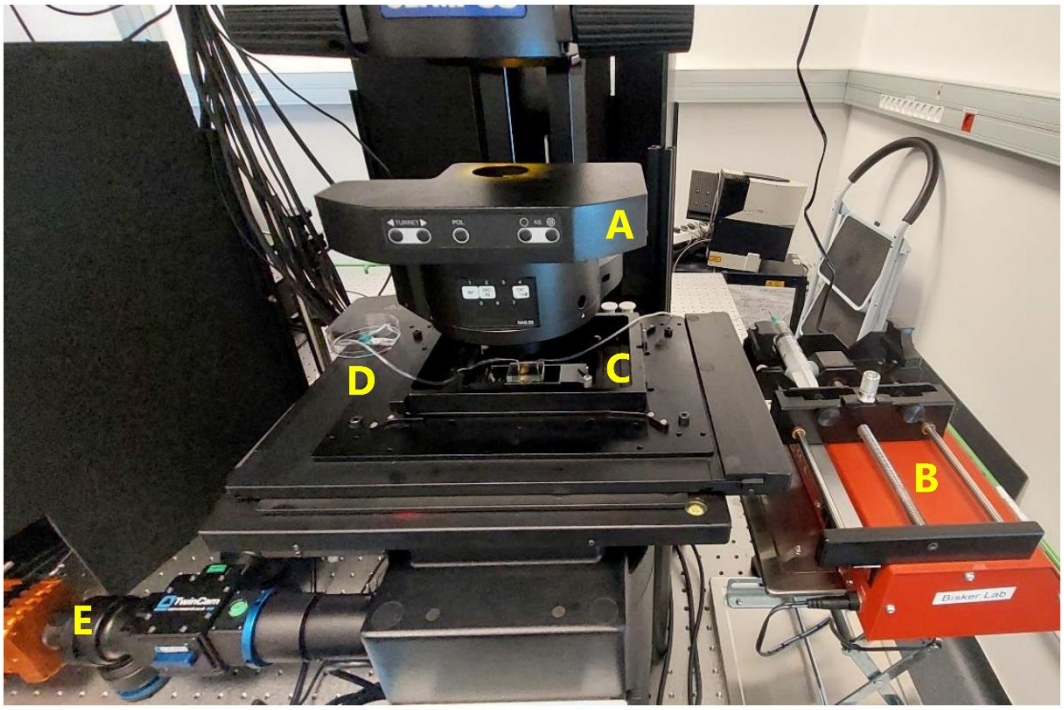

Figure 16. Worms imaging system Setup. Olympus IX83 fluorescence imaging microscope (A), Syringe pump system (B), Microfluidics device (C), Waste container (D), InGaAs-camera (E).

All images were processed by Fiji (ImageJ), and MATLAB (R2021b). In general, NIR images were subtracted by a background out-of-focus image, or de-speckled and adjusted for contrast and brightness, where DAPI, GFP, and BF images were slightly adjusted for brightness and contrast. The overlay of the images from the EMCCD and InGaAs cameras was done by adjusting the pixel sizes and the orientation, where overlay parameters of the two images were determined via maximization of the 2D autocorrelation of an identical mark frame taken with both cameras. The images were then cropped to the desired size, and the scale was calculated accordingly. SWCNTs tracking in the worms was performed by Fiji-TrackMate utility using the differences between Gaussian (DoG) and threshold methods.

3. Results and discussion

3.1. Platform for imaging internalized SWCNTs in *C. elegans*

In order to image SWCNTs internalized by *C. elegans* nematodes, we first established the microfluidics platform and optimized the working conditions. For our study, we chose two different functionalization classes for the SWCNTs to be used as model NIR fluorescent probes, namely, a single-stranded DNA functionalized SWCNT, specifically $(GT)_{15}$-SWCNTs, owing to the ease of sample preparation,[124,171] and phospholipid-PEG functionalized SWCNTs, namely dipalmitoyl-phosphatidylethanolamine (DPPE)-PEG (5 kDa)-SWCNTs, owing to their higher brightness (**Figure 17**), and the PEG corona which suppresses nonspecific binding.[172–174]

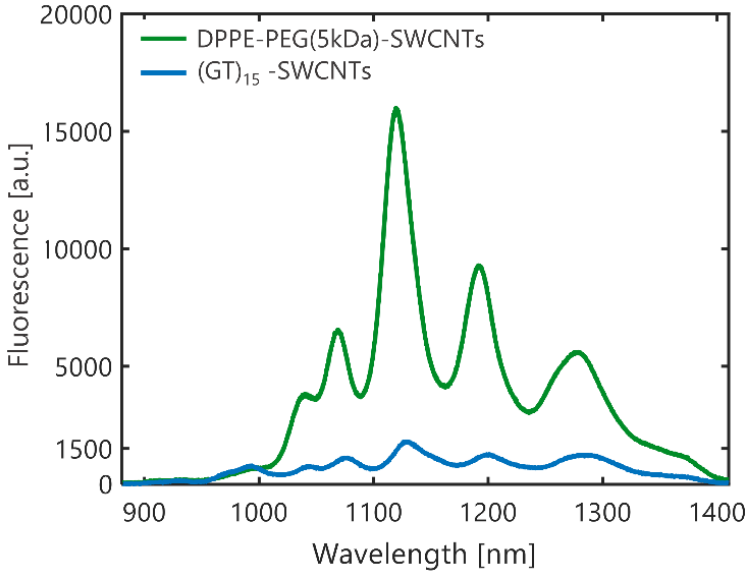

Figure 17. Sensors fluorescence intensity spectrum comparison. DPPE-PEG-SWCNTs and $(GT)_{15}$-SWCNTs fluorescence emission for the same concentration of 0.5 mg L^{-1} at an excitation wavelength of 730 nm.

Both the DNA and PEGylated-lipid SWCNTs functionalizations had previously shown no adverse impact on the viability, well-being, and compatibility with *C. elegans*,[37] cells [175,176] and mice,[177,178] rendering them compelling imaging and sensing agents within *C. elegans*.

The working concentrations of the chosen SWCNTs had to be considered carefully, as low concentrations might result in weak signals below the detection limit of the imaging system, whereas high concentrations could give rise to substantial background fluorescence from SWCNT binding to the surface of the worms or to the microfluidic device and might affect the biocompatibility. Based on previous research,[37,179] the concentration for both types of functionalized SWCNTs was chosen to be 0.5 mg L^{-1}, for optimal signal-to-noise ratio in the NIR images and confirmed biocompatibility. For SWCNT fluorescence excitation, we used a 730 nm CW laser source, which resonates with the absorption of the predominant (10,2), (9,4), (8,6), and (8,7) chiralities (**Figure 9**), all of which emit in the NIR-II, specifically, at 1070 nm, 1120 nm, 1192 nm, and 1278 nm, respectively. Since the *C. elegans* worms are known to be photosensitive,[180,181] we had to evaluate the trade-off between obtaining high-quality data with sufficient excitation power for the SWCNT, and ensuring the safety and well-being of the *C. elegans* worms. To ensure a wide experimental framework consisting of two different types of functionalized SWCNTs with different excitation-emission responses and colloidal manifestation, multiple optical setups, and short and long imaging durations, we optimized our system to an excitation intensity of 570 mW (~10 W mm^{-2}) at the sample plane. The worm's safety was ensured first by using a NIR-I excitation wavelength (730 nm), which overlaps with the biological transparency window, so only a small amount of the energy is absorbed by the biological sample to generate heat or free radicals. Furthermore, we applied short exposure pulses (150-200 msec) with a duty cycle of ~30% on-to-off time, a convection cooling mechanism provided by the microfluidic device, and real-time behavior monitoring.

The SWCNTs were internalized by the worms via food-intake. The *C. elegans* worms ingest food through their mouth into their Pharynx by a peristaltic-like pumping action of

the surrounding liquid containing *E. coli* bacteria,[53] where it passes through the Corpus to the terminal bulb. At the worm's terminal bulb, the grinder physically breaks the food, and it passes through the pharyngeal-intestinal valve into the lumen of the anterior intestines (**Figure 18**). For internalization, the *C. elegans* worms can be pre-incubated with the functionalized SWCNTs in a feeding medium consisting of M9 buffer and *E. coli* bacteria, prior to live imaging.

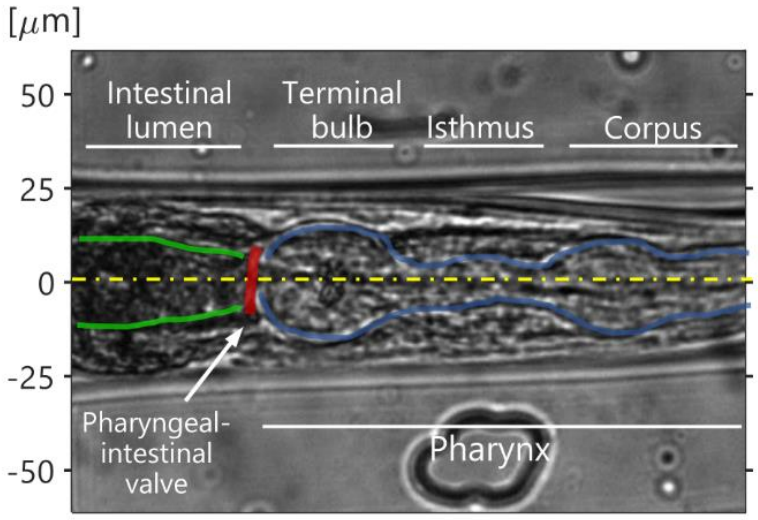

Figure 18. Longitudinal cross-section brightfield image of a confined *C. elegans* worm showing the main anterior features: Pharynx (blue), Pharyngeal-intestinal valve (red), and anterior intestinal lumen (green). Width dimensions are explicitly shown on the vertical axis around the longitudinal mid-axis (yellow dashed line set as zero). Vertical and horizontal scaling is 1:1.

Inspired by the original design of the 'Worm Spa' microfluidics, and to enable worms confinement, we fabricated a modified version of the microfluidic device suitable for our purposes, and subsequently refined the process of worms loading. The Polydimethylsiloxane (PDMS) microfluidic devices were casted from a prefabricated silicon wafer master mold and adhered to a microscope cover glass via a plasma process, thus providing an imaging accessible area of approximately 2.5 mm × 10 mm, covering 32 worm-confining channels, each of which was 50 ± 10 μm in width and height (**Figure 11**). To prevent clogging of worms in the fluidic channels during the loading process, we loaded no more than 20 adult hermaphrodite *C. elegans* worms in one experimental

sequence that were individually handpicked from a pre-synchronized N2-Bristol strain colony and maintained in a loading medium. The worms were then loaded into the microfluidic device inlet and pushed into the confinement channels using a syringe pump system infusing M9 buffer. The loading and infusion protocols were optimized to prevent leaks and blockages, and to smoothly guide individual worms into one of the 32 confinement channels. When the optimal positioning of the worms within the central part of the confinement channel was achieved (**Figure 15**) the worms were ready for imaging. Given the controlled spatiotemporal microfluidics environment we established, in addition to pre-incubation of the worms with SWCNTs for internalization, our platform can also enable real-time feeding during the live imaging, while the worms are confined within the channels.

For fluorescence microscopy, we used a wide range of optical objectives for imaging ranging from 4× up to 100×, to cover as many imaging length scales and configurations as possible. Lower magnifications, such as the 4× and 10×, were normally used to scan the areas of interest and identify candidate worms, whereas the higher magnifications served to focus on the optical plane of interest and subsequently image the internal organs with the internalized NIR fluorescent SWCNTs. For the *C. elegans* autofluorescence imaging, we chose to demonstrate two commonly used excitation wavelengths, corresponding to the green fluorescent protein (GFP) channel, excited at 480 nm, and 4',6-diamidino-2-phenylindole (DAPI) channel, excited at 365 nm, having emission central wavelengths of 530 nm and 430 nm, respectively. The autofluorescence in the visible range was excited using an LED illumination system, and its emission was imaged with an EMCCD camera mounted on an inverted fluorescence microscope. We used a separate InGaAs camera mounted on the same microscope for the NIR fluorescence imaging, where the two images were later overlaid.

Lastly, we optimized the live imaging frame rates and exposure times for optimal signal-to-noise ratio (SNR) in each experimental imaging configuration. Frame rates varied in the range between 2 frames per second for high temporal resolution imaging, and a frame every 10 seconds for stress-free long time-lapse imaging.

3.2. Internalized SWCNTs detection and colocalization

We set to establish a reliable system for detecting, visualizing, and monitoring the SWCNT particles that were internalized by the worms. It was particularly crucial to devise a technique for differentiating intra-corporeal NIR fluorescent SWCNTs from those that were outside the worms. Such a platform enables further exploration of the different optical and spatiotemporal aspects of SWCNT internalization in *C. elegans* worms.

The *C. elegans* is a typical roundworm whose digestive tract is a simple tube with an asymmetrical 'twist' in the intestine between anterior and posterior segments (**Figure 1a**).[182] In many cases, such as in our work, the main region of interest and scrutiny is the anterior part of the intestinal lumen, since it is the most dynamic section and holds most of the feeding mechanism. Within the anterior segment of the worm, where the pharynx, pharyngeal-intestinal valve and a portion of the intestinal lumen are located, the intestine tube is mainly situated along its central longitudinal axis (**Figure 18**). Therefore, we expected to find, in a captured image of the longitudinal center cross-section, fluorescent SWCNTs that are exclusively located inside the worm's body. Any other NIR fluorescent signals, as we realized, were barely discernible. Hence, we assumed them to be out of the focal plane as external entities.

The proposed technique is straightforward. Initially, we opted for a conspicuous and easily identifiable morphological feature of the worm, such as the terminal bulb grinder. This component is situated symmetrically in the center of the pharynx's longitudinal axis,

thereby enabling qualitative *z*-positioning, which brings the focal plane approximately to the central longitudinal axis. Based on this, we can deduce that the radial edges of the worm lie within a range of approximately ± 40 μm, considering that an average adult hermaphrodite measures up to 80 μm in diameter at its broadest point,[183] and the worm is confined in a squared microfluidic channel of 50 ± 10 μm (**Figure 18**).

For the next step, we set this central axis plane as $z = 0$ and took a stack of 11 images at different *z* positions of the worm, ranging from $+50$ μm to -50 μm relative to the $z = 0$ plane in 10 μm intervals, as illustrated for 20× magnification with $(GT)_{15}$-SWCNTs (**Figure 19** and **Figure 20**a).

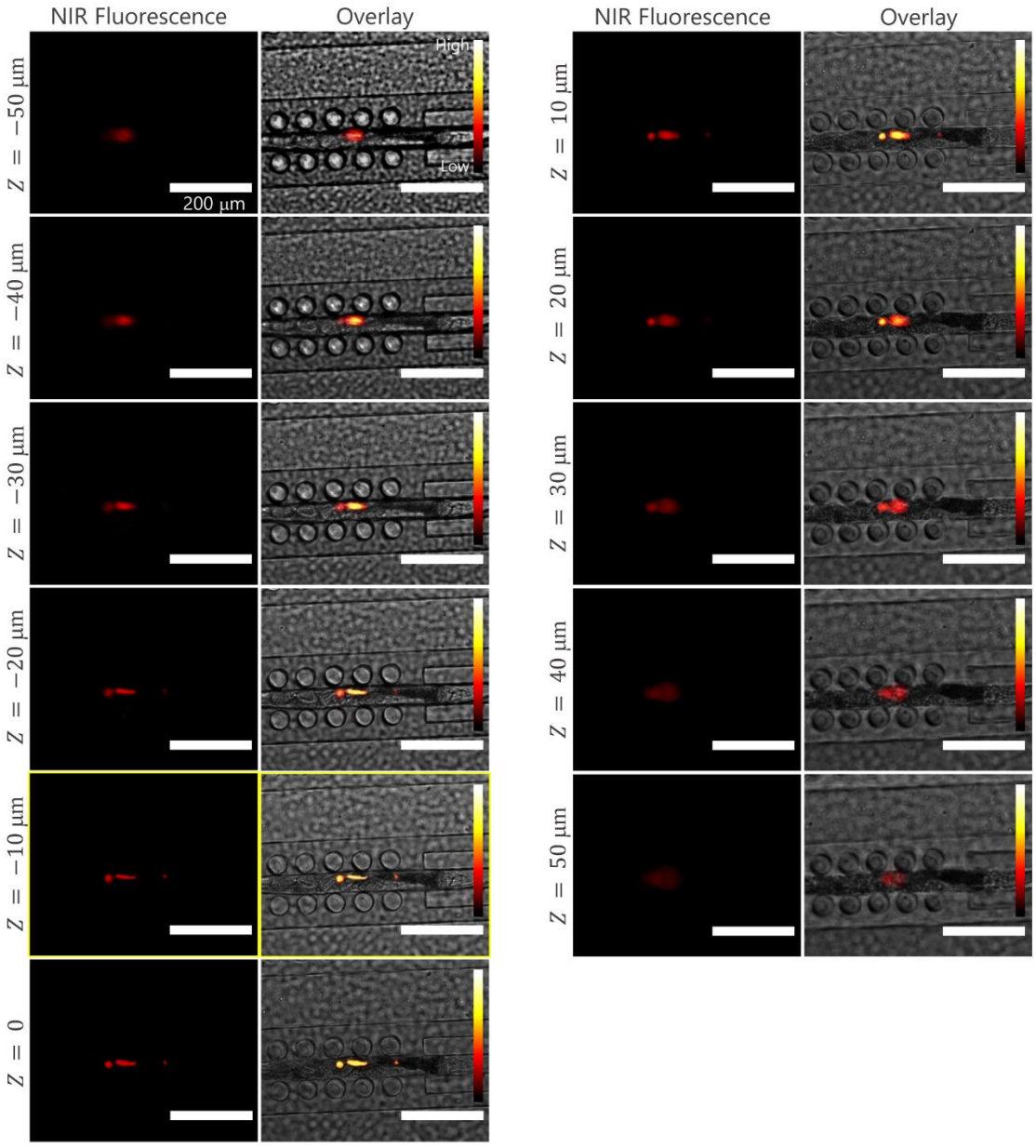

Figure 19. Z-stack imaging. 20× objective, 11 ***z***-planes, **10** µm apart, NIR fluorescence images (left columns), and brightfield and NIR fluorescence overlay images (right columns), framed in yellow, is the plane in focus. Scale bars are 200 µm. The colorbars represent the NIR fluorescence intensity from low (dark red) to high (bright yellow).

Subsequently, we identified a region of interest (ROI) showing SWCNTs fluorescence in the NIR channel, and evaluated the intensity of a vertical line that intersected the fluorescent region (**Figure 20**b) for every *z*-position image (**Figure 20**c). Then, for each slice, we established and assessed the full width at half-maximum (FWHM) of the primary intensity profile, which served as a marker for determining the *z*-position of the

fluorescence image that was 'in-focus'. Choosing the minimum FWHM value from the entire stack of images (**Figure 20**c and **Figure 20**d), we obtained the optimal image, which in this case was at $z = -10$ μm plane. A similar approach was repeated for a different imaging setting with the 60× objective, and the optimal image was found to be at the $z = -20$ μm plane (**Figure 20**e). Considering that we qualitatively set our $z = 0$ plane based on visual assessment of the terminal bulb grinder, which essentially may yield a certain spatial tolerance, we could still ascertain the presence of the SWCNTs inside the body of the worm based on this technique even with a ± 20 μm offset.

To further reinforce the level of confidence in detecting SWCNTs within the worm, a complementary measurement was conducted, based on the assumption that internalized SWCNTs have similar spatial dynamics as the worm, whereas the position of the extra-corporeal SWCNTs is independent with respect to the worm motion. A worm with candidate SWCNTs was temporally imaged for approximately two minutes, and the position of the labeled particles was tracked relative to a fixed point in the microfluidic space and to the worm's terminal bulb grinder (**Figure 20**f and **Figure 20**g). As expected, it can be clearly seen that the internalized SWCNT candidates, marked in blue, have an almost identical motion as the worm's grinder, marked in red, and is entirely independent with respect to the green mark, which labels external SWCNTs that appear static. Slight differences can be observed between the internal SWCNTs and the grinder due to the worm's body contractions, elongations, and bends. Using these two complementary methods, we could relatively easily detect and colocalize the SWCNTs' NIR fluorescence within the worm's digestive tract.

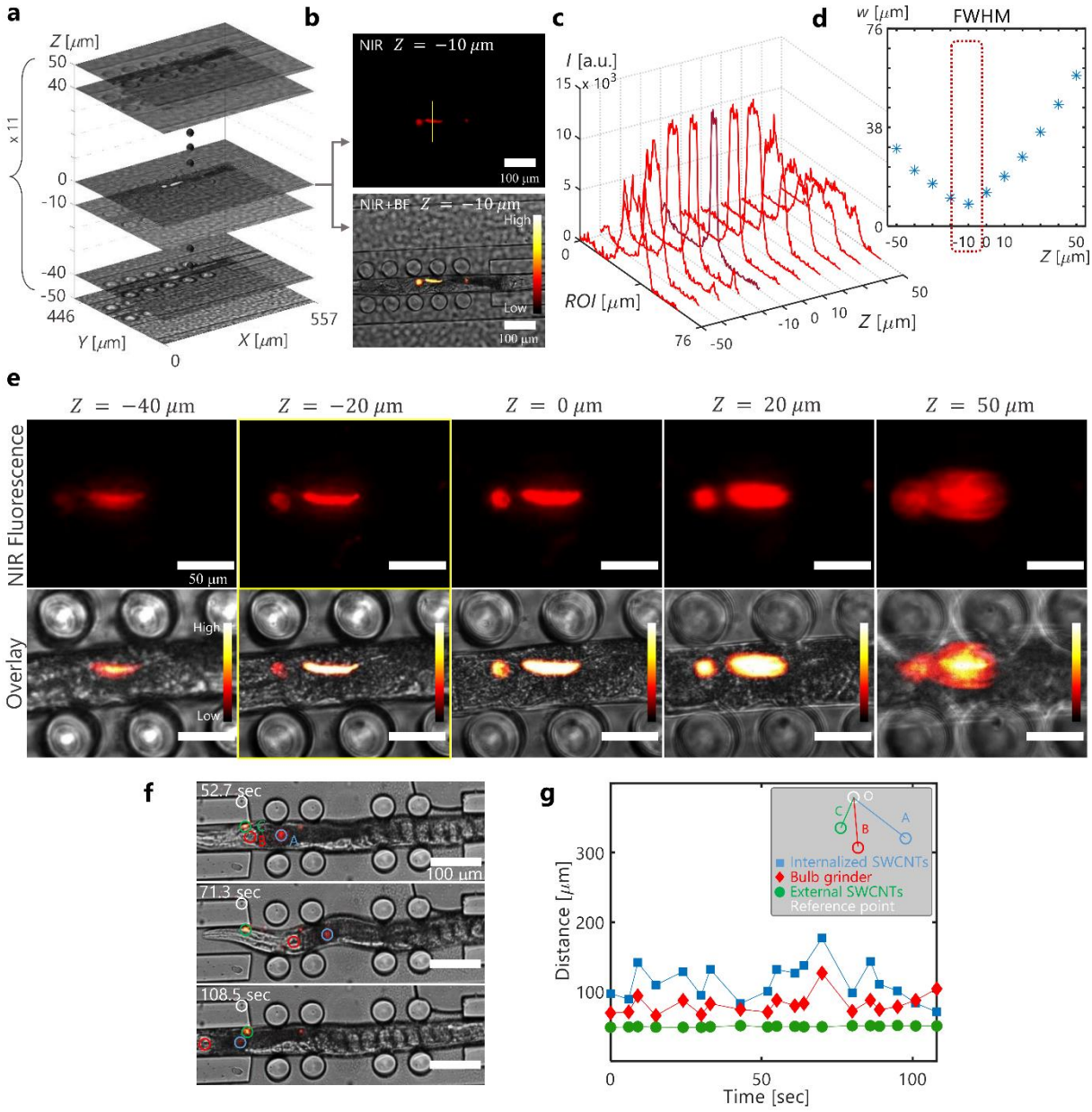

Figure 20. Validation of SWCNTs internalization. a) $\boldsymbol{Z}$-stack images of a *C. elegans* worm with $(GT)_{15}$-SWCNTs taken with 20× objective, 10 μm apart, 11 slices in 3D view, where $\boldsymbol{z = 0}$ marks the middle longitudinal $\boldsymbol{z}$-slice of the images stack. b) NIR (top) and overlay (bottom) images at $\boldsymbol{z = -10}$ μm from the z-stack. A vertical line (yellow) indicates a ROI along which the intensity is analyzed across the different $\boldsymbol{z}$-slices in the fluorescence channel. The scale bar is 100 μm. The colorbar represents the NIR fluorescence intensity from low (dark red) to high (bright yellow). c) Fluorescence intensity for all the $\boldsymbol{z}$-slices along the selected ROI, where $\boldsymbol{z = -10}$ μm (dark red) intensity profile has the minimal FWHM. d) FWHM of the intensity profiles for every $\boldsymbol{z}$-slice, highlighting the minimal value at $\boldsymbol{z = -10}$ μm. e) $\boldsymbol{Z}$-stack images of a *C. elegans* worm with $(GT)_{15}$-SWCNTs taken with 60× objective, 20 μm apart, NIR fluorescence images (top row) and brightfield-NIR overlay images (bottom row). The $\boldsymbol{z = -20}$ μm slice (yellow frame) is the slice in focus. The colorbars represent the NIR fluorescence intensity from low (dark red) to high (bright yellow), scale bar is 50 μm. f) Snapshots of a single worm confined within a microfluidic channel, tracking NIR fluorescent cues: suspected internalized $(GT)_{15}$-SWCNTs (blue, A), terminal bulb grinder (red, B), suspected external $(GT)_{15}$-SWCNTs (green, C) and a reference static point (white). The scale bar is 100 μm. g) Distance of the NIR fluorescent cues from the reference point as a function of time, showing a clear movement of the internalized SWCNTs and worm's grinder, whereas the extracorporeal SWCNTs remain static.

3.3. *In vivo* SWCNTS imaging

Having established a method for detecting and confirming SWCNTs internalized within *C. elegans*, we proceeded to optimize the optical imaging configuration. We examined typical images of the internalized SWCNTs captured at various magnifications and compared the performance of the two different SWCNTs functionalization, namely $(GT)_{15}$-SWCNTs (**Figure 21**a) and DPPE-PEG-SWCNTs (**Figure 21**b).

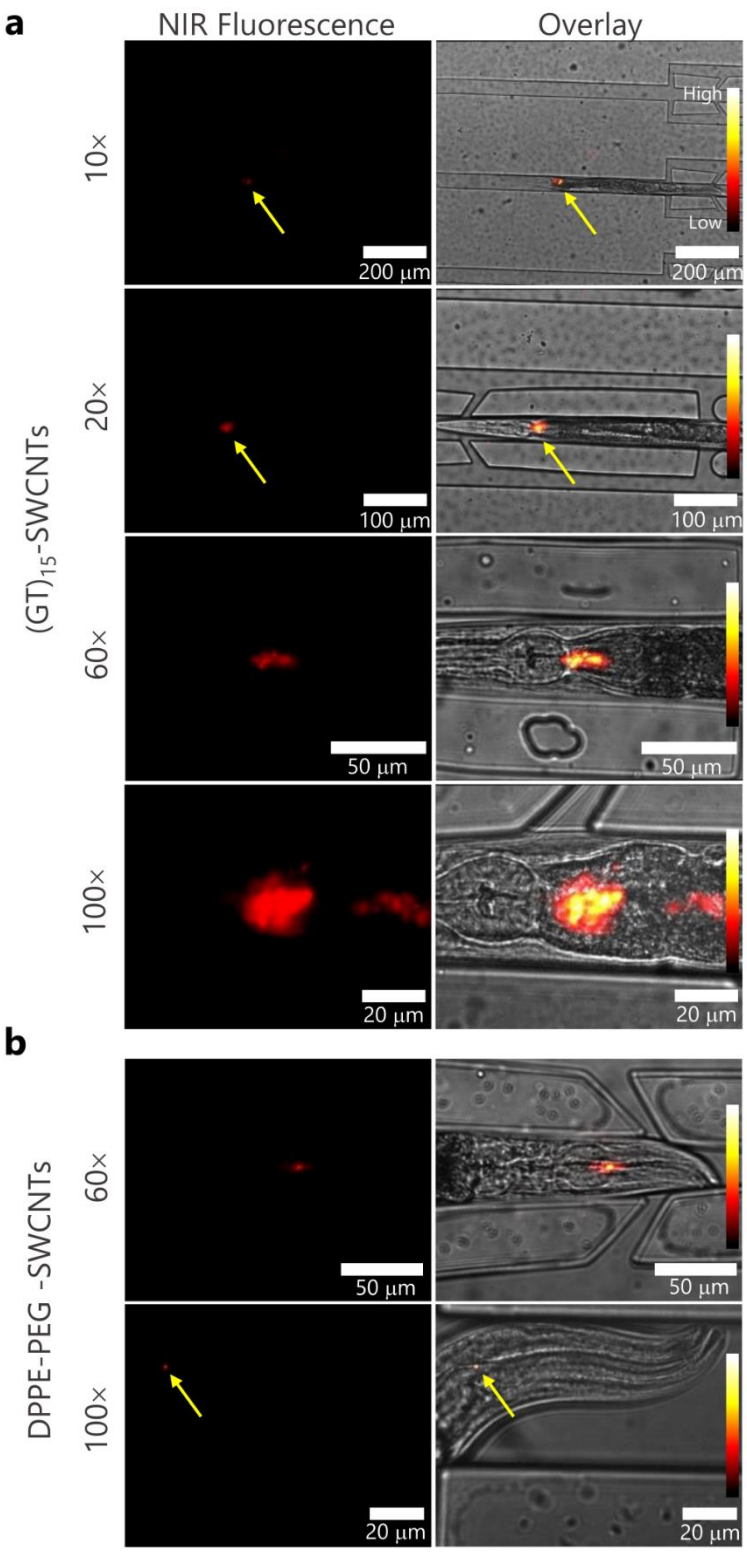

Figure 21. *In vivo* SWCNT imaging. NIR fluorescence images (left column) and brightfield-NIR overlay images (right column) of worms with a) internalized $(GT)_{15}$-SWCNTs at 10×, 20×, 60×, 100× magnifications, with scale bars of 200 µm, 100 µm, 50 µm, and 20 µm, respectively. b) Internalized DPPE-PEG-SWCNTs at 60×, and 100× magnifications, with scale bars of 50 µm, and 20 µm, respectively. The colorbars represent the NIR fluorescence intensity from low (dark red) to high (bright yellow).

One immediate observation was that the DNA-functionalized SWCNTs have a larger tendency to cluster within the worm compared to the PEGylated SWCNTs. This effect is attributed to the relatively larger hydrophilic layer of the PEG functionalization around the SWCNTs, which prevents individual SWCNTs from coming in close proximity with the surrounding ones. This fact is also evident in the feeding medium (**Figure 22**), where comparing the two classes of functionalized SWCNTs at the same concentrations, they exhibit distinct morphological features in their dispersion. The fact that the ssDNA-suspended SWCNTs are prone to clustering throughout the entire experimental work increases the ability to optically detect them, with smaller magnifications. Indeed, we managed to detect $(GT)_{15}$-SWCNTs clusters of $10-20$ μm in size, with a magnification as low as 10× (**Figure 21**a). This can be advantageous in cases where multiple worms need to be imaged simultaneously, and a large field of view (FOV) is required, such as in toxicity or chemotaxis assays, or when using SWCNTs as tracking markers for *C. elegans* nematodes in an automated detection system.[147,184–186]

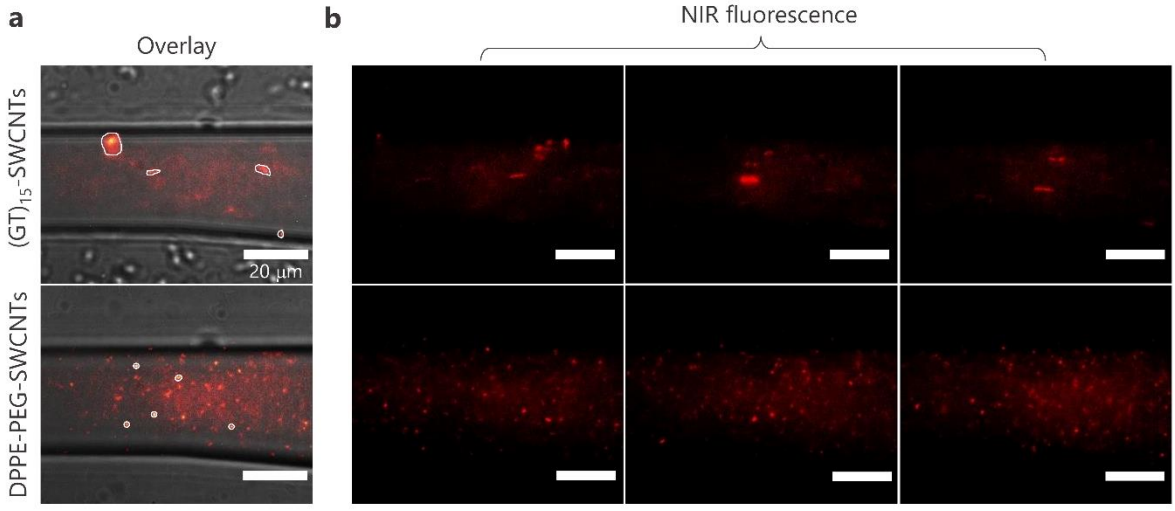

Figure 22. Comparison of feeding mediums within a microfluidic channel containing SWCNTs. 1 mg L^{-1} of $(GT)_{15}$-SWCNTs (top row) and 1 mg L^{-1} of DPPE-PEG-SWCNTs (bottom row), imaged with same exposure time (150 msec), showing both morphological and fluorescent intensity distinctions between the two types of SWCNTs. a) Overlay images (left column) of brightfield and NIR fluorescence taken with a 100× objective. Selected SWCNTs with varying size and shape are marked with white line contours. b) NIR fluorescent images (3 right columns) showing 3 additional observations of the same feeding mediums as manifested inside the microfluidic channel. All scale bars are 20 μm.

Detecting and imaging the DPPE-PEG-SWCNTs presented a distinct challenge. Their intake by the worms was less often detectable since they remained as individual particles or as very small bundles in the order of 1 μm, and could only be identified with the higher magnification setups. On rare occasions, small DPPE-PEG-SWCNTs bundles could be seen with the 60× magnification imaging, as shown in the worm's Metacorpus (**Figure 21**b). However, for most cases, the detection and imaging of DPPE-PEG-SWCNTs were made possible only through the 100× objective setup. Still, the DPPE-PEG-SWCNTs benefit from higher fluorescence intensity compared to their $(GT)_{15}$-SWCNTs counterparts and have better single-particle dynamics.

3.4. Immobilization effect on colocalization mismatch of autofluorescence and NIR channels

Multi-spectral imaging in *C. elegans* worms may become a challenge in an uncontrolled spatial environment since free-roaming worm locomotion in the presence of food or other chemotaxis cues is hectic. In order to exemplify the role of worm restriction by the microfluidic device, we compared the locomotion behavior of *C. elegans* in the spatially controlled and non-controlled environments using $(GT)_{15}$-SWCNTs as internalized probes. Indeed, the free-roaming worm covered a larger area within a field of view (FOV) compared to the worm that was confined within a microfluidic channel (**Figure 23**a and **Figure 23**b). In many cases, the free-roaming worms exited the static FOV within a short period of time, even when observed using a relatively small magnification with a 20× objective, rendering the worm's tracking and overlay imaging a challenging task. In contrast, the worms inside the microfluidic device were confined to a small area and were successfully imaged for at least 5 minutes (**Figure 23**c and **Figure 23**d).

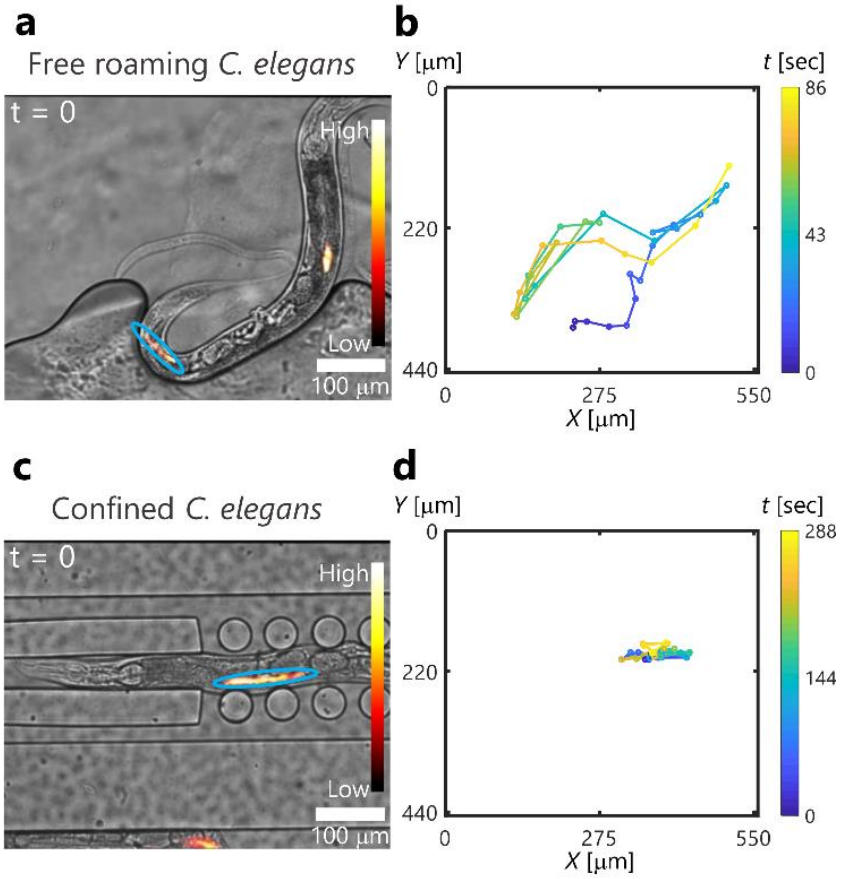

Figure 23. Tracking patterns comparison of SWCNT probes inside free roaming worms vs. confined worms. a) Brightfield and NIR overlay 20× image at $\boldsymbol{t = 0}$, with tracking ROI (blue) of $(GT)_{15}$-SWCNTs inside a free roaming *C. elegans*. b) Tracking graph of the SWCNTs inside the ROI in a free roaming *C. elegans* over a period of 86 seconds. c) Brightfield and NIR overlay 20× image at $\boldsymbol{t = 0}$, with tracking ROI (blue) of $(GT)_{15}$-SWCNTs inside a confined *C. elegans*. d) Tracking graph of the SWCNTs inside the ROI in a confined *C. elegans* over a period of 288 seconds. Graphs colorbar is the time evolution in seconds, Images colorbar represents the NIR fluorescence intensity from low (dark red) to high (bright yellow), scale bars are 100 μm.

Rapid movement of free-roaming worms poses an additional challenge on multi-spectral imaging (**Figure 24**). Specifically, physically rotating a filter turret within a microscope can take up to several seconds, and during the acquisition of consecutive frames of bright-field, visible fluorescence, and NIR fluorescence, the worm can substantially change its position. As a result, when overlaying the entire multi-spectral stack (**Figure 24**a), the combined image unravels the colocalization mismatch challenge **(Figure 24**b. In contrast, the limited degree of freedom of a confined worm only allowed for minor bends of its medial section, which resulted in a minor mismatch between the fluorescent channels, mainly the GFP and DAPI, to the brightfield and NIR channels (**Figure 24**c). Although

this undesirable effect was still observed in the confined worm, it was negligible compared to the free-roaming worm imaged under similar conditions (**Figure 24**b and **Figure 24**c), which exhibited significant mismatches that made colocalization impossible. Moreover, the confinement in the microfluidics platform allowed us to use a much higher magnification for multi-spectral overlaid imaging, such as 100×, which otherwise was not possible in a non-anesthetized free-roaming worm.

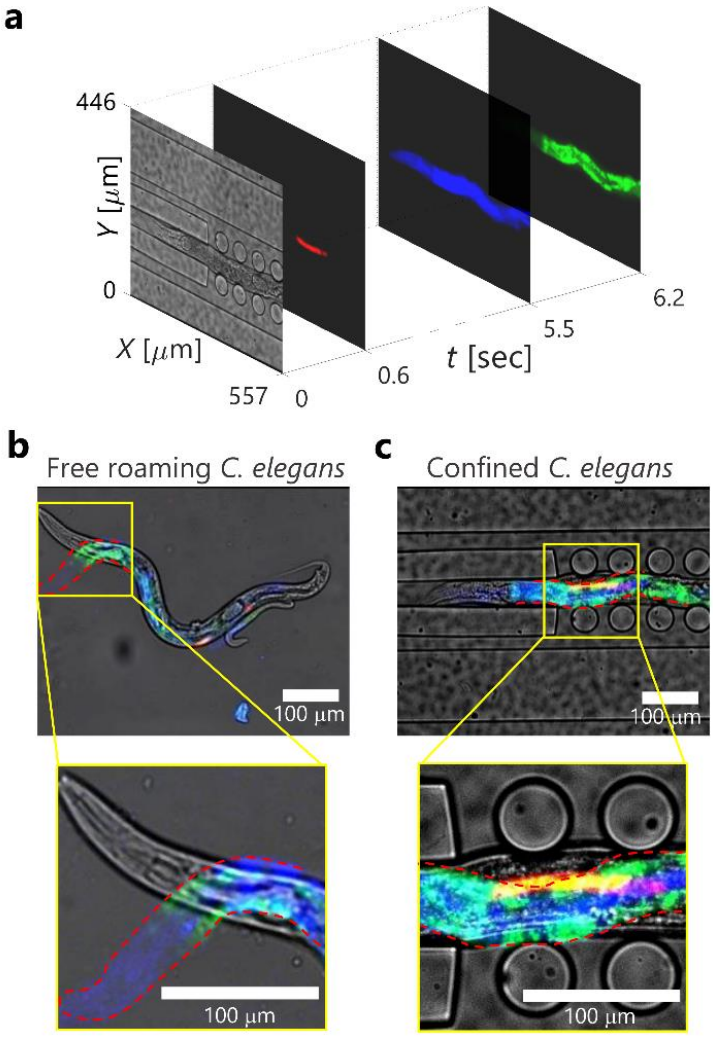

Figure 24. Worms confinement effect on colocalization mismatch of autofluorescence and NIR channels. a) 3D explosion of separated brightfield, NIR, DAPI, and GFP multichannel layering images acquired with 20× objective of a confined worm with $(GT)_{15}$-SWCNTs, showing the transfer time between filters. b) Overlay image of a free-roaming worm with $(GT)_{15}$-SWCNTs, showing (in zoom) a significant mismatch of the worm head (red dashed line) due to the delay of the GFP and DAPI channels after the brightfield image capture. Scale bars are 100 μm. c) Overlay image of a confined worm with $(GT)_{15}$-SWCNTs, showing a red dashed line marking the displacement of the worm during the time lapsed from first to last channel imaging seen in zoom, scale bars are 100 μm.

The NIR fluorescent signal of internalized SWCNTs could be detected in the worm's terminal bulb grinder and right passed the pharyngeal-intestinal valve, and could be overlaid with the worm's GFP and DAPI autofluorescence channels and the bright-field image (**Figure 25**). The FWHM of the NIR fluorescence clusters, in this case, was as small as 1 μm. This result highlights the capability to image functionalized SWCNTs in the NIR range, through the strong autofluorescence interference of the worm's intestinal granules.

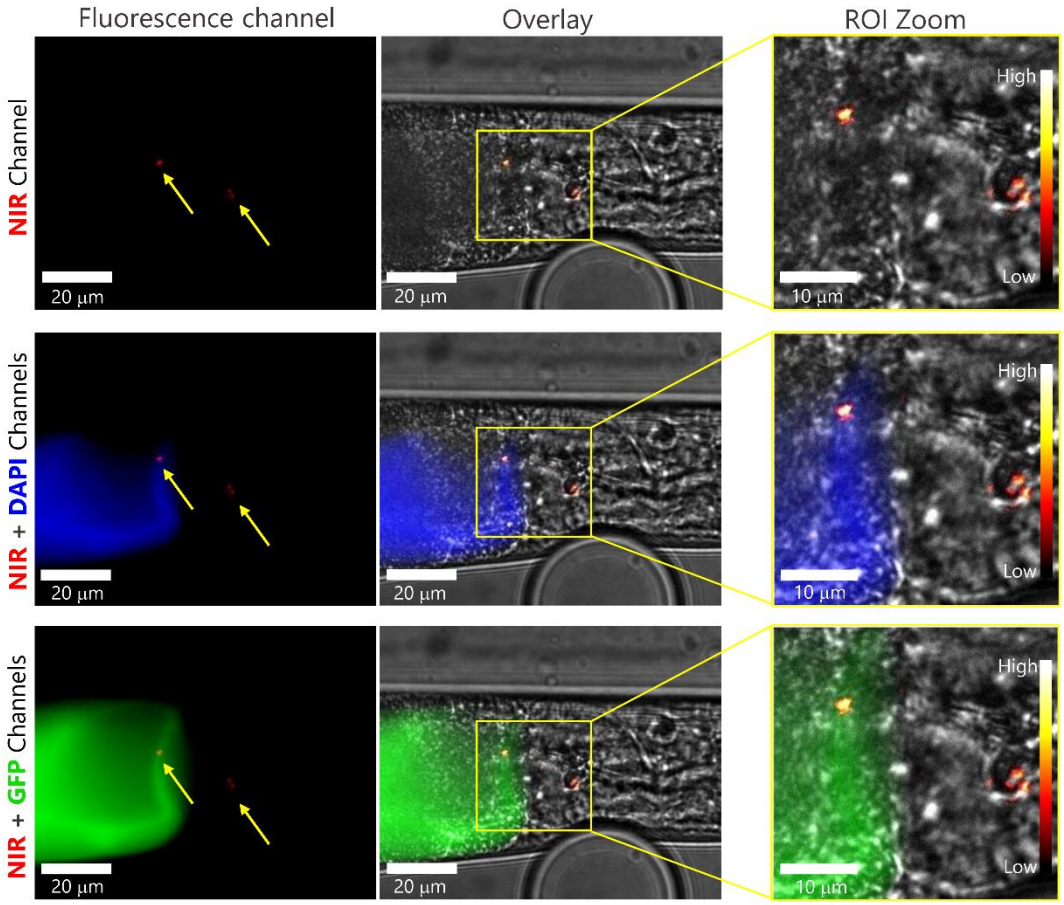

Figure 25. Spectral separation of NIR and visible wavelength images. Detailed images acquired with 100× objective of multichannel fluorescent imaging identifying two NIR fluorescent spots (yellow arrows) emitted by DPPE-PEG-SWCNTs, with the left one visible through both DAPI and GFP autofluorescence channels images. Left (NIR fluorescence), middle (overlay), and right (zoomed ROI) columns show the NIR (top row), NIR and DAPI channels (middle row), and NIR and GFP channels (bottom row) separately. Fluorescence column scale bars are 20 μm, overlay column scale bars are 20 μm, zoom column scale bars are 10 μm. The colorbars on the ROI zoom column images represent the NIR fluorescence intensity from low (dark red) to high (bright yellow).

3.5. Feeding profiles effect on SWCNTs internalization

The preliminary strategy adopted to internalize SWCNTs within *C. Elegans* worms relied on feeding methods used in earlier studies.[37,187,188] Specifically, worms were pre-incubated for a few hours in a feeding medium that contained *E. Coli* and SWCNTs, before loading them into the microfluidics channels and acquiring images over time. We performed pre-incubation cycles with either $(GT)_{15}$-SWCNTs or DPPE-PEG-SWCNTs for a minimum of 2 hours. Although in both cases we observed successful internalization of the SWCNTs, the $(GT)_{15}$-SWCNTs were more easily detectable as they were present as larger clusters deep within the intestinal bulb, in the intestinal 'twist' and posterior section (**Figure 26**a and **Figure 27**), whereas the DPPE-PEG-SWCNTs were found as smaller clusters in the corpus and terminal bulb parts of the worm's pharynx (**Figure 26**a). The $(GT)_{15}$-SWCNTs pre-incubation results were similar for longer periods of pre-incubation, namely, 3 and 4 hours (**Figure 26**b), showing accumulation in the pharyngeal–intestinal valve and the anterior part of the intestinal lumen as well as other internal sections (**Figure 27**). The clusters of the $(GT)_{15}$-SWCNTs that appeared following a few hours of pre-incubation and were observed irrespective of the feeding duration can be attributed to the morphological characteristics of the ssDNA-suspended SWCNTs as were first evident in the feeding medium itself (**Figure 22**) and could hint on similar binding affinities within the *C. elegans* digestive tract. Another reason can be linked to the gut microenvironment, consisting of a rich presence of proteins and other biomolecules within the intestinal lumen, such as C-type Lectin or mucins.[189,190] This can explain the differences we observed between the pre-incubation results of the $(GT)_{15}$-SWCNTs and the DPPE-PEG-SWCNTs, since, for the latter, the PEG corona can prevent nonspecific adsorption,[191] and therefore cluster formations are less pronounced.

In addition to pre-incubation with SWCNTs, we used a different internalization approach, in which we first loaded *C. Elegans* worms into the microfluidics device and exposed them to a feeding medium containing *E. Coli* and SWCNTs, while monitoring in real-time the intake and digestive progression of the SWCNTs for 2 hours (**Figure 26**c). The SWCNTs fluorescence could be detected in the meta-corpus and terminal-bulb as early as 15 minutes after the introduction of the SWCNTs, for both the $(GT)_{15}$-SWCNTs and the DPPE-PEG-SWCNTs, where fluorescence spots as small as 1 μm could be visualized. Throughout the imaging duration, we continuously observed intake of SWCNTs passing through the worm's pharynx and throughout the pharyngeal pathway, without large clustering in the worm's corpus, isthmus or terminal bulb, probably owing to the mechanical and structural properties of the pharynx where muscular walls create strong contractions during pumping.[53] Moreover, the mucus secreted in the pharynx provides a barrier to the wall's lining and may contribute to the prevention of such aggregations.[192,193] While the DPPE-PEG-SWCNTs did not form large clusters, rendering their tracking somewhat more challenging, the $(GT)_{15}$-SWCNTs began to accumulate and cluster in various internal segments of the worm's intestinal lumen approximately 90 minutes following their introduction, in agreement with the results of the pre-incubation internalization. Compared to the pre-incubation approach, in which the SWCNTs intake process cannot be captured, real-time imaging of the confined worms enabled us to monitor the intake dynamics of SWCNTs. This platform proposed thus provided us a new opportunity for scrutinizing and tracking the feeding process in real-time, in a controlled spatiotemporal setting.

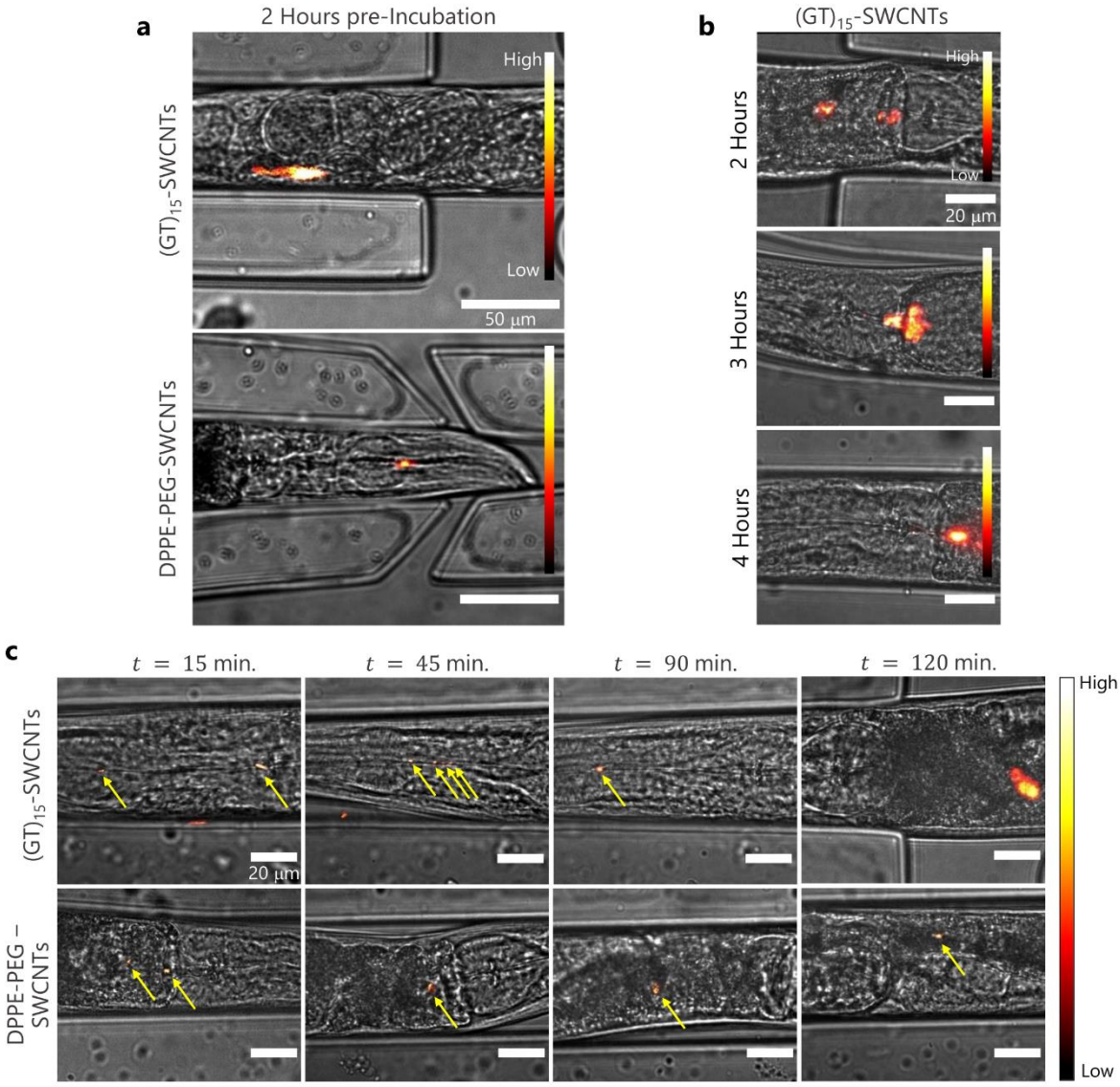

Figure 26. Pre-incubation vs. real-time feeding profiles. a) Overlay images (brightfield and NIR) of internalized $(GT)_{15}$-SWCNTs and DPPE-PEG-SWCNTs taken with 60× objective after pre-incubation feeding of 2 hours. Scale bars are 50 μm. b) Overlay images (brightfield and NIR) of internalized $(GT)_{15}$-SWCNTs at 2, 3, and 4 hours of pre-incubation feeding taken with a 100× objective, showing typical $(GT)_{15}$-SWCNTs clustering past the pharyngeal-intestinal valve and the front segment of the intestinal lumen. Scale bars are 20 μm. c) Overlay images (brightfield and NIR) of real-time feeding of $(GT)_{15}$-SWCNTs (top) and DPPE-PEG-SWCNTs (bottom) taken with a 100× objective during a 2-hour session showing dynamic ingestion of SWCNTs (yellow arrows) through the pharynx, and inside the intestinal lumen at $\boldsymbol{t = 15}$, 45, **90**, and **120** minutes. Scale bars are 20 μm. The colorbars represent the NIR fluorescence intensity from low (dark red) to high (bright yellow).

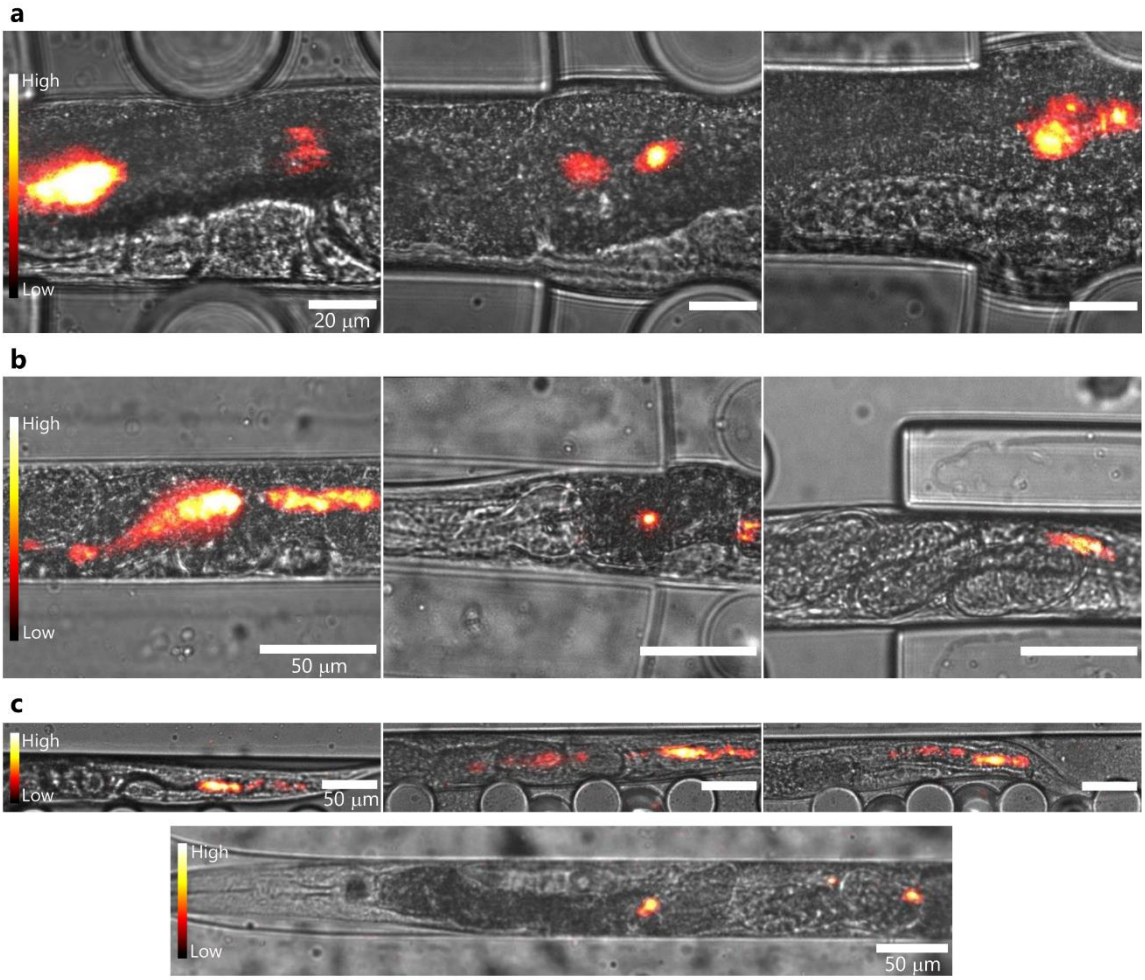

Figure 27. Overlay images (brightfield and NIR) of $(GT)_{15}$-SWCNTs clusters formations inside *C. elegans* worms after 2 hours of pre-incubation feeding. a) Cluster formations in the middle section of the intestine imaged with 100× objective, scale bars are 20 μm. b) Cluster formations in the anterior and middle sections of the intestine imaged with 60× objective, scale bars are 50 μm. c) SWCNTs distribution throughout the anterior, middle, and posterior sections of the worm imaged with 20× objective. Scale bars are 50 μm. The colorbars represent the NIR fluorescence intensity from low (dark red) to high (bright yellow).

3.6. Digestive path tracking

One of the advantages of using the microfluidics device for worm confinement and live imaging is the ability to identify and monitor a trajectory of functionalized SWCNTs through the digestive tract of the worm. Specifically, we successfully monitored the translocation of $(GT)_{15}$-SWCNTs through the anterior segment of the intestinal lumen (**Figure 28**a). During a period of 15 minutes, we observed a small cluster of SWCNTs, of approximately 5 μm in diameter (blue circle), displaced from a source cluster of approximately 10 μm in diameter (red circle), and progressed through the intestine lumen

toward the posterior section of the worm's intestinal lumen. The source cluster remained relatively stationary within the worm frame of reference, albeit the clusters' erratic motion resulting from the worm's motion back and forth along the fluidic channel. We measured the distance (**Figure 28**b) between the centers of the source cluster and the moving cluster as a function of time (green line) in the frames in which both were considered to be in focus according to our previously established criterion (**Figure 20**). In addition, we determined the distance between both the source cluster (red) and the moving cluster (blue) from a stationary reference point on the microfluidic device (yellow). The distance between the moving cluster and the source cluster exhibited a steady and continuous increase up to 120 μm. This distance is roughly equivalent to 13% of the average length of the adult hermaphrodite intestine and corresponds to a digestion speed of 8 μm min^{-1}. Studies have shown that the defecation cycle time of an adult *C. elegans* is 45 - 50 seconds.[54,194] However, transport and defecation times through an average adult *C. elegans* intestine depends on several factors, such as the type and quantity of food consumed, the age and health of the worm, and the environmental conditions. Specifically, when the food medium contains non-food particles, and the uptake is exhausted, particles start to accumulate within regions of the intestinal lumen, and the defecation process slows down to time scales of 15 minutes and higher.[195] These previous studies are in good agreement with the time-scale measured in this work.

While the $(GT)_{15}$-SWCNTs showed a higher tendency to cluster compared to the DPPE-PEG-SWCNTs, they enable detection and tracking in lower magnifications imaging, benefiting from a larger FOV. The DPPE-PEG-SWCNTs, on the other hand, could only be detected and imaged using the highest magnification 100x objective. This resulted in a relatively small FOV, of approximately 115 μm in width. Following 90 minutes of *C. elegans* feeding with DPPE-PEG-SWCNTs, we observed several NIR fluorescent signals,

of approximately 1 μm in diameter, and monitored their position (**Figure 28**c). Despite their strong fluorescence signal, accurately measuring the displacement of the NIR fluorescent cues was challenging due to their small size, the limited focal depth, and the small FOV. Nevertheless, we were able to qualitatively capture the trajectory of the DPPE-PEG-SWCNTs over a 25-minute interval. We observed distinct organelles within the worm, such as a portion of the anterior gonad sheath (indicated by a blue dashed line) and two oocytes (indicated by a green dashed line). We also marked two points of interest (labeled as I and II) and monitored the movement of the NIR signals relative to these reference points. We could clearly see that the DPPE-PEG-SWCNTs probes move deeper within the intestinal lumen.

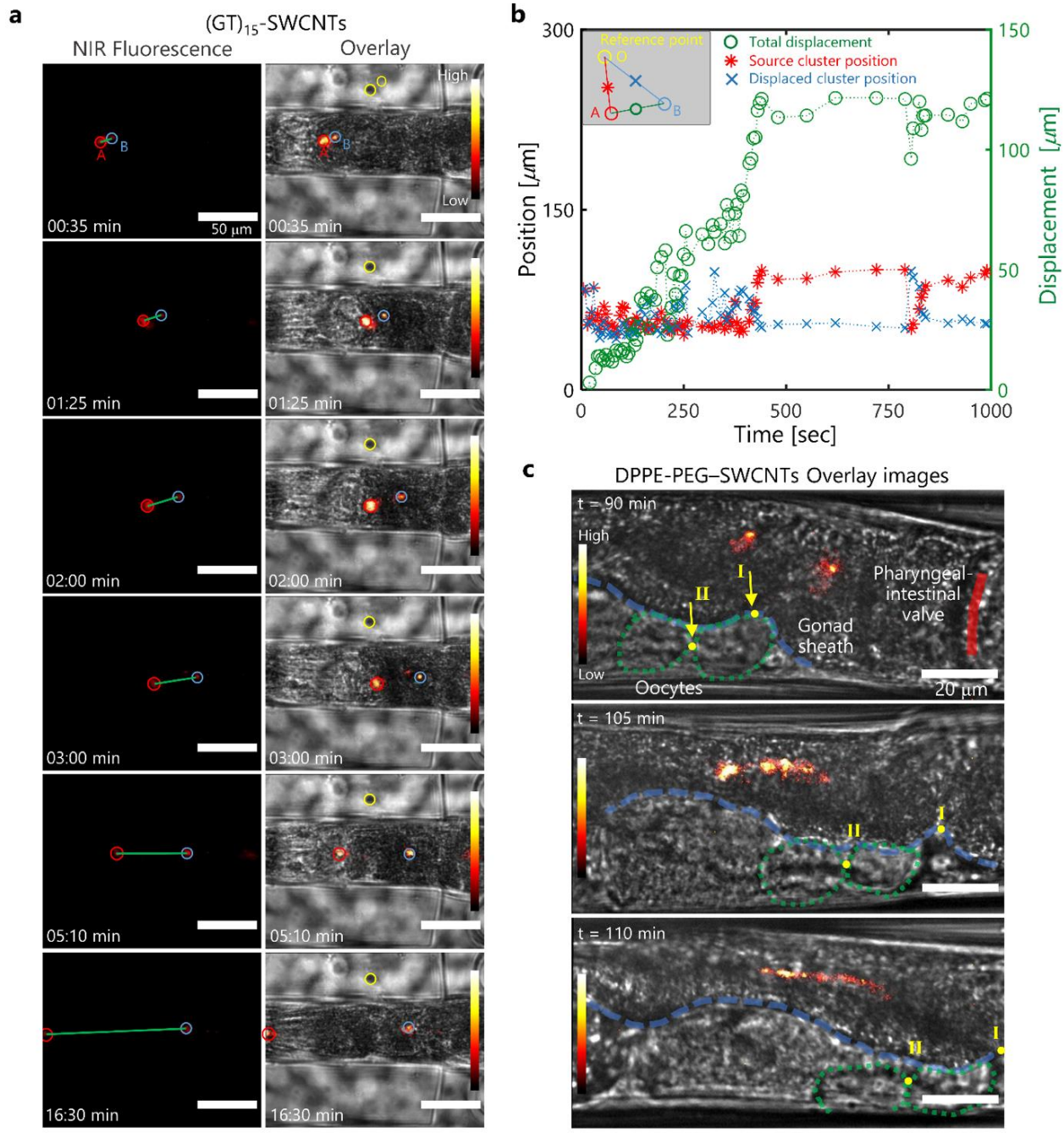

Figure 28. Spatiotemporal tracking of internalized SWCNTs. a) Displacement of internalized fluorescent $(GT)_{15}$-SWCNTs over time, imaged with a 60× objective shown in NIR fluorescent channel (left column) and brightfield-NIR overlay image (right column). Markers and labels are for SWCNTs source cluster position within the worm (red circle, A), SWCNTs of the displaced cluster position within the intestinal lumen of the worm (blue circle, B), a static reference point (yellow circle, O), and total displacement between the source cluster and the displaced cluster within the worm (green line). Scale bars are 50 µm. b) Total displacement measured over time between the SWCNTs from the source cluster and the displaced SWCNTs cluster (green), the SWCNTs source cluster relative position to the reference point (red), and the displaced SWCNTs cluster relative position to the reference point (blue). c) Overlay of brightfield and NIR fluorescence snapshots taken with a 100× objective showing a right-to-left trajectory of internalized DPPE-PEG-SWCNTs relative to reference features within the *C. elegans* worm. I is a point of reference on the gonad sheath (blue dashed curve), and II is a point of reference between the front oocytes (green dashed circles). The pharyngeal-intestinal valve is marked by a red curve. Scale bars are 20 µm. All image colorbars represent the NIR fluorescence intensity from low (dark red) to high (bright yellow).

We demonstrated that both the $(GT)_{15}$-SWCNTs and the DPPE-PEG-SWCNTs could be used for tracking within the digestive tract of the *C. elegans* worm confined in a microfluidics device. Although the DPPE-PEG-SWCNTs have higher fluorescence intensity, the $(GT)_{15}$-SWCNTs were preferable for the detection and monitoring of food trajectory owing to larger FOV given the ability to use lower magnification for fluorescence imaging. In terms of temporal resolution, our platform provided a satisfactory temporal resolution for the purpose of tracking SWCNT probes within the intestine. However, for specific requirements such as monitoring pharyngeal pumping behaviors where short temporal dynamics dominate, or tracking SWCNT probes in conjunction with other fluorescent dyes where heavy multispectral overlaying is needed and colocalization is challenging, the imaging setup should be adapted accordingly by, for example, modifications to the microscope filter turret and dichroic mirrors, optical parallelization or even a more sensitive camera sensor which allows shorter exposure times.

4. Conclusion and summary

Biological and biomedical research, among many others, has long aimed to visualize and analyze the physiological processes of living organisms in real-time. NIR imaging techniques have recently become a valuable non-invasive tool for *in vivo* imaging, due to the distinct characteristics of NIR light, including low tissue autofluorescence and the ability to penetrate deep into tissues. Although using NIR fluorescent materials also has its challenges, such as specialized imaging equipment, and possibly higher costs, with careful evaluation of the research needs, one can benefit extensively from the unique properties of NIR imaging. One notable organism that has been frequently employed as a research model, is the *C. elegans* nematode, which has been used to study environmental toxicity, human diseases, host-parasite interactions, and developmental biology.[8,196–198] Due to its ease of genetic manipulation and a significant level of molecular and cellular similarity with humans, this organism is highly advantageous for research purposes.[1,2] Although the strong autofluorescence sourcing from the *C. elegans* internal organs, such as the uterus and intestine, in the entire visible spectrum is extensively harnessed for many research fields, it covers most of the worm's body and in many experimental cases interferes spatially and spectrally with external fluorescent markers. However, *C. elegans* show no autofluorescence in the NIR spectral range (>900 nm), thus allowing the use of NIR fluorescent SWCNTs as efficient biomarkers, sensors, and tracking agents within the worm's entire volume.

The internalization of SWCNTs inside *C. elegans* organisms has been explored in the past for various research fields, yet in a very ill-controlled spatiotemporal setting. Rapid locomotion of the worms presented colocalization artifacts, and the worm's anesthetic immobilization affected the physiological parameters.

In our work, we assembled a spatially and temporally controlled NIR imaging platform that utilizes the advantages of using the wild-type C. elegans nematodes as an *in vivo* organism model with functionalized SWCNTs as NIR fluorescent markers, all in a microfluidic device used for worm's stress-free immobilization that does not require anesthesia. Owing to their biocompatibility, we chose two widely used types of functionalized SWCNTs as our NIR fluorescent markers, single-stranded DNA SWCNTs ((GT)15-SWCNTs), and phospholipid PEGylated SWCNTS ((DPPE)-PEG (5 kDa)-SWCNTs). We internalized the functionalized SWCNTs in the *C. elegans* worms through food intake with *E. coli* bacteria (OP50) broth, following their immobilization inside microfluidic device confinement channels. First, we showed a method to correctly detect and label candidate SWCNT particles within the *C. elegans* digestive tract. The proposed method utilized Z-stacking NIR imaging to measure "in-focus" fluorescent signals. Furthermore, we measured the SWCNTs' synchronized motion with the worm's body to reassure the intra-corporeal presence of the SWCNTs. Live NIR and brightfield overlaid images of the worm's pharyngeal corpus and terminal bulb grinder were used to set the focal plane for SWCNTs intake and tracking. Once we were able to reproduce the detection of fluorescent SWCNTs within the worm's pharynx and intestine, we showed the ability to image the SWCNTs with various optical settings. We identified large cluster formations of (GT)15-SWCNTs in low magnifications (10×), in contrast to small cluster formation of (DPPE)-PEG (5 kDa)-SWCNTs which could only be detected in higher magnifications (> 60×).

While spectral separation of the SWCNTs' NIR fluorescence and the worm's visible autofluorescence (at the GFP and DAPI channels) was previously proven,[37] it was never before tested without the use of anesthetic means of immobilization. In our study, we utilized a microfluidic device and created a stress-free environment for the free-roaming

C. elegans worms, allowing us to successfully image both the worm's visible autofluorescence and the SWCNTs' NIR fluorescence spectral ranges and colocalize them with minimal misalignment. In contrast, visible and NIR dual channel imaging of un-anesthetized worms on agar treated glass slide suffered from significant misalignment between NIR, DAPI and GFP channels, and colocalization was nearly impossible in most cases.

Another new important functionality we demonstrated in our work is real-time NIR imaging and tracking of SWCNT intake in un-anesthetized and yet immobilized C. elegans worms. Initially, we observed and characterized the intake of ssDNA SWCNTs and PEGylated SWCNTs during live imaging and were able to identify the fluorescent SWCNT particles in the worm's corpus and terminal bulb from the first minutes of the feeding process. Our results from the 2 hours real-time feeding imaging were in good agreement with the intake picture we observed in worms that were pre-incubated with SWCNTs for 2-4 hours. Most notably, after approximately 2 hours of feeding (in both methods), the (GT)15-SWCNTs started accumulating in the anterior parts of the worm's intestinal lumen, creating distinct trackable clusters. The DPPE-PEG-SWCNTs, on the other hand, showed little to no clustering throughout the real-time feeding and were detectable only with the high magnification (100×), which, again, matched our pre-incubation (>2 hours) observations, where distinct clusters were hardly noticeable. Further, we also succeeded in tracking and measuring the (GT)15-SWCNTs trajectory through an anterior part of the intestine owing to the easily detectable ssDNA SWCNTs clusters in lower magnifications with larger FOV. The DPPE-PEG-SWCNTs intestinal trajectories were indeed recognized due to their higher fluorescence signal, however, their small spot sizes limited our tracking capabilities to higher magnifications and smaller FOV.

In summary, we were able to demonstrate a method to image, detect, and track two types of functionalized NIR fluorescent SWCNTs that were internalized via food intake into wild-type C. elegans worms confined within a microfluidic device. We showed improved colocalization of multi-spectral fluorescence imaging and revalidated the spatial freedom of NIR fluorescence probes within a highly visible autofluorescence environment of the *C. elegans*. Finally, we showcased a spatiotemporally controlled platform and a method to track and characterize, with real-time feeding, different intake behaviors of fluorescent nano-sensors using two types of SWCNTs, the (GT)15-SWCNTs and the DPPE-PEG-SWCNTs, each expressed different uptake, accumulation, detectability, and dynamics throughout the feeding process owing to their specific molecular complexes and optical characteristics.

Our work holds significant promise for advancing various areas of scientific research and biomedical applications such as NIR imaging advancements where this technology could revolutionize our ability to monitor and study biological processes in real-time within living organisms. Future research can further optimize the use of SWCNTs for enhanced imaging, potentially enabling the study of complex physiological processes with high spatiotemporal resolution. Moreover, functionalized SWCNTs variations opens the door to a wide range of applications, including investigating feeding behaviors in nematodes, toxicity studies, tracking neuronal pathways or studying embryonic development. Researchers can employ SWCNTs in different ways to answer specific questions, for example, targeted drug delivery systems or the assessment of treatment efficacy at a cellular level using tailored SWCNTs.

The microfluidic devices and the imaging setups can be tailored and rendered to fit other relevant needs with increased performance, such as conducting multiple parallel worms imaging with large group quantitative statistics, by customizing the microscopy setup and

programming a motorized state such that consecutive images can be captured from several regions of interest including different areas of the same worm, or interesting areas in different worms in adjacent channels. Further, the temporal resolution can also be increased by modifications to the microscope filter turret, dichroic mirrors, optical parallelization, or even a higher sensitivity grade of the camera sensor, which allows shorter exposure times. This will support experiments with fast dynamics analysis and heavy multispectral overlaying with challenging colocalization. Future research can focus on developing specialized microfluidic setups to mimic specific physiological conditions or create controlled environments for different organisms or cell types.

This research represents a significant step forward in biomedical imaging and offers a wide range of possibilities for future research. It has the potential to impact not only the field of biology but also nanotechnology, materials science, and medicine, paving the way for innovative discoveries and applications in the years to come.

5. References

(1) Kaletta, T.; Hengartner, M. O. Finding Function in Novel Targets: C. Elegans as a Model Organism. *Nat. Rev. Drug Discov.* **2006**, *5* (5), 387–399. https://doi.org/10.1038/nrd2031.

(2) Corsi, A. K. A Transparent Window into Biology: A Primer on Caenorhabditis Elegans. *WormBook* **2015**, 1–31. https://doi.org/10.1895/wormbook.1.177.1.

(3) Tissenbaum, H. A. Using C. Elegans for Aging Research. *Invertebrate Reproduction and Development*. Taylor and Francis Ltd. January 30, 2015, pp 59–63. https://doi.org/10.1080/07924259.2014.940470.

(4) Agarwal, P.; Shemesh, T.; Zaidel-Bar, R. Directed Cell Invasion and Asymmetric Adhesion Drive Tissue Elongation and Turning in C. Elegans Gonad Morphogenesis. *Dev. Cell* **2022**, *57* (17), 2111-2126.e6. https://doi.org/10.1016/j.devcel.2022.08.003.

(5) Rechavi, O.; Houri-Ze'evi, L.; Anava, S.; Goh, W. S. S.; Kerk, S. Y.; Hannon, G. J.; Hobert, O. Starvation-Induced Transgenerational Inheritance of Small RNAs in C. Elegans. *Cell* **2014**, *158* (2), 277–287. https://doi.org/10.1016/j.cell.2014.06.020.

(6) Ewe, C. K.; Rechavi, O. The Third Barrier to Transgenerational Inheritance in Animals: Somatic Epigenetic Resetting. *EMBO Rep.* **2023**, *24* (4), 1–7. https://doi.org/10.15252/embr.202256615.

(7) Gubert, P.; Gubert, G.; Oliveira, R. C. De; Fernandes, I. C. O.; Bezerra, I. C.; Ramos, B. De; Lima, M. F. De; Rodrigues, D. T.; Cruz, A. F. N. da; Pereira, E. C.; Ávila, D. S.; Mosca, D. H. Caenorhabditis Elegans as a Prediction Platform for Nanotechnology-Based Strategies: Insights on Analytical Challenges. *Toxics*

2023, *11* (3), 239. https://doi.org/10.3390/toxics11030239.

(8) Culetto, E.; Sattelle, D. B. A Role for Caenorhabditis Elegans in Understanding the Function and Interactions of Human Disease Genes. *Hum. Mol. Genet.* **2000**, *9* (6), 869–877.

(9) Silverman, G. A.; Luke, C. J.; Bhatia, S. R.; Long, O. S.; Vetica, A. C.; Perlmutter, D. H.; Pak, S. C. Modeling Molecular and Cellular Aspects of Human Disease Using the Nematode Caenorhabditis Elegans. *Pediatr. Res.* **2009**, *65* (1), 10–18. https://doi.org/10.1203/PDR.0b013e31819009b0.

(10) Lockshin, R. A.; Zakeri, Z. Cell Death in Health and Disease: Angiogenesis Review Series. *J. Cell. Mol. Med.* **2007**, *11* (6), 1214–1224. https://doi.org/10.1111/j.1582-4934.2007.00150.x.

(11) Ellis, H. Genetic Control of Programmed Cell Death in the Nematode C. Elegans. *Cell* **1986**, *44* (6), 817–829. https://doi.org/10.1016/0092-8674(86)90004-8.

(12) Lettre, G.; Hengartner, M. O. Developmental Apoptosis in C. Elegans: A Complex CEDnario. *Nat. Rev. Mol. Cell Biol.* **2006**, *7* (2), 97–108. https://doi.org/10.1038/nrm1836.

(13) Lukácsi, S.; Farkas, Z.; Saskői, É.; Bajtay, Z.; Takács-Vellai, K. Conserved and Distinct Elements of Phagocytosis in Human and C. Elegans. *Int. J. Mol. Sci.* **2021**, *22* (16), 8934. https://doi.org/10.3390/ijms22168934.

(14) Crook, M.; Upadhyay, A.; Hanna-Rose, W. Necrosis in C. Elegans. In *Methods in Molecular Biology*; 2013; Vol. 1004, pp 171–182. https://doi.org/10.1007/978-1-62703-383-1_13.

(15) Kirienko, N. V.; Mani, K.; Fay, D. S. Cancer Models in Caenorhabditis Elegans. *Dev. Dyn.* **2010**, *239* (5), 1413–1448. https://doi.org/10.1002/dvdy.22247.

(16) Kyriakakis, E.; Markaki, M.; Tavernarakis, N. Caenorhabditis Elegans as a Model

for Cancer Research. *Mol. Cell. Oncol.* **2015**, *2* (2), e975027. https://doi.org/10.4161/23723556.2014.975027.

(17) Roussos, A.; Kitopoulou, K.; Borbolis, F.; Palikaras, K. Caenorhabditis Elegans as a Model System to Study Human Neurodegenerative Disorders. *Biomolecules* **2023**, *13* (3), 478. https://doi.org/10.3390/biom13030478.

(18) Caldwell, K. A.; Willicott, C. W.; Caldwell, G. A. Modeling Neurodegeneration in Caenorhabditis Elegans. *Dis. Model. Mech.* **2020**, *13* (10), dmm046110. https://doi.org/10.1242/dmm.046110.

(19) Uno, M.; Nishida, E. Lifespan-Regulating Genes in C. Elegans. *npj Aging Mech. Dis.* **2016**, *2* (1), 16010. https://doi.org/10.1038/npjamd.2016.10.

(20) Giunti, S.; Andersen, N.; Rayes, D.; De Rosa, M. J. Drug Discovery: Insights from the Invertebrate Caenorhabditis Elegans. *Pharmacol. Res. Perspect.* **2021**, *9* (2), e00721. https://doi.org/10.1002/PRP2.721.

(21) Powell, J. R.; Ausubel, F. M. Models of Caenorhabditis Elegans Infection by Bacterial and Fungal Pathogens. *Methods Mol. Biol.* **2008**, *415*, 403–427. https://doi.org/10.1007/978-1-59745-570-1_24/COVER.

(22) Mudd, N.; Liceaga, A. M. Caenorhabditis Elegans as an in Vivo Model for Food Bioactives: A Review. *Curr. Res. Food Sci.* **2022**, *5* (May), 845–856. https://doi.org/10.1016/j.crfs.2022.05.001.

(23) Hermann, G. J.; Schroeder, L. K.; Hieb, C. A.; Kershner, A. M.; Rabbitts, B. M.; Fonarev, P.; Grant, B. D.; Priess, J. R. Genetic Analysis of Lysosomal Trafficking in Caenorhabditis Elegans. *Mol. Biol. Cell* **2005**, *16*, 3273–3288. https://doi.org/10.1091/mbc.E05-01-0060.

(24) Chalfie, M.; Tu, Y.; Euskirchen, G.; Ward, W. W.; Prasher, D. C. Green Fluorescent Protein as a Marker for Gene Expression. *Science* **1994**, *263* (5148),

802–805. https://doi.org/10.1126/science.8303295.

(25) Fire, A.; Harrison, S. W.; Dixon, D. A Modular Set of LacZ Fusion Vectors for Studying Gene Expression in Caenorhabditis Elegans. *Gene* **1990**, *93* (2), 189–198. https://doi.org/10.1016/0378-1119(90)90224-F.

(26) Hobert, O.; Loria, P. Uses of GFP in Caenorhabditis Elegans; Chalfie, M., R. Kain, S., Eds.; Wiley, 2005; pp 203–226. https://doi.org/10.1002/0471739499.ch10.

(27) Ji, N.; van Oudenaarden, A. Single Molecule Fluorescent in Situ Hybridization (SmFISH) of C. Elegans Worms and Embryos. *WormBook* **2012**, 1–16. https://doi.org/10.1895/wormbook.1.153.1.

(28) Porta-de-la-Riva, M.; Fontrodona, L.; Villanueva, A.; Cerón, J. Basic Caenorhabditis Elegans Methods: Synchronization and Observation. *J. Vis. Exp.* **2012**, No. 64, e4019. https://doi.org/10.3791/4019.

(29) Feinberg, E. H.; VanHoven, M. K.; Bendesky, A.; Wang, G.; Fetter, R. D.; Shen, K.; Bargmann, C. I. GFP Reconstitution Across Synaptic Partners (GRASP) Defines Cell Contacts and Synapses in Living Nervous Systems. *Neuron* **2008**, *57* (3), 353–363. https://doi.org/10.1016/j.neuron.2007.11.030.

(30) Boulin, T.; Etchberger, J. F.; Hobert, O. *Reporter Gene Fusions*.; The C. elegans Research Community, Ed.; WormBook Research Community: Pasadena, 2006. https://doi.org/10.1895/wormbook.1.106.1.

(31) Pincus, Z.; Mazer, T. C.; Slack, F. J. Autofluorescence as a Measure of Senescence in C. Elegans: Look to Red, Not Blue or Green. *Aging (Albany. NY).* **2016**, *8* (5), 889–898. https://doi.org/10.18632/aging.100936.

(32) Anderson, G. L.; Dusenbery, D. B.; Davis, B. O. Total Luminescence Spectroscopy of Fluorescence Changes during Aging in Caenorhabditis Elegans.

Biochemistry **1982**, *21* (17), 4089–4095. https://doi.org/10.1021/BI00260A027/ASSET/BI00260A027.FP.PNG_V03.

(33) Forge, T. A.; Macguidwin, A. E. Nematode Autofluorescence and Its Use as an Indicator of Viability. *J. Nematol.* **1989**, *21* (3), 399–403.

(34) Monici, M. Cell and Tissue Autofluorescence Research and Diagnostic Applications. *Biotechnol. Annu. Rev.* **2005**, *11* (SUPPL.), 227–256. https://doi.org/10.1016/S1387-2656(05)11007-2.

(35) Klass, M. R. Aging in the Nematode Caenorhabditis Elegans: Major Biological and Environmental Factors Influencing Life Span. *Mech. Ageing Dev.* **1977**, *6* (6), 413–429. https://doi.org/10.1016/0047-6374(77)90043-4.

(36) Clokey, G. V.; Jacobson, L. A. The Autofluorescent "Lipofuscin Granules" in the Intestinal Cells of Caenorhabditis Elegans Are Secondary Lysosomes. *Mech. Ageing Dev.* **1986**, *35* (1), 79–94. https://doi.org/10.1016/0047-6374(86)90068-0.

(37) Hendler-Neumark, A.; Wulf, V.; Bisker, G. In Vivo Imaging of Fluorescent Single-Walled Carbon Nanotubes within C. Elegans Nematodes in the near-Infrared Window. *Mater. Today Bio* **2021**, *12* (November), 100175. https://doi.org/10.1016/j.mtbio.2021.100175.

(38) Macarthur, R. H.; Pianka, E. R. ON OPTIMAL USE OF A PATCHY ENVIRONMENT There Is a Close Parallel between the Development of Theories in Economics and Population Biology . In Biology , However , the Geometry of the Organisms and Their Environment Plays a Greater Role . Different Phenotyp. *Am. Nat.* **1966**, *100* (916), 603–609.

(39) Larsen, C. S. Animal Source Foods and Human Health during Evolution. *J. Nutr.* **2003**, *133* (11), 3893S-3897S. https://doi.org/10.1093/jn/133.11.3893S.

(40) Trepanowski, J. F.; Canale, R. E.; Marshall, K. E.; Kabir, M. M.; Bloomer, R. J.

Impact of Caloric and Dietary Restriction Regimens on Markers of Health and Longevity in Humans and Animals: A Summary of Available Findings. *Nutr. J.* **2011**, *10* (1), 1–13. https://doi.org/10.1186/1475-2891-10-107.

(41) Balasubramanian, P.; Howell, P. R.; Anderson, R. M. Aging and Caloric Restriction Research: A Biological Perspective With Translational Potential. *EBioMedicine* **2017**, *21*, 37–44. https://doi.org/10.1016/j.ebiom.2017.06.015.

(42) Mattson, M. P.; Allison, D. B.; Fontana, L.; Harvie, M.; Longo, V. D.; Malaisse, W. J.; Mosley, M.; Notterpek, L.; Ravussin, E.; Scheer, F. A. J. L.; Seyfried, T. N.; Varady, K. A.; Panda, S. Meal Frequency and Timing in Health and Disease. *Proc. Natl. Acad. Sci.* **2014**, *111* (47), 16647–16653. https://doi.org/10.1073/pnas.1413965111.

(43) Djalalinia, S.; Qorbani, M.; Peykari, N.; Kelishadi, R. Health Impacts of Obesity - Obesity Canada. *Pak J Med Sci* **2015**, *31* (1), 239–242.

(44) Zheng, S. Q.; Ding, A. J.; Li, G. P.; Wu, G. S.; Luo, H. R. Drug Absorption Efficiency in Caenorhbditis Elegans Delivered by Different Methods. *PLoS One* **2013**, *8* (2), e56877. https://doi.org/10.1371/JOURNAL.PONE.0056877.

(45) Wu, T.; Xu, H.; Liang, X.; Tang, M. Caenorhabditis Elegans as a Complete Model Organism for Biosafety Assessments of Nanoparticles. *Chemosphere* **2019**, *221*, 708–726. https://doi.org/10.1016/J.CHEMOSPHERE.2019.01.021.

(46) Charão, M. F.; Souto, C.; Brucker, N.; Barth, A.; Jornada, D. S.; Fagundez, D.; Ávila, D. S.; Eifler-Lima, V. L.; Guterres, S. S.; Pohlmann, A. R.; Garcia, S. C. Caenorhabditis Elegans as an Alternative in Vivo Model to Determine Oral Uptake, Nanotoxicity, and Efficacy of Melatonin-Loaded Lipid-Core Nanocapsules on Paraquat Damage. *Int. J. Nanomedicine* **2015**, *10*, 5093–5106. https://doi.org/10.2147/IJN.S84909.

(47) Jung, S.-K.; Qu, X.; Aleman-Meza, B.; Wang, T.; Riepe, C.; Liu, Z.; Li, Q.; Zhong, W. Multi-Endpoint, High-Throughput Study of Nanomaterial Toxicity in Caenorhabditis Elegans. *Environ. Sci. Technol.* **2015**, *49* (4), 2477–2485. https://doi.org/10.1021/es5056462.

(48) Gonzalez-Moragas, L.; Berto, P.; Vilches, C.; Quidant, R.; Kolovou, A.; Santarella-Mellwig, R.; Schwab, Y.; Stürzenbaum, S.; Roig, A.; Laromaine, A. In Vivo Testing of Gold Nanoparticles Using the Caenorhabditis Elegans Model Organism. *Acta Biomater.* **2017**, *53*, 598–609. https://doi.org/10.1016/j.actbio.2017.01.080.

(49) Yang, X.; Jiang, C.; Hsu-Kim, H.; Badireddy, A. R.; Dykstra, M.; Wiesner, M.; Hinton, D. E.; Meyer, J. N. Silver Nanoparticle Behavior, Uptake, and Toxicity in Caenorhabditis Elegans : Effects of Natural Organic Matter. *Environ. Sci. Technol.* **2014**, *48* (6), 3486–3495. https://doi.org/10.1021/es404444n.

(50) Eom, H. J.; Roca, C. P.; Roh, J. Y.; Chatterjee, N.; Jeong, J. S.; Shim, I.; Kim, H. M.; Kim, P. J.; Choi, K.; Giralt, F.; Choi, J. A Systems Toxicology Approach on the Mechanism of Uptake and Toxicity of MWCNT in Caenorhabditis Elegans. *Chem. Biol. Interact.* **2015**, *239*, 153–163. https://doi.org/10.1016/j.cbi.2015.06.031.

(51) Chen, P. H.; Hsiao, K. M.; Chou, C. C. Molecular Characterization of Toxicity Mechanism of Single-Walled Carbon Nanotubes. *Biomaterials* **2013**, *34* (22), 5661–5669. https://doi.org/10.1016/j.biomaterials.2013.03.093.

(52) Altun, Z. F.; Hall, D. H. WormAtlas Hermaphrodite Handbook - Alimentary System - Pharynx. *WormAtlas* **2003**. https://doi.org/10.3908/wormatlas.1.3.

(53) Avery, L.; Shtonda, B. B. Food Transport in the C. Elegans Pharynx. *J. Exp. Biol.* **2003**, *206* (Pt 14), 2441–2457. https://doi.org/10.1242/jeb.00433.

(54) Liu, D. W.; Thomas, J. H. Regulation of a Periodic Motor Program in C. Elegans. *J. Neurosci.* **1994**, *14* (4), 1953–1962. https://doi.org/10.1523/JNEUROSCI.14-04-01953.1994.

(55) Herman, M. A.; Irazoqui, J. E.; Samuel, B. S.; Vega, N. Editorial: C. Elegans Host-Microbiome Interactions: From Medical to Ecological and Evolutionary Model. *Front. Cell. Infect. Microbiol.* **2022**, *12* (September), 1035545. https://doi.org/10.3389/fcimb.2022.1035545.

(56) Iwanaga, S.; Bok, L. L. Recent Advances in the Innate Immunity of Invertebrate Animals. *J. Biochem. Mol. Biol.* **2005**, *38* (2), 128–150. https://doi.org/10.5483/bmbrep.2005.38.2.128.

(57) Dushay, M. S.; Eldon, E. D. Drosophila Immune Responses as Models for Human Immunity. *Am. J. Hum. Genet.* **1998**, *62* (1), 10–14. https://doi.org/10.1086/301694.

(58) Mahajan-Miklos, S.; Tan, M. W.; Rahme, L. G.; Ausubel, F. M. Molecular Mechanisms of Bacterial Virulence Elucidated Using a Pseudomonas Aeruginosa-Caenorhabditis Elegans Pathogenesis Model. *Cell* **1999**, *96* (1), 47–56. https://doi.org/10.1016/S0092-8674(00)80958-7.

(59) Tan, M.-W.; Mahajan-Miklos, S.; Ausubel, F. M. Killing of Caenorhabditis Elegans by Pseudomonas Aeruginosa Used to Model Mammalian Bacterial Pathogenesis. *Proc. Natl. Acad. Sci.* **1999**, *96* (2), 715–720. https://doi.org/10.1073/pnas.96.2.715.

(60) Zhang, Y.-P.; Zhang, W.-H.; Zhang, P.; Li, Q.; Sun, Y.; Wang, J.-W.; Zhang, S. O.; Cai, T.; Zhan, C.; Dong, M.-Q. Intestine-Specific Removal of DAF-2 Nearly Doubles Lifespan in Caenorhabditis Elegans with Little Fitness Cost. *Nat. Commun.* **2022**, *13* (1), 6339. https://doi.org/10.1038/s41467-022-33850-4.

(61) Suzuki, Y.; Kikuchi, K.; Numayama-Tsuruta, K.; Ishikawa, T. Reciprocating Intestinal Flows Enhance Glucose Uptake in C. Elegans. *Sci. Rep.* **2022**, *12* (1), 15310. https://doi.org/10.1038/s41598-022-18968-1.

(62) Kumar, S.; Egan, B. M.; Kocsisova, Z.; Schneider, D. L.; Murphy, J. T.; Diwan, A.; Kornfeld, K. Lifespan Extension in C. Elegans Caused by Bacterial Colonization of the Intestine and Subsequent Activation of an Innate Immune Response. *Dev. Cell* **2019**, *49* (1), 100-117.e6. https://doi.org/10.1016/j.devcel.2019.03.010.

(63) Coburn, C.; Allman, E.; Mahanti, P.; Benedetto, A.; Cabreiro, F.; Pincus, Z.; Matthijssens, F.; Araiz, C.; Mandel, A.; Vlachos, M.; Edwards, S.-A.; Fischer, G.; Davidson, A.; Pryor, R. E.; Stevens, A.; Slack, F. J.; Tavernarakis, N.; Braeckman, B. P.; Schroeder, F. C.; Nehrke, K.; Gems, D. Anthranilate Fluorescence Marks a Calcium-Propagated Necrotic Wave That Promotes Organismal Death in C. Elegans. *PLoS Biol.* **2013**, *11* (7), e1001613. https://doi.org/10.1371/journal.pbio.1001613.

(64) Teuscher, A.; Ewald, C. Overcoming Autofluorescence to Assess GFP Expression During Normal Physiology and Aging in Caenorhabditis Elegans. *BIO-PROTOCOL* **2018**, *8* (14), e2940. https://doi.org/10.21769/BioProtoc.2940.

(65) He, X.; Wang, K.; Cheng, Z. In Vivo Near-Infrared Fluorescence Imaging of Cancer with Nanoparticle-Based Probes. *Wiley Interdiscip. Rev. Nanomedicine Nanobiotechnology* **2010**, *2* (4), 349–366. https://doi.org/10.1002/wnan.85.

(66) Hendler-Neumark, A.; Bisker, G. Fluorescent Single-Walled Carbon Nanotubes for Protein Detection. *Sensors* **2019**, *19* (24), 5403. https://doi.org/10.3390/s19245403.

(67) Huang, J.; Pu, K. Near-Infrared Fluorescent Molecular Probes for Imaging and

Diagnosis of Nephro-Urological Diseases. *Chem. Sci.* **2021**, *12* (10), 3379–3392. https://doi.org/10.1039/D0SC02925D.

(68) Chinnathambi, S.; Shirahata, N. Recent Advances on Fluorescent Biomarkers of Near-Infrared Quantum Dots for in Vitro and in Vivo Imaging. *Sci. Technol. Adv. Mater.* **2019**, *20* (1), 337–355. https://doi.org/10.1080/14686996.2019.1590731.

(69) Frangioni, J. V. In Vivo Near-Infrared Fluorescence Imaging. *Curr. Opin. Chem. Biol.* **2003**, *7* (5), 626–634. https://doi.org/10.1016/J.CBPA.2003.08.007.

(70) Owens, E. A.; Henary, M.; El Fakhri, G.; Choi, H. S. Tissue-Specific Near-Infrared Fluorescence Imaging. *Acc. Chem. Res.* **2016**, *49* (9), 1731–1740. https://doi.org/10.1021/acs.accounts.6b00239.

(71) O'Connell, M. J.; Bachilo, S. M.; Huffman, C. B.; Moore, V. C.; Strano, M. S.; Haroz, E. H.; Rialon, K. L.; Boul, P. J.; Noon, W. H.; Kittrell, C.; Ma, J.; Hauge, R. H.; Weisman, R. B.; Smalley, R. E. Band Gap Fluorescence from Individual Single-Walled Carbon Nanotubes. *Science* **2002**, *297* (5581), 593–596. https://doi.org/10.1126/science.1072631.

(72) Dresselhaus, M. S.; Dresselhaus, G.; Saito, R.; Jorio, A. Raman Spectroscopy of Carbon Nanotubes. *Phys. Rep.* **2005**, *409* (2), 47–99. https://doi.org/10.1016/j.physrep.2004.10.006.

(73) Bachilo, S. M.; Strano, M. S.; Kittrell, C.; Hauge, R. H.; Smalley, R. E.; Weisman, R. B. Structure-Assigned Optical Spectra of Single-Walled Carbon Nanotubes. *Science* **2002**, *298* (5602), 2361–2366. https://doi.org/10.1126/science.1078727.

(74) Nißler, R.; Bader, O.; Dohmen, M.; Walter, S. G.; Noll, C.; Selvaggio, G.; Groß, U.; Kruss, S. Remote near Infrared Identification of Pathogens with Multiplexed Nanosensors. *Nat. Commun.* **2020**, *11* (1), 5995. https://doi.org/10.1038/s41467-

020-19718-5.

(75) Nißler, R.; Kurth, L.; Li, H.; Spreinat, A.; Kuhlemann, I.; Flavel, B. S.; Kruss, S. Sensing with Chirality-Pure Near-Infrared Fluorescent Carbon Nanotubes. *Anal. Chem.* **2021**, *93* (16), 6446–6455. https://doi.org/10.1021/acs.analchem.1c00168.

(76) Yang, F.; Wang, M.; Zhang, D.; Yang, J.; Zheng, M.; Li, Y. Chirality Pure Carbon Nanotubes: Growth, Sorting, and Characterization. *Chem. Rev.* **2020**, *120* (5), 2693–2758. https://doi.org/10.1021/acs.chemrev.9b00835.

(77) Salem, D. P.; Landry, M. P.; Bisker, G.; Ahn, J.; Kruss, S.; Strano, M. S. Chirality Dependent Corona Phase Molecular Recognition of DNA-Wrapped Carbon Nanotubes. *Carbon N. Y.* **2016**, *97*, 147–153. https://doi.org/10.1016/j.carbon.2015.08.075.

(78) Antonucci, A.; Kupis-Rozmysłowicz, J.; Boghossian, A. A. Noncovalent Protein and Peptide Functionalization of Single-Walled Carbon Nanotubes for Biodelivery and Optical Sensing Applications. *ACS Appl. Mater. Interfaces* **2017**, *9* (13), 11321–11331. https://doi.org/10.1021/acsami.7b00810.

(79) Iverson, N. M.; Barone, P. W.; Shandell, M.; Trudel, L. J.; Sen, S.; Sen, F.; Ivanov, V.; Atolia, E.; Farias, E.; McNicholas, T. P.; Reuel, N.; Parry, N. M. A.; Wogan, G. N.; Strano, M. S. In Vivo Biosensing via Tissue-Localizable near-Infrared-Fluorescent Single-Walled Carbon Nanotubes. *Nat. Nanotechnol.* **2013**, *8* (11), 873–880. https://doi.org/10.1038/nnano.2013.222.

(80) Iverson, N. M.; Bisker, G.; Farias, E.; Ivanov, V.; Ahn, J.; Wogan, G. N.; Strano, M. S. Quantitative Tissue Spectroscopy of Near Infrared Fluorescent Nanosensor Implants HHS Public Access. *J Biomed Nanotechnol* **2016**, *12* (5), 1035–1047.

(81) Beyene, A. G.; Delevich, K.; Del Bonis-O'Donnell, J. T.; Piekarski, D. J.; Lin, W. C.; Wren Thomas, A.; Yang, S. J.; Kosillo, P.; Yang, D.; Prounis, G. S.;

Wilbrecht, L.; Landry, M. P. Imaging Striatal Dopamine Release Using a Nongenetically Encoded near Infrared Fluorescent Catecholamine Nanosensor. *Sci. Adv.* **2019**, *5* (7), 1–12. https://doi.org/10.1126/sciadv.aaw3108.

(82) Bonis-O'Donnell, J. T. Del; Page, R. H.; Beyene, A. G.; Tindall, E. G.; McFarlane, I. R.; Landry, M. P. Dual Near-Infrared Two-Photon Microscopy for Deep-Tissue Dopamine Nanosensor Imaging. *Adv. Funct. Mater.* **2017**, *27* (39), 1702112. https://doi.org/10.1002/adfm.201702112.

(83) Wu, H.; Nißler, R.; Morris, V.; Herrmann, N.; Hu, P.; Jeon, S. J.; Kruss, S.; Giraldo, J. P. Monitoring Plant Health with Near-Infrared Fluorescent H2O2 Nanosensors. *Nano Lett.* **2020**, *20* (4), 2432–2442. https://doi.org/10.1021/acs.nanolett.9b05159.

(84) Wong, M. H.; Giraldo, J. P.; Kwak, S.-Y.; Koman, V. B.; Sinclair, R.; Lew, T. T. S.; Bisker, G.; Liu, P.; Strano, M. S. Nitroaromatic Detection and Infrared Communication from Wild-Type Plants Using Plant Nanobionics. *Nat. Mater.* **2017**, *16* (2), 264–272. https://doi.org/10.1038/nmat4771.

(85) Robinson, J. T.; Hong, G.; Liang, Y.; Zhang, B.; Yaghi, O. K.; Dai, H. In Vivo Fluorescence Imaging in the Second Near-Infrared Window with Long Circulating Carbon Nanotubes Capable of Ultrahigh Tumor Uptake. *J. Am. Chem. Soc.* **2012**, *134* (25), 10664–10669. https://doi.org/10.1021/ja303737a.

(86) Bisker, G. Optical Nanosensors in the Near-Infrared Spectral Window. In *Conference on Lasers and Electro-Optics*; Optica Publishing Group: Washington, D.C., 2021; p AF2Q.6. https://doi.org/10.1364/CLEO_AT.2021.AF2Q.6.

(87) Qiu, L.; Ding, F. Understanding Single-Walled Carbon Nanotube Growth for Chirality Controllable Synthesis. *Accounts Mater. Res.* **2021**, *2* (9), 828–841. https://doi.org/10.1021/accountsmr.1c00111.

(88) Ackermann, J.; Metternich, J. T.; Herbertz, S.; Kruss, S. Biosensing with Fluorescent Carbon Nanotubes. *Angew. Chemie - Int. Ed.* **2022**, *61* (18). https://doi.org/10.1002/anie.202112372.

(89) Mu, B.; Zhang, J.; McNicholas, T. P.; Reuel, N. F.; Kruss, S.; Strano, M. S. Recent Advances in Molecular Recognition Based on Nanoengineered Platforms. *Acc. Chem. Res.* **2014**, *47* (4), 979–988. https://doi.org/10.1021/ar400162w.

(90) Wulf, V.; Slor, G.; Rathee, P.; Amir, R. J.; Bisker, G. Dendron–Polymer Hybrids as Tailorable Responsive Coronae of Single-Walled Carbon Nanotubes. *ACS Nano* **2021**, *15* (12), 20539–20549. https://doi.org/10.1021/acsnano.1c09125.

(91) Bisker, G.; Bakh, N. A.; Lee, M. A.; Ahn, J.; Park, M.; O'Connell, E. B.; Iverson, N. M.; Strano, M. S. Insulin Detection Using a Corona Phase Molecular Recognition Site on Single-Walled Carbon Nanotubes. *ACS Sensors* **2018**, *3* (2), 367–377. https://doi.org/10.1021/acssensors.7b00788.

(92) Bisker, G.; Dong, J.; Park, H. D.; Iverson, N. M.; Ahn, J.; Nelson, J. T.; Landry, M. P.; Kruss, S.; Strano, M. S. Protein-Targeted Corona Phase Molecular Recognition. *Nat. Commun.* **2016**, *7* (1), 10241. https://doi.org/10.1038/ncomms10241.

(93) Nelson, J. T.; Kim, S.; Reuel, N. F.; Salem, D. P.; Bisker, G.; Landry, M. P.; Kruss, S.; Barone, P. W.; Kwak, S.; Strano, M. S. Mechanism of Immobilized Protein A Binding to Immunoglobulin G on Nanosensor Array Surfaces. *Anal. Chem* **2015**, *87*, 45. https://doi.org/10.1021/acs.analchem.5b00843.

(94) Oh, S.-H.; Altug, H.; Jin, X.; Low, T.; Koester, S. J.; Ivanov, A. P.; Edel, J. B.; Avouris, P.; Strano, M. S. Nanophotonic Biosensors Harnessing van Der Waals Materials. *Nat. Commun.* **2021**, *12* (1), 3824. https://doi.org/10.1038/s41467-021-23564-4.

(95) Ehrlich, R.; Hendler-Neumark, A.; Wulf, V.; Amir, D.; Bisker, G. Optical Nanosensors for Real-Time Feedback on Insulin Secretion by B-Cells. *Small* **2021**, *17* (30), 2101660. https://doi.org/10.1002/smll.202101660.

(96) Graf, A.; Zakharko, Y.; Schießl, S. P.; Backes, C.; Pfohl, M.; Flavel, B. S.; Zaumseil, J. Large Scale, Selective Dispersion of Long Single-Walled Carbon Nanotubes with High Photoluminescence Quantum Yield by Shear Force Mixing. *Carbon N. Y.* **2016**, *105*, 593–599. https://doi.org/10.1016/j.carbon.2016.05.002.

(97) Hashida, Y.; Tanaka, H.; Zhou, S.; Kawakami, S.; Yamashita, F.; Murakami, T.; Umeyama, T.; Imahori, H.; Hashida, M. Photothermal Ablation of Tumor Cells Using a Single-Walled Carbon Nanotube-Peptide Composite. *J. Control. Release* **2014**, *173* (1), 59–66. https://doi.org/10.1016/j.jconrel.2013.10.039.

(98) Panchapakesan, B.; Cesarone, G.; Liu, S.; Teker, K.; Wickstrom, E. Single-Wall Carbon Nanotubes with Adsorbed Antibodies Detect Live Breast Cancer Cells. *Nanobiotechnology* **2005**, *1* (4), 353–360. https://doi.org/10.1385/NBT:1:4:353.

(99) Chen, H.; Yu, C.; Jiang, C.; Zhang, S.; Liu, B.; Kong, J. A Novel Near-Infrared Protein Assay Based on the Dissolution and Aggregation of Aptamer-Wrapped Single-Walled Carbon Nanotubes. *Chem. Commun.* **2009**, No. 33, 5006. https://doi.org/10.1039/b910457g.

(100) Landry, M. P.; Vuković,Vuković, L.; Kruss, S.; Bisker, G.; Landry, A. M.; Islam, S.; Jain, R.; Schulten, K.; Strano, M. S. Comparative Dynamics and Sequence Dependence of DNA and RNA Binding to Single Walled Carbon Nanotubes. *J. Phys. Chem. C* **2015**, *119*, 24. https://doi.org/10.1021/jp511448e.

(101) Shumeiko, V.; Malach, E.; Helman, Y.; Paltiel, Y.; Bisker, G.; Hayouka, Z.; Shoseyov, O. Sensors and Actuators : B . Chemical A Nanoscale Optical Biosensor Based on Peptide Encapsulated SWCNTs for Detection of Acetic Acid

in the Gaseous Phase. *Sensors Actuators B. Chem.* **2021**, *327* (September 2020), 128832. https://doi.org/10.1016/j.snb.2020.128832.

(102) Zubkovs, V.; Wu, S.-J.; Rahnamaee, S. Y.; Schuergers, N.; Boghossian, A. A. Site-Specific Protein Conjugation onto Fluorescent Single-Walled Carbon Nanotubes. *Chem. Mater.* **2020**, *32* (20), 8798–8807. https://doi.org/10.1021/acs.chemmater.0c02051.

(103) Chio, L.; Del Bonis-O'Donnell, J. T.; Kline, M. A.; Kim, J. H.; McFarlane, I. R.; Zuckermann, R. N.; Landry, M. P. Electrostatic Assemblies of Single-Walled Carbon Nanotubes and Sequence-Tunable Peptoid Polymers Detect a Lectin Protein and Its Target Sugars. *Nano Lett.* **2019**, *19* (11), 7563–7572. https://doi.org/10.1021/acs.nanolett.8b04955.

(104) Zou, J.; Zhang, Q. Advances and Frontiers in Single-Walled Carbon Nanotube Electronics. *Adv. Sci.* **2021**, *8* (23), 1–19. https://doi.org/10.1002/advs.202102860.

(105) Gu, Q.; Gicquel-Guézo, M.; Loualiche, S.; Pouliquen, J. Le; Batte, T.; Folliot, H.; Dehaese, O.; Grillot, F.; Battie, Y.; Loiseau, A.; Liang, B.; Huffaker, D. Photonics Based on Carbon Nanotubes. *Nanoscale Res. Lett.* **2013**, *8* (1), 300. https://doi.org/10.1186/1556-276X-8-300.

(106) Chen, X.; Cheng, P.; Tang, Z.; Xu, X.; Gao, H.; Wang, G. Carbon-Based Composite Phase Change Materials for Thermal Energy Storage, Transfer, and Conversion. *Adv. Sci.* **2021**, *8* (9), 1–38. https://doi.org/10.1002/advs.202001274.

(107) Kuo, M.-T.; Raffaelle, J. F.; Waller, E. M.; Varaljay, V. A.; Wagner, D.; Kelley-Loughnane, N.; Reuel, N. F. Screening Enzymatic Degradation of Polyester Polyurethane with Fluorescent Single-Walled Carbon Nanotube and Polymer Nanoparticle Conjugates. *ACS Nano* **2023**, *17* (17), 17021–17030.

https://doi.org/10.1021/acsnano.3c04347.

(108) Demirer, G.; Landry, M. Efficient Transient Gene Knock-down in Tobacco Plants Using Carbon Nanocarriers. *BIO-PROTOCOL* **2021**, *11* (1), 1–13. https://doi.org/10.21769/BioProtoc.3897.

(109) Kwak, S.-Y.; Lew, T. T. S.; Sweeney, C. J.; Koman, V. B.; Wong, M. H.; Bohmert-Tatarev, K.; Snell, K. D.; Seo, J. S.; Chua, N.-H.; Strano, M. S. Chloroplast-Selective Gene Delivery and Expression in Planta Using Chitosan-Complexed Single-Walled Carbon Nanotube Carriers. *Nat. Nanotechnol.* **2019**, *14* (5), 447–455. https://doi.org/10.1038/s41565-019-0375-4.

(110) Godin, A. G.; Varela, J. A.; Gao, Z.; Danné, N.; Dupuis, J. P.; Lounis, B.; Groc, L.; Cognet, L. Single-Nanotube Tracking Reveals the Nanoscale Organization of the Extracellular Space in the Live Brain. *Nat. Nanotechnol.* **2017**, *12* (3), 238–243. https://doi.org/10.1038/nnano.2016.248.

(111) Mandal, A. K.; Wu, X.; Ferreira, J. S.; Kim, M.; Powell, L. R.; Kwon, H.; Groc, L.; Wang, Y.; Cognet, L. Fluorescent Sp3 Defect-Tailored Carbon Nanotubes Enable NIR-II Single Particle Imaging in Live Brain Slices at Ultra-Low Excitation Doses. *Sci. Rep.* **2020**, *10* (1), 5286. https://doi.org/10.1038/s41598-020-62201-w.

(112) Agarwal, S.; Kallmyer, N. E.; Vang, D. X.; Ramirez, A. V.; Islam, M. M.; Hillier, A. C.; Halverson, L. J.; Reuel, N. F. Single-Walled Carbon Nanotube Probes for the Characterization of Biofilm-Degrading Enzymes Demonstrated against Pseudomonas Aeruginosa Extracellular Matrices. *Anal. Chem.* **2022**, *94* (2), 856–865. https://doi.org/10.1021/acs.analchem.1c03633.

(113) Harvey, J. D.; Baker, H. A.; Ortiz, M. V.; Kentsis, A.; Heller, D. A. HIV Detection via a Carbon Nanotube RNA Sensor. *ACS Sensors* **2019**, *4* (5), 1236–

1244. https://doi.org/10.1021/acssensors.9b00025.

(114) Madani, S. Z. M.; Safaee, M. M.; Gravely, M.; Silva, C.; Kennedy, S.; Bothun, G. D.; Roxbury, D. Carbon Nanotube–Liposome Complexes in Hydrogels for Controlled Drug Delivery via Near-Infrared Laser Stimulation. *ACS Appl. Nano Mater.* **2021**, *4* (1), 331–342. https://doi.org/10.1021/acsanm.0c02700.

(115) Hendler-Neumark, A.; Wulf, V.; Bisker, G. Single-Walled Carbon Nanotube Sensor Selection for the Detection of MicroRNA Biomarkers for Acute Myocardial Infarction as a Case Study. *ACS Sensors* **2023**, *8* (10), 3713–3722. https://doi.org/10.1021/acssensors.3c00633.

(116) Niidome, Y.; Hamano, R.; Nakamura, K.; Qi, S.; Ito, S.; Yu, B.; Nagai, Y.; Tanaka, N.; Mori, T.; Katayama, Y.; Fujigaya, T.; Shiraki, T. Near-Infrared Photoluminescent Detection of Serum Albumin Using Single-Walled Carbon Nanotubes Locally Functionalized with a Long-Chain Fatty Acid. *Carbon N. Y.* **2023**, 118533. https://doi.org/10.1016/j.carbon.2023.118533.

(117) Côa, F.; Bortolozzo, L. de S.; Ávila, D. S.; Souza Filho, A. G.; Martinez, D. S. T. Toxicology of Carbon Nanomaterials in the Caenorhabditis Elegans Model: Current Status, Characterization, and Perspectives for Testing Harmonization. *Front. Carbon* **2023**, *2*, 1241637. https://doi.org/10.3389/frcrb.2023.1241637.

(118) Harvey, J. D.; Jena, P. V; Baker, H. A.; Zerze, G. H.; Williams, R. M.; Galassi, T. V; Roxbury, D.; Mittal, J.; Heller, D. A. A Carbon Nanotube Reporter of MicroRNA Hybridization Events in Vivo. *Nat. Biomed. Eng.* **2017**, *1* (4), 0041. https://doi.org/10.1038/s41551-017-0041.

(119) Ang, M. C.-Y.; Dhar, N.; Khong, D. T.; Lew, T. T. S.; Park, M.; Sarangapani, S.; Cui, J.; Dehadrai, A.; Singh, G. P.; Chan-Park, M. B.; Sarojam, R.; Strano, M. Nanosensor Detection of Synthetic Auxins In Planta Using Corona Phase

Molecular Recognition. *ACS Sensors* **2021**, *6* (8), 3032–3046. https://doi.org/10.1021/acssensors.1c01022.

(120) Shumeiko, V.; Paltiel, Y.; Bisker, G.; Hayouka, Z.; Shoseyov, O. A Paper-Based Near-Infrared Optical Biosensor for Quantitative Detection of Protease Activity Using Peptide-Encapsulated SWCNTs. *Sensors* **2020**, *20* (18), 5247. https://doi.org/10.3390/s20185247.

(121) Hofferber, E.; Meier, J.; Herrera, N.; Stapleton, J.; Calkins, C.; Iverson, N. Detection of Single Walled Carbon Nanotube Based Sensors in a Large Mammal. *Nanomedicine Nanotechnology, Biol. Med.* **2022**, *40*, 102489. https://doi.org/10.1016/j.nano.2021.102489.

(122) Amir, D.; Hendler-Neumark, A.; Wulf, V.; Ehrlich, R.; Bisker, G. Oncometabolite Fingerprinting Using Fluorescent Single-Walled Carbon Nanotubes. *Adv. Mater. Interfaces* **2022**, *9* (4), 2101591. https://doi.org/10.1002/admi.202101591.

(123) Lew, T. T. S.; Park, M.; Cui, J.; Strano, M. S. Plant Nanobionic Sensors for Arsenic Detection. *Adv. Mater.* **2021**, *33* (1), 2005683. https://doi.org/10.1002/adma.202005683.

(124) Galassi, T. V.; Antman-Passig, M.; Yaari, Z.; Jessurun, J.; Schwartz, R. E.; Heller, D. A. Long-Term in Vivo Biocompatibility of Single-Walled Carbon Nanotubes. *PLoS One* **2020**, *15* (5), 1–22. https://doi.org/10.1371/journal.pone.0226791.

(125) Roxbury, D.; Jena, P. V; Williams, R. M.; Enyedi, B.; Niethammer, P.; Marcet, S.; Verhaegen, M.; Blais-ouellette, S. Hyperspectral Microscopy of Near- Infrared Fluorescence Enables 17-Chirality Carbon Nanotube Imaging. *Nat. Publ. Gr.* **2015**, No. September, 1–6. https://doi.org/10.1038/srep14167.

(126) Pan, J.; Li, F.; Choi, J. H. Single-Walled Carbon Nanotubes as Optical Probes for Bio-Sensing and Imaging. *J. Mater. Chem. B* **2017**, *5*, 6511. https://doi.org/10.1039/c7tb00748e.

(127) Barone, P. W.; Parker, R. S.; Strano, M. S. In Vivo Fluorescence Detection of Glucose Using a Single-Walled Carbon Nanotube Optical Sensor: Design, Fluorophore Properties, Advantages, and Disadvantages. *Anal. Chem.* **2005**, *77* (23), 7556–7562. https://doi.org/10.1021/ac0511997.

(128) Lee, M. A.; Wang, S.; Jin, X.; Bakh, N. A.; Nguyen, F. T.; Dong, J.; Silmore, K. S.; Gong, X.; Pham, C.; Jones, K. K.; Muthupalani, S.; Bisker, G.; Son, M.; Strano, M. S. Implantable Nanosensors for Human Steroid Hormone Sensing In Vivo Using a Self-Templating Corona Phase Molecular Recognition. *Adv. Healthc. Mater.* **2020**, *9* (21), 2000429. https://doi.org/10.1002/adhm.202000429.

(129) Boghossian, A. A.; Zhang, J.; Barone, P. W.; Reuel, N. F.; Kim, J.-H.; Heller, D. A.; Ahn, J.-H.; Hilmer, A. J.; Rwei, A.; Arkalgud, J. R.; Zhang, C. T.; Strano, M. S. Near-Infrared Fluorescent Sensors Based on Single-Walled Carbon Nanotubes for Life Sciences Applications. *ChemSusChem* **2011**, *4* (7), 848–863. https://doi.org/10.1002/cssc.201100070.

(130) Kruss, S.; Hilmer, A. J.; Zhang, J.; Reuel, N. F.; Mu, B.; Strano, M. S. Carbon Nanotubes as Optical Biomedical Sensors ☆. *Adv. Drug Deliv. Rev.* **2013**, *65* (15), 1933–1950. https://doi.org/10.1016/j.addr.2013.07.015.

(131) Hofferber, E. M.; Stapleton, J. A.; Iverson, N. M. Review—Single Walled Carbon Nanotubes as Optical Sensors for Biological Applications. *J. Electrochem. Soc.* **2020**, *167* (3), 037530. https://doi.org/10.1149/1945-7111/ab64bf.

(132) Antonucci, A.; Reggente, M.; Roullier, C.; Gillen, A. J.; Schuergers, N.; Zubkovs, V.; Lambert, B. P.; Mouhib, M.; Carata, E.; Dini, L.; Boghossian, A. A. Carbon

Nanotube Uptake in Cyanobacteria for Near-Infrared Imaging and Enhanced Bioelectricity Generation in Living Photovoltaics. *Nat. Nanotechnol. 2022 1710* **2022**, *17* (10), 1111–1119. https://doi.org/10.1038/s41565-022-01198-x.

(133) Fang, H.; Yao, S.; Chen, Q.; Liu, C.; Cai, Y.; Geng, S.; Bai, Y.; Tian, Z.; Zacharias, A. L.; Takebe, T.; Chen, Y.; Guo, Z.; He, W.; Diao, J. De Novo - Designed Near-Infrared Nanoaggregates for Super-Resolution Monitoring of Lysosomes in Cells, in Whole Organoids, and in Vivo. *ACS Nano* **2019**, *13* (12), 14426–14436. https://doi.org/10.1021/acsnano.9b08011.

(134) Huang, X.; Fan, J.; Li, L.; Liu, H.; Wu, R.; Wu, Y.; Wei, L.; Mao, H.; Lal, A.; Xi, P.; Tang, L.; Zhang, Y.; Liu, Y.; Tan, S.; Chen, L. Fast, Long-Term, Super-Resolution Imaging with Hessian Structured Illumination Microscopy. *Nat. Biotechnol.* **2018**, *36* (5), 451–459. https://doi.org/10.1038/nbt.4115.

(135) Li, H.; Feng, F.; Zhai, M.; Zhang, J.; Jiang, J.; Su, Y.; Chen, L.; Gao, S.; Tao, L.; Mao, H. Fast Whole-body Motor Neuron Calcium Imaging of Freely Moving <scp> *Caenorhabditis Elegans* </Scp> without Coverslip Pressed. *Cytom. Part A* **2021**, *99* (11), 1143–1157. https://doi.org/10.1002/cyto.a.24483.

(136) Barman, A. K.; Chaturbedi, A.; Subramaniam, K.; Verma, S. Imaging C. Elegans with Thiolated Tryptophan-Based NIR Fluorescent Gold Nanoclusters. *J. Nanoparticle Res.* **2013**, *15* (11), 2083. https://doi.org/10.1007/s11051-013-2083-6.

(137) Zhang, J.; Landry, M. P.; Barone, P. W.; Kim, J. H.; Lin, S.; Ulissi, Z. W.; Lin, D.; Mu, B.; Boghossian, A. A.; Hilmer, A. J.; Rwei, A.; Hinckley, A. C.; Kruss, S.; Shandell, M. A.; Nair, N.; Blake, S.; Şen, F.; Şen, S.; Croy, R. G.; Li, D.; Yum, K.; Ahn, J. H.; Jin, H.; Heller, D. A.; Essigmann, J. M.; Blankschtein, D.; Strano, M. S. Molecular Recognition Using Corona Phase Complexes Made of

Synthetic Polymers Adsorbed on Carbon Nanotubes. *Nat. Nanotechnol.* **2013**, *8* (12), 959–968. https://doi.org/10.1038/nnano.2013.236.

(138) Fang-Yen, C.; Gabel, C. V.; Samuel, A. D. T.; Bargmann, C. I.; Avery, L. Laser Microsurgery in Caenorhabditis Elegans. In *Methods in Cell Biology*; 2012; Vol. 107, pp 177–206. https://doi.org/10.1016/B978-0-12-394620-1.00006-0.

(139) Lewis, J. A.; Wu, C. H.; Berg, H.; Levine, J. H. The Genetics of Levamisole Resistance in the Nematode Caenorhabditis Elegans. *Genetics* **1980**, *95* (4), 905–928. https://doi.org/10.1093/genetics/95.4.905.

(140) Cornaglia, M.; Mouchiroud, L.; Marette, A.; Narasimhan, S.; Lehnert, T.; Jovaisaite, V.; Auwerx, J.; Gijs, M. A. M. An Automated Microfluidic Platform for C. Elegans Embryo Arraying, Phenotyping, and Long-Term Live Imaging. *Sci. Rep.* **2015**, *5* (May), 1–13. https://doi.org/10.1038/srep10192.

(141) Gritti, N.; Kienle, S.; Filina, O.; Van Zon, J. S. Long-Term Time-Lapse Microscopy of C. Elegans Post-Embryonic Development. *Nat. Commun.* **2016**, *7*, 1–9. https://doi.org/10.1038/ncomms12500.

(142) Mondal, S.; Ben-Yakar, A. Caenorhabditis Elegans-on-a-Chip: Microfluidic Platforms for High-Resolution Imaging and Phenotyping. In *Organ-on-a-chip*; Elsevier, 2020; pp 363–390. https://doi.org/10.1016/B978-0-12-817202-5.00009-7.

(143) Guo, S. X.; Bourgeois, F.; Chokshi, T.; Durr, N. J.; Hilliard, M. A.; Chronis, N.; Ben-Yakar, A. Femtosecond Laser Nanoaxotomy Lab-on-a-Chip for in Vivo Nerve Regeneration Studies. *Nat. Methods* **2008**, *5* (6), 531–533. https://doi.org/10.1038/nmeth.1203.

(144) Krajniak, J.; Lu, H. Long-Term High-Resolution Imaging and Culture of C. Elegans in Chip-Gel Hybrid Microfluidic Device for Developmental Studies. *Lab*

Chip **2010**, *10* (14), 1862–1868. https://doi.org/10.1039/c001986k.

(145) Carr, J. A.; Parashar, A.; Gibson, R.; Robertson, A. P.; Martin, R. J.; Pandey, S. A Microfluidic Platform for High-Sensitivity, Real-Time Drug Screening on C. Elegans and Parasitic Nematodes. *Lab Chip* **2011**, *11* (14), 2385. https://doi.org/10.1039/c1lc20170k.

(146) Viri, V.; Arveiler, M.; Lehnert, T.; Gijs, M. A. M. An in Vivo Microfluidic Study of Bacterial Load Dynamics and Absorption in the C. Elegans Intestine. *Micromachines* **2021**, *12* (7), 832. https://doi.org/10.3390/MI12070832/S1.

(147) Youssef, K.; Archonta, D.; Kubiseski, T. J.; Tandon, A.; Rezai, P. Microfluidic Electric Parallel Egg-Laying Assay and Application to in-Vivo Toxicity Screening of Microplastics Using C. Elegans. *Sci. Total Environ.* **2021**, *783*, 147055. https://doi.org/10.1016/j.scitotenv.2021.147055.

(148) Song, P.; Zhang, W.; Sobolevski, A.; Bernard, K.; Hekimi, S.; Liu, X. A Microfluidic Device for Efficient Chemical Testing Using Caenorhabditis Elegans. *Biomed. Microdevices* **2015**, *17* (2), 1–10. https://doi.org/10.1007/s10544-015-9939-8.

(149) Levine, E.; Lee, K. S. Microfluidic Approaches for Caenorhabditis Elegans Research. *Animal Cells Syst. (Seoul).* **2020**, *24* (6), 311–320. https://doi.org/10.1080/19768354.2020.1837951.

(150) Ghorashian, N.; Gökçe, S. K.; Ben-Yakar, A. Microfluidic Systems for Whole-Animal Screening with C. Elegans. In *Micro- and Nanosystems for Biotechnology*; Wiley-VCH Verlag GmbH & Co. KGaA: Weinheim, Germany, 2016; pp 245–272. https://doi.org/10.1002/9783527801312.ch10.

(151) Shivers, J.; Uppaluri, S.; Brangwynne, C. P. Microfluidic Immobilization and Subcellular Imaging of Developing Caenorhabditis Elegans. *Microfluid.*

Nanofluidics **2017**, *21* (9), 1–9. https://doi.org/10.1007/s10404-017-1988-2.

(152) Mondal, S.; Hegarty, E.; Martin, C.; Gökçe, S. K.; Ghorashian, N.; Ben-Yakar, A. Large-Scale Microfluidics Providing High-Resolution and High-Throughput Screening of Caenorhabditis Elegans Poly-Glutamine Aggregation Model. *Nat. Commun.* **2016**, *7* (1), 13023. https://doi.org/10.1038/ncomms13023.

(153) Keil, W.; Kutscher, L. M.; Shaham, S.; Siggia, E. D. Long-Term High-Resolution Imaging of Developing C. Elegans Larvae with Microfluidics. *Dev. Cell* **2017**, *40* (2), 202–214. https://doi.org/10.1016/j.devcel.2016.11.022.

(154) Rezai, P.; Salam, S.; Selvaganapathy, P. R.; Gupta, B. P. Electrical Sorting of Caenorhabditis Elegans. *Lab Chip* **2012**, *12* (10), 1831–1840. https://doi.org/10.1039/C2LC20967E.

(155) Lockery, S. R.; Hulme, S. E.; Roberts, W. M.; Robinson, K. J.; Laromaine, A.; Lindsay, T. H.; Whitesides, G. M.; Weeks, J. C. A Microfluidic Device for Whole-Animal Drug Screening Using Electrophysiological Measures in the Nematode C. Elegans. *Lab Chip* **2012**, *12* (12), 2211. https://doi.org/10.1039/c2lc00001f.

(156) Cho, Y.; Porto, D. A.; Hwang, H.; Grundy, L. J.; Schafer, W. R.; Lu, H. Automated and Controlled Mechanical Stimulation and Functional Imaging in Vivo in C. Elegans. *Lab Chip* **2017**, *17* (15), 2609–2618. https://doi.org/10.1039/c7lc00465f.

(157) Ahmed, D.; Ozcelik, A.; Bojanala, N.; Nama, N.; Upadhyay, A.; Chen, Y.; Hanna-Rose, W.; Huang, T. J. Rotational Manipulation of Single Cells and Organisms Using Acoustic Waves. *Nat. Commun.* **2016**, *7* (1), 11085. https://doi.org/10.1038/ncomms11085.

(158) Kopito, R. B.; Levine, E. Durable Spatiotemporal Surveillance of Caenorhabditis

Elegans Response to Environmental Cues-SI. *Lab Chip* **2014**, *14* (4), 764–770. https://doi.org/10.1039/c3lc51061a.

(159) Lee, K. S.; Levine, E. A Microfluidic Platform for Longitudinal Imaging in Caenorhabditis Elegans. *J. Vis. Exp.* **2018**, *2018* (135), 1–7. https://doi.org/10.3791/57348.

(160) Scholz, M.; Lynch, D. J.; Suk, K.; Levine, E.; Biron, D. A Scalable Method for Automatically Measuring Pharyngeal Pumping in C . Elegans. *J. Neurosci. Methods* **2016**, *274*, 172–178. https://doi.org/10.1016/j.jneumeth.2016.07.016.

(161) Lee, K. S.; Iwanir, S.; Kopito, R. B.; Scholz, M.; Calarco, J. A.; Biron, D.; Levine, E. Serotonin-Dependent Kinetics of Feeding Bursts Underlie a Graded Response to Food Availability in C. Elegans. *Nat. Commun.* **2017**, *8* (1), 14221. https://doi.org/10.1038/ncomms14221.

(162) Sharaga, E.; Hendler-Neumark, A.; Kamber, D.; Bisker, G. Spatiotemporal Tracking of Near-Infrared Fluorescent Single-Walled Carbon Nanotubes in C. Elegans Nematodes Confined in a Microfluidics Platform. *Adv. Mater. Technol.* **2023**.

(163) Welsher, K.; Liu, Z.; Sherlock, S. P.; Robinson, J. T.; Chen, Z.; Daranciang, D.; Dai, H. A Route to Brightly Fluorescent Carbon Nanotubes for Near-Infrared Imaging in Mice. *Nat. Nanotechnol. 2009 411* **2009**, *4* (11), 773–780. https://doi.org/10.1038/nnano.2009.294.

(164) Stiernagle, T. *Maintenance of C. Elegans*; 2006. https://doi.org/10.1895/wormbook.1.101.1.

(165) Brenner, S. The Genetics of Caenorhabditis Elegans. Genetics. 1974 May;77(1):71-94. In *The genetics of Caenorhabditis elegans. Genetics.*; 1974; pp 71–94.

(166) Donkin, S. G.; Williams, P. L. Influence of Developmental Stage, Salts and Food Presence on Various End Points Using Caenorhabditis Elegans for Aquatic Toxicity Testing. *Environ. Toxicol. Chem.* **1995**, *14* (12), 2139–2147. https://doi.org/10.1002/etc.5620141218.

(167) Kopito, R. B.; Levine, E. Durable Spatiotemporal Surveillance of Caenorhabditis Elegans Response to Environmental Cues. *Lab Chip* **2014**, *14* (4), 764–770. https://doi.org/10.1039/c3lc51061a.

(168) Xia, Y.; Whitesides, G. M. Soft Lithography. *Annu. Rev. Mater. Sci.* **1998**, *28* (1), 153–184. https://doi.org/10.1146/annurev.matsci.28.1.153.

(169) Gokce, S. K.; Hegarty, E. M.; Mondal, S.; Zhao, P.; Ghorashian, N.; Hilliard, M. A.; Ben-Yakar, A. A Multi-Trap Microfluidic Chip Enabling Longitudinal Studies of Nerve Regeneration in Caenorhabditis Elegans. *Sci. Rep.* **2017**, *7* (1), 1–12. https://doi.org/10.1038/s41598-017-10302-4.

(170) Wu, Z.; Hjort, K. Surface Modification of PDMS by Gradient-Induced Migration of Embedded Pluronic. *Lab Chip* **2009**, *9* (11), 1500–1503. https://doi.org/10.1039/B901651A.

(171) González-Grandío, E.; Demirer, G. S.; Jackson, C. T.; Yang, D.; Ebert, S.; Molawi, K.; Keller, H.; Landry, M. P. Carbon Nanotube Biocompatibility in Plants Is Determined by Their Surface Chemistry. *J. Nanobiotechnology* **2021**, *19* (1), 431. https://doi.org/10.1186/s12951-021-01178-8.

(172) Jokerst, J. V.; Lobovkina, T.; Zare, R. N.; Gambhir, S. S. Nanoparticle PEGylation for Imaging and Therapy. *Nanomedicine (Lond).* **2011**, *6* (4), 715. https://doi.org/10.2217/NNM.11.19.

(173) Suk, J. S.; Xu, Q.; Kim, N.; Hanes, J.; Ensign, L. M. PEGylation as a Strategy for Improving Nanoparticle-Based Drug and Gene Delivery. *Adv. Drug Deliv. Rev.*

2016, *99* (Pt A), 28–51. https://doi.org/10.1016/j.addr.2015.09.012.

(174) Wang, M.; Gustafsson, O. J. R.; Siddiqui, G.; Javed, I.; Kelly, H. G.; Blin, T.; Yin, H.; Kent, S. J.; Creek, D. J.; Kempe, K.; Ke, P. C.; Davis, T. P. Human Plasma Proteome Association and Cytotoxicity of Nano-Graphene Oxide Grafted with Stealth Polyethylene Glycol and Poly(2-Ethyl-2-Oxazoline). *Nanoscale* **2018**, *10* (23), 10863–10875. https://doi.org/10.1039/c8nr00835c.

(175) Hadidi, N.; Farshad, S.; Shirazi, H.; Kobarfard, F.; Nafissi-Varcheh, N.; Aboofazeli, R. Evaluation of the Effect of PEGylated Single-Walled Carbon Nanotubes on Viability and Proliferation of Jurkat Cells. *Shaheed Beheshti Univ. Med. Sci. Heal. Serv. Iran. J. Pharm. Res.* **2012**, *11* (1), 27–37.

(176) Heller, D. A.; Baik, S.; Eurell, T. E.; Strano, M. S. Single-Walled Carbon Nanotube Spectroscopy in Live Cells: Towards Long-Term Labels and Optical Sensors. *Adv. Mater.* **2005**, *17* (23), 2793–2799. https://doi.org/10.1002/adma.200500477.

(177) Campagnolo, L.; Massimiani, M.; Palmieri, G.; Bernardini, R.; Sacchetti, C.; Bergamaschi, A.; Vecchione, L.; Magrini, A.; Bottini, M.; Pietroiusti, A. Biodistribution and Toxicity of Pegylated Single Wall Carbon Nanotubes in Pregnant Mice. *Part. Fibre Toxicol.* **2013**, *10* (1), 21. https://doi.org/10.1186/1743-8977-10-21.

(178) Iverson, N. M.; Barone, P. W.; Shandell, M.; Trudel, L. J.; Sen, S.; Sen, F.; Ivanov, V.; Atolia, E.; Farias, E.; McNicholas, T. P.; Reuel, N.; Parry, N. M. A.; Wogan, G. N.; Strano, M. S. In Vivo Biosensing via Tissue-Localizable near-Infrared-Fluorescent Single-Walled Carbon Nanotubes. *Nat. Nanotechnol.* **2013**, *8* (11), 873–880. https://doi.org/10.1038/nnano.2013.222.

(179) Gerstman, E.; Hendler-Neumark, A.; Wulf, V.; Bisker, G. Monitoring the

Formation of Fibrin Clots as Part of the Coagulation Cascade Using Fluorescent Single-Walled Carbon Nanotubes. *ACS Appl. Mater. Interfaces* **2023**, *15* (18), 21866–21876. https://doi.org/10.1021/acsami.3c00828.

(180) Ward, A.; Liu, J.; Feng, Z.; Xu, X. Z. S. Light-Sensitive Neurons and Channels Mediate Phototaxis in C. Elegans. *Nat. Neurosci.* **2008**, *11* (8), 916–922. https://doi.org/10.1038/nn.2155.

(181) De Magalhaes Filho, C. D.; Henriquez, B.; Seah, N. E.; Evans, R. M.; Lapierre, L. R.; Dillin, A. Visible Light Reduces C. Elegans Longevity. *Nat. Commun.* **2018**, *9* (1), 927. https://doi.org/10.1038/s41467-018-02934-5.

(182) Hermann, G. J.; Leung, B.; Priess, J. R. Left-Right Asymmetry in C. Elegans Intestine Organogenesis Involves a LIN-12/Notch Signaling Pathway. *Development* **2000**, *127* (16), 3429–3440. https://doi.org/10.1242/dev.127.16.3429.

(183) Palikaras, K.; Tavernarakis, N. Caenorhabditis Elegans (Nematode). In *Brenner's Encyclopedia of Genetics*; Elsevier, 2013; Vol. 1, pp 404–408. https://doi.org/10.1016/B978-0-12-374984-0.00186-8.

(184) Koopman, M.; Peter, Q.; Seinstra, R. I.; Perni, M.; Vendruscolo, M.; Dobson, C. M.; Knowles, T. P. J.; Nollen, E. A. A. Assessing Motor-Related Phenotypes of Caenorhabditis Elegans with the Wide Field-of-View Nematode Tracking Platform. *Nat. Protoc.* **2020**, *15* (6), 2071–2106. https://doi.org/10.1038/s41596-020-0321-9.

(185) Itskovits, E.; Ruach, R.; Kazakov, A.; Zaslaver, A. Concerted Pulsatile and Graded Neural Dynamics Enables Efficient Chemotaxis in C. Elegans. *Nat. Commun.* **2018**, *9* (1), 2866. https://doi.org/10.1038/s41467-018-05151-2.

(186) Perni, M.; Challa, P. K.; Kirkegaard, J. B.; Limbocker, R.; Koopman, M.;

Hardenberg, M. C.; Sormanni, P.; Müller, T.; Saar, K. L.; Roode, L. W. Y.; Habchi, J.; Vecchi, G.; Fernando, N.; Casford, S.; Nollen, E. A. A.; Vendruscolo, M.; Dobson, C. M.; Knowles, T. P. J. Massively Parallel C. Elegans Tracking Provides Multi-Dimensional Fingerprints for Phenotypic Discovery. *J. Neurosci. Methods* **2018**, *306*, 57–67. https://doi.org/10.1016/j.jneumeth.2018.02.005.

(187) Smith, M. P.; Laws, T. R.; Atkins, T. P.; Oyston, P. C. F.; Pomerai, D. I.; Titball, R. W. A Liquid-Based Method for the Assessment of Bacterial Pathogenicity Using the Nematode Caenorhabditis Elegans. *FEMS Microbiol. Lett.* **2002**, *210* (2), 181–185. https://doi.org/10.1111/j.1574-6968.2002.tb11178.x.

(188) Hull, D.; Timmons, L. Methods for Delivery of Double-Stranded RNA into Caenorhabditis Elegans. *Methods Mol. Biol.* **2004**, *265*, 23–58. https://doi.org/10.1385/1-59259-775-0:023.

(189) Pees, B.; Yang, W.; Kloock, A.; Petersen, C.; Peters, L.; Fan, L.; Friedrichsen, M.; Butze, S.; Zárate-Potes, A.; Schulenburg, H.; Dierking, K. Effector and Regulator: Diverse Functions of C. Elegans C-Type Lectin-like Domain Proteins. *PLoS Pathog.* **2021**, *17* (4), 1–25. https://doi.org/10.1371/JOURNAL.PPAT.1009454.

(190) Berninsone, P. *Carbohydrates and Glycosylation*; WormBook Research Community, 2006; Vol. 17. https://doi.org/10.1895/wormbook.1.125.1.

(191) Pinals, R. L.; Yang, D.; Rosenberg, D. J.; Chaudhary, T.; Crothers, A. R.; Iavarone, A. T.; Hammel, M.; Landry, M. P. Quantitative Protein Corona Composition and Dynamics on Carbon Nanotubes in Biological Environments. *Angew. Chemie - Int. Ed.* **2020**, *59* (52), 23668–23677. https://doi.org/10.1002/anie.202008175.

(192) Albertson, D. G., & Thomson, J. N. The Pharynx of Caenorhabditis Elegans.

Philos. Trans. R. Soc. London. B, Biol. Sci. **1976**, *275* (938), 299–325. https://doi.org/10.1098/rstb.1976.0085.

(193) Cohen, J. D.; Sundaram, M. V. C. Elegans Apical Extracellular Matrices Shape Epithelia. *J. Dev. Biol.* **2020**, *8* (4), 23. https://doi.org/10.3390/jdb8040023.

(194) Iwasaki, K.; Liu, D. W. C.; Thomas, J. H. Genes That Control a Temperature-Compensated Ultradian Clock in Caenorhabditis Elegans. *Genetics* **1995**, *92*, 10317–10321.

(195) Kiyama, Y.; Miyahara, K.; Ohshima, Y. Active Uptake of Artificial Particles in the Nematode Caenorhabditis Elegans. *J. Exp. Biol.* **2012**, *215* (7), 1178–1183. https://doi.org/10.1242/JEB.067199.

(196) Faber, P. W.; Voisine, C.; King, D. C.; Bates, E. A.; Hart, A. C. Glutamine/Proline-Rich PQE-1 Proteins Protect Caenorhabditis Elegans Neurons from Huntingtin Polyglutamine Neurotoxicity. *Proc. Natl. Acad. Sci.* **2002**, *99* (26), 17131–17136. https://doi.org/10.1073/pnas.262544899.

(197) Tan, M.; Mahajan-Miklos, S.; Ausubel, F. M. Killing of Caenorhabditis Elegans by Pseudomonas Aeruginosa Used to Model Mammalian Bacterial Pathogenesis. *Proc. Natl. Acad. Sci.* **1999**, *96* (2), 715–720. https://doi.org/10.1073/pnas.96.2.715.

(198) Desai, S. K.; Padmanabhan, A.; Harshe, S.; Zaidel-Bar, R.; Kenney, L. J. Salmonella Biofilms Program Innate Immunity for Persistence in Caenorhabditis Elegans. *Proc. Natl. Acad. Sci.* **2019**, *116* (25), 12462–12467. https://doi.org/10.1073/pnas.1822018116.

תקציר

תולעי נמטודה מסוג סי-אלגנס (*C. elegans*) Caenorhabditis elegans, הן אורגניזם מודל רב שימושי למחקרים ביולוגיים וביו-רפואיים מגוונים, המשתמשים בדמיון הגנטי שלהם לבני אדם, בגודלן הזעיר, ובשקיפות הגוף שלהן. עם זאת, הדמיית הפלואורסצנציה (זְהִירָה) של תולעי סי-אלגנס יכולה להיות מאתגרת בשל פליטת הפלואורסצנציה העצמית (אוטופלואורסנציה) החזקה שלהן בטווח ארכי הגל הנראה לעין, תופעה שעלולה להסתיר את האות המתקבל למשל בעת דימות של חלבונים פולטי פלואורסצנציה נפוצים או צבענים. ננו-צינוריות פחמן חד-שכבתיות (Single walled carbon nanotubes, SWCNT) פולטות פלואורסצנציה בטווח האינפרה אדום הקרוב (Near infrared, NIR), שבו אין לתולעים רקע פלואורסצנטי עצמי. במחקר זה, אנו מפתחים פלטפורמה להדמיית אינפרה אדום קרוב ביצורים חיים (*in vivo*), במערכת העיכול של תולעי סי-אלגנס, העושה שימוש בננו-צינוריות פחמן חד-שכבתיות שעברו תהליך תאימות פונקציונאלית ביולוגית (Bio-compatible functionalization) על ידי צימוד של מולקולות נפוצות כמו די-אן-איי חד גדילי (ssDNA) או פוספוליפיד-פוליאתילן גליקול (Phospholipid-PEG). ננו-צינוריות הפחמן משמשות כסמני מעקב פלואורסצנטיים בתוך מערכת העיכול של התולעת, המוחדרות לתולעת יחד עם צריכת המזון. ננו-צינוריות הפחמן לא עוברות דעיכה או הבהוב פלואורסצנטי עקב מנגנון הפליטה הפיזיקלי שלהן ולכן מאפשרות מעקב הדמיה לפרקי זמן ארוכים. במחקר זה נעשה שימוש במנגנון כליאה ובקרה תנועתית של התולעים על בסיס התקן מיקרו-פלואידיקה (Microfluidic device) על מנת להבטיח סביבת האכלה נטולת חומרי הרדמה, המאפשרת שליטה מרחבית וזמנית אופטימלית בתהליך ההדמיה. יתר על כן, אנו מדגימים שיפור בקולוקליזציה (colocalization) הספקטרלית, יכולת זיהוי בזמן אמת של תנועת צינוריות הפחמן בתוך גוף התולעת, ומעקב אחר מסלולי העיכול. בשל המאפיינים האופטיים הייחודיים של צינוריות הפחמן החד-שכבתיות וכליאת התולעים במערכת המיקרו-פלואידיקה, הפלטפורמה המוצעת מאפשרת יכולות הדמיה מתקדמות של תולעי הסי-אלגנס הן בטווח ארכי הגל הנראה והן בטווח האינפרה אדום הקרוב, ופותחת אפיקים רבים לקידום המחקר של תולעי סי-אלגנס ואורגניזמים מיקרוסקופיים אחרים

אוניברסיטת תל אביב

הפקולטה להנדסה ע״ש איבי ואלדר פליישמן
בית הספר לתארים מתקדמים ע״ש זנדמן סליינר
בית הספר להנדסת חשמל

אנליזה מרחבית וזמנית של ננו-סנסורים אופטיים, המבוססים על צינוריות פחמן חד שכבתיות פלואורסצנטיות, באמצעות פלטפורמות התקני מיקרו-פלואידיקה

חיבור זה הוגש כעבודת גמר לקראת התואר ״מוסמך אוניברסיטה״ בהנדסת חשמל

על ידי

אדוארד שרגא

העבודה נעשתה במחלקה להנדסה ביו רפואית

בהנחיית פרופ׳ גילי ביסקר

טבת תשפ״ד

אוניברסיטת תל אביב

הפקולטה להנדסה ע״ש איבי ואלדר פליישמן
בית הספר לתארים מתקדמים ע״ש זנדמן סליינר
בית הספר להנדסת חשמל

אנליזה מרחבית וזמנית של ננו-סנסורים אופטיים, המבוססים על צינוריות פחמן חד שכבתיות פלואורסצנטיות, באמצעות פלטפורמות התקני מיקרו-פלואידיקה

חיבור זה הוגש כעבודת גמר לקראת התואר ״מוסמך אוניברסיטה״ בהנדסת חשמל

על ידי

אדוארד שרגא

טבת תשפ״ד